University of Sheffield

Computational mechanics of crack growth in selective laser sintering by means of eXtend finite element method (XFEM)

Yongqiang Hu

A thesis submitted in partial fulfilment of the requirements for the degree of

Master of Philosophy

The University of Sheffield

Faculty of Engineering

Department of mechanical engineering

Submission Date: June 2021

Acknowledgements

Abstract

Additive Manufacturing (AM) as a material additive manufacturing process represents a significant breakthrough in manufacturing philosophy; this differs significantly from traditional material removal manufacturing processes e.g. metal cutting. Selective laser sintering (SLS), which comprises many elements such as mechanical processes, material, powders sintering, laser processing, and heat transfer, is an important branch of AM. Several fundamental problems including the interaction between the degree of particle melt (DPM) and crack behaviour of SLS printed part, eXtend finite element method (XFEM) based on material thermoelastic fracture performance are investigated in depth in this dissertation.

The DPM is defined by the proportions of the existence of both melted and crystallised parts, and un-melted particles within the SLS printed component. As un-melted particles come close to the initial crack, the crack attempts to evade these un-melted particles; as the hole is close to the initial crack, and the crack attempts to stay close to the hole.

There are two approaches, the virtual crack closure technique (VCCT) and the cohesive segment approach, used in each simulation. In some cases, VCCT results are similar to the results of the cohesive segment approach, however, the crack path of VCCT results is usually generated more smoothly than the results of the cohesive segment approach; this phenomenon is attributed to the fact that the method of VCCT for opening the crack is based on a combination of the critical energy release rates of normal and shear separation.

Further, the XFEM can be used to analyse the thermoelastic fracture problem. The displacement field of XFEM discretisation is similar to the temperature field discretisation. The test indicates that XFEM allows steady-state 2D thermoelastic problems to be dealt with precisely on a mesh independent of the location and length of the crack.

Contents

List of Figures

Chapter 1

Motivation for selective laser sintering with computational technique

1.1 Motivation

In recent years, there has been growing interest in additive manufacturing (AM) worldwide [1]. AM is a process of joining material in order to build a product using Computer Aided Design (CAD) files which are separated into layers. Its unique technologies and processes provide a range of technical, economic, and logistical advantages, and open up new ground for innovation. The basic AM consists of the production of a digital model, the conversion of a CAD model to a STL file, and printing and post processes. A range of materials such as cement, ceramics, metals, polymers, and composite materials are currently widely used in AM [2-4]. AM has the capacity to produce complex parts at a low cost, including designs which cannot be produced by traditional manufacturing methods, rendering low-yield production and customised products economically viable in many cases [5]; this reduces delivery time for order fulfilment, as well as enabling manufacturing from the source.

AM research was initially developed by Charles Hull in 1986 [6], which was followed by subsequent developments such as stereolithography (SLA), inkjet printing, fused deposition modelling (FDM), selective laser melting (SLM), and selective laser sintering (SLS). Currently, many additive manufacturing processes differ in terms of raw materials, operating principles, and the number of layers deposited to create a part which can be adopted. Many methods are used to soften or melt materials to create the layers, while others cure liquid materials. Each method has its advantages and disadvantages, and many companies provide choices between filament and powder material to build an object. The laser is one of the most frequently-adopted energy sources in AM, because high strength laser beams irradiated onto printed materials can be effectively absorbed without any transmission

medium [7, 8]. Today, selective laser sintering (SLS) has gained attention from a broad range of industrial sectors, such as biomedical, automotive, and aerospace due to its diverse advantages. SLS has become a promising business proposition for manufacturers engaged in different aspects of manufacturing, enabling the faster delivery of new custom products and the gaining of larger consumer markets for companies' products. SLS is an AM technology which promises to revolutionise traditional manufacturing processes, decrease the length of design and production cycles, and enable the manufacture of parts without the need for tools for some individual items, saving significant costs and time [9]. However, there remain many key issues which need to be addressed before the widespread industrial application of the SLS process. SLS is therefore the chosen research topic of this thesis.

SLS employs a transient cooling pattern to control phase compositions and phase percentages, grain sizes, and shapes to enhance desirable mechanical properties. Other experimental studies of effects on SLS processes have been developed, as referenced in the literature review [10, 11]. Berzins et al. [7] suggest that in SLS maps, the position of the boundaries and sintering are strongly influenced by powder particle size and build parameters. Because of the often inhomogeneous nature of the build parameters used, the SLS manufactured parts' material properties vary significantly [12-14]. Further, the presence of un-melted particles due to incomplete melting introduces instabilities. This indicates that printed engineering parts usually develop unexpected fracture problems; the presence of fracture problems and other flaws can be influenced by thermal/mechanical load. Because SLS printing parts are generally applied under huge temperature conditions, this may increase the chance of failure due to instability [15, 16]. The main source of failure is attributed to geometric discontinuity or stress concentration. This form of discontinuity usually takes the form of a sharp change of geometry, opening, hole, notch, and/or crack [17]. As a result, a more comprehensive understanding of the printed parts' performance is required, not related to mechanical testing, but to fatigue and fracture behaviour. The work report on the majority of the literature [18-20] is based on experimental study examining the potential of SLS to produce parts using polymer powders. This can be done experimentally, but on a microscopic scale because individual particles play an essential role, and a simulation method can give an essential advantage.

Computational mechanics (CM) is an important method in research into, and the characterisation of, SLS problems. Some examples where CM has been put to practical use are semiconductor modelling, glass manufacturing, petroleum reservoir modelling, and biomechanics and vehicle crash simulation [21, 22]. The successful simulation of complex physical events due to the application of a variety of principles, methods and concepts means that CM is interdisciplinary [23-26]. For example, when the behaviour of the material is linearly elastic, the structure for predicting the distribution of loads, stress and thermal analysis becomes a vital tool. However, the available computational tools are not as robust as linear stress analysis in the simulation of material faults. The fields most relevant to computational mechanics in mathematics are numerical analysis, linear algebra, and partial differential equations. Modelling and analysis of these discontinuities is meaningful, as it builds on the understanding of their behaviour within selective laser sintered (SLS) parts and contributes to their longevity and performance. Prediction of the macrostructure performance of SLS parts requires better microstructural representation [27]. Performance, as well as properties' modelling of SLS material, has been examined, especially in term of strength and damage. The impact of the microstructure is remarkable, and it is impossible to fully display SLS using a simple macroscopic model in order to successfully predict dynamic damage. The theory of SLS and the opportunity it affords to calculate predictive methods are shown below [28-30]:

- Faster computational method:
    - For process control, fast emulators, deduced-order model
    - For high-fidelity physics-based simulation (such as implicit methods), an accurate, efficient and robust numerical method

- Mechanics of the material – the SLS materials' model as well as properties
    (such as solid-solid phase transformation)
    - Linkage of microstructure information to macroscale model
    - Damage as well as plasticity and modelling

- Material processing
    - Residual stress

3

- Linkage of microstructure information to macroscale mode such as cooling rate maps and thermal gradient
- Solidification as well as melting cycle, alloy composition distribution, microstructure morphology evolution, melt pools and liquid-solid phase change models [28-30].

In modern design, SLS applications are so diverse that there is a high demand for powerful digital tools to avoid expensive and time-consuming experimental methods. This demand is more evident in the failure and fractures analysis of SLS parts, which prompted the author to conduct this research study.

The most commonly used numerical methods, in order of dominance, are the boundary element method, the finite difference method, and the finite element method (FEM). FEM is far more prevalent than the finite difference method in solid mechanics, while the finite difference method is equally applicable in electromagnetism, thermodynamics, and fluid mechanics. Various methods address this problem, but the literature illustrates some general limitations, such as the divergence of the numerical technique before virtual failure. Therefore, failure modelling of materials remains an ongoing study object [31, 32].

For a standard simulation rule, the problem often becomes more complicated when the connections between some elements are changed; for example due to a cut, thermal effect or resection. During FEM, these direct discontinuities potentially cause massive remeshing and mesh adaptation [33, 34]. To find appropriate and high-quality mesh, machine and time cost is uncertain and critical. Although the mesh performed smoothly at the early stage for a model, the success of subsequent remeshing cannot be guaranteed; for this reason, it should be avoided for remeshing and mesh adaptation.

In order to prevent the remeshing, a fresh method, based on the extended finite element method (XFEM), was introduced in 1999 [35]. The use of XFEM for dealing with element resection is discussed in the following sections.

1.2   Aims and objectives

The project is designed to obtain an understanding of the nature of microcracks in printed engineering parts obtained by SLS. The objectives of this project are summarised as follows:

- To review the general understanding of the application of SLS and FEM to fracture problems

- To summarise the empirical literature and fatigue fracture modelling relating to SLS

- To conduct testing to study DPM in the microcrack paths of printed engineering parts obtained by SLS

- To conduct testing to study microcracks in thermoelastic fracture mechanics obtained by SLS

1.3   Organisation of thesis chapters

This thesis comprises six Chapters. In **Chapter One**, the key motivation for the study and the aims of the thesis are outlined.

In **Chapter Two**, the basic process principles of SLS machining and the main factors which affect the quality of SLS printed parts are presented. The state of the art of SLS fracture problems are discussed in view of currently published understandings.

In **Chapter Three**, the first section provides a general understanding of the fracture mechanism, while the second section concerns the application of interface damage approaching linking with virtual crack closure technique (VCCT) and cohesive elements. The third section offers a detailed explanation of XFEM when used in heterogeneous material cracks and SLS.

In **Chapter Four**, three tests indicate that the degree of particle melt (DPM) has a critical effect on the crack behaviour of a SLS printed engineering part under load. The mechanism of how un-melted particles and porosity affect crack behaviour is examined. It

is observed that the location, number and size of un-melted particles and holes lead to significant changes in crack length and path.

Chapter Five begins with discussion of the background of SLS printed parts and XFEM in thermoelastic fracture mechanics, addressing the interaction between a single crack and a single circular inclusion under thermomechanical condition, comparing this with existing solutions.

In **Chapter Six** the conclusions of the thesis are listed along with the future developments proposed in this thesis.

Chapter 2

Selective laser sintering (SLS) process

Selective laser sintering (SLS) process has emerged as one of the fastest growing, most successful, and commercially available AM methods. It not only produces accurate models and prototypes, but also forms parts with reliable structures for direct functional use. It has attracted increasing attention from modern manufacturing industry due to its significant advantages in terms of wide selection of powders, applicability, relatively simple manufacturing process, high moulding accuracy, lack of requirement for support structure, and direct sintering of parts [36]. However, in terms of reliability, mechanical properties, precision, and the cost of manufactured products, SLS has not yet made a significant breakthrough and has not yet reached the necessary maturity level for general industrial applications. Therefore, it is necessary to conduct more in-depth research on its forming mechanism, the selection of new materials, optimisation of process parameters, and the pre- and post-treatment processes of SLS, in order to further improve the performance of SLS products and meet the requirements of industrial production [37, 38]. Research into SLS mechanisms, such as the laser-material interaction process, the evolution of temperature and stress fields during laser sintering, and the related physical and chemical processes, continue to require further exploration in terms of how to improve the final physical features of the manufactured components and improve production efficiency. Currently, this is an important aspect of SLS technology research, which is significant for the development of both SLS process and AM technology [39].

The Chapter firstly provides a basic overview of SLS, including commonly used technology, characteristics of SLS, processing parameters, material types, and sintering theory. The advantages and disadvantages of the use of SLS are then presented, after which the empirical literature in SLS fatigue fracture is outlined. This Chapter thirdly introduces state of the art obeys with reference to academic studies conducted by other researchers. These are the main research foci of this study.

2.1 Overview of the SLS process

SLS was licensed to DTM Corporation, having been initially proposed by the University of Texas at Austin in the mid-1980s [7]. Compared to available processes of AM, there is a use of CAD software or a computed tomography imaging scanning process to present the elements in a three-dimensional manner. Selective laser melting (SLM) can only be employed for certain metals, such as aluminium and steel, but SLS can be used for many metals, as well as polymers and alloy powders. Laser scanning in SLS does not have the capacity to completely melt the powders. Meanwhile, at molecular level, the elevated local temperature on the grains' surface leads to fusion of the powders [40, 41].

Dramatic rise in metal AM system sales   Source: Wohlers Report 2018
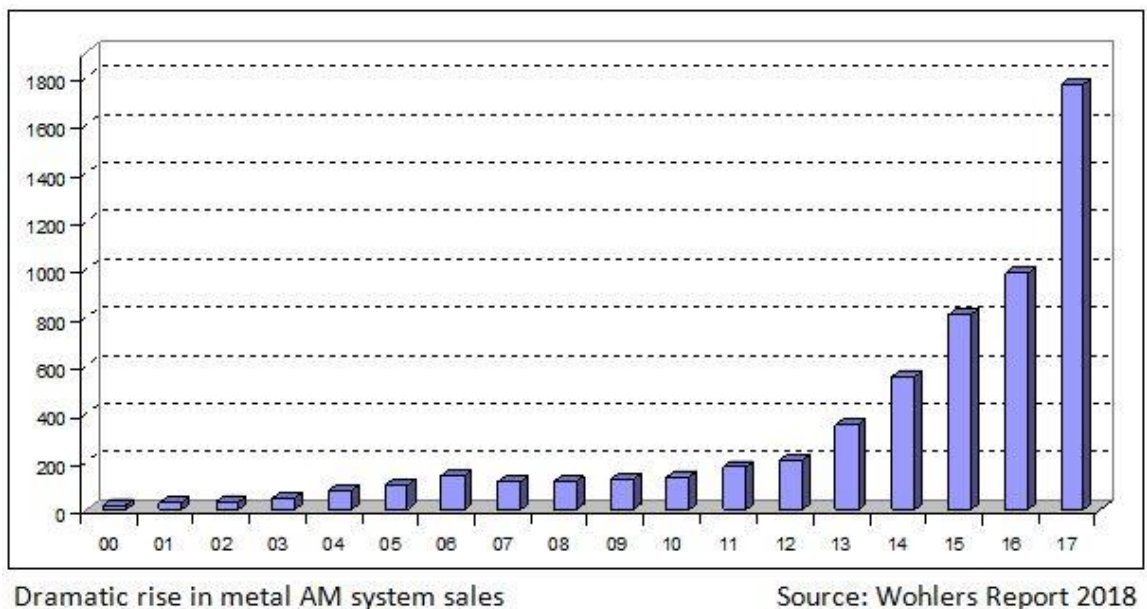
Figure 2.1 AM Services's global income (USD$ millions) and products from 2000 to 2017 [42]

More recently, among commercial users and research institutions, SLS processes have become increasingly popular. **Figure 2.1** presents the increased state of the revenues for AM services as well as products in the years between 2000-2017, which can be attributed to these manufacturing techniques' advantages, such as reducing material waste and building complex geometries, and directly fabricating components with moving parts [42].

In addition, a significant advantage can be gained in terms of reducing the overall production costs of an item.

Selective Laser Sintering

1 Heaters
2 Build Chamber
3 Powder Delivery System
4 Printed part
5 Recoater
6 Laser Beam
7 X-Y Scanning Mirror
8 Laser
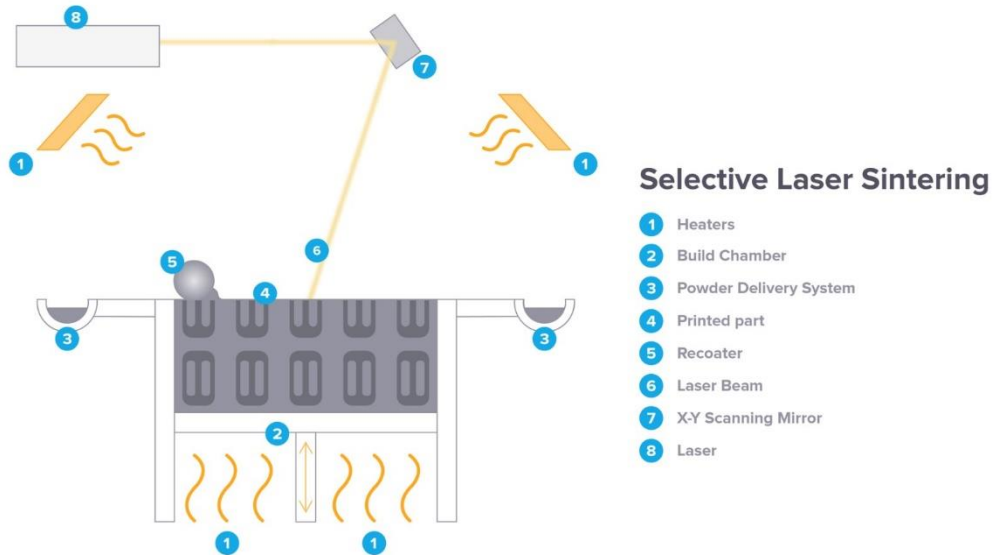
Figure 2.2: Schematic of selective laser sintering (SLS) [43]

SLS has the capacity to deploy a laser beam layer by layer to selectively fuse powder into a designed solid object (see **Figure 2.2** [43]). It adopts a fine powder to fuse the grains, heated by a laser beam with a range of 7W to 200W in terms of plastic [7, 44]. For the purposes of decreasing thermal distortion or increasing fusion in the former tier, it heats the whole bed under the material's melting point before the laser beam sinters the powder. The bed is reduced, with a novel powder layer being used after the construction of each layer. Then, a rotating roller is applied to distribute the powder consistently. The unsintered material powder is retained in its proper position to facilitate the construct, but the sintered one forms the part. After completion of the build, the unsintered material is wiped away and later reused. The procedure is carried out for every tier of the CAD model before it is performed on the last tier [43].

The procedure consists of each selective laser sintering system, which is described as follows. The major differentiators are measurement of the build volume and the type of laser. A variety of systems provides various solutions for layer deposition, powder dispensing and temperature control. SLS requires tight control and a high level of precision. Before removal, in order to minimise heat-induced distortion, stresses, and warping when

it is processed in the course of preheating, sintering, and storage, the temperature of the powder in addition to the (incomplete) components should be limited to below 2 °C [7].

2.1.1 Characteristics of SLS

The unique characteristics of SLS compared to other AM technologies are as follows [45]:

- A variety of materials is available. Theoretically, SLS can be produced using any powder material whose viscosity decreases when heated. A variety of powders including polymer, metal, ceramic powder, and quartz sand powder can be used as sintering material.

- The manufacturing process is simple: given the fact that the unsintered powder facilitates the creation of the cavity and cantilever part of the model, the use of stereographic forming (stereolithography) and fused deposition moulding (FDM) is not required. SLS can directly produce complex shapes and parts.

- High material utilisation rate. The un-sintered powder can be re-used without creating material waste, which reduces the cost of production.

- Forming accuracy depends on the type of material used, particle size, geometry of the product and its complexity. The accuracy of the original shape can reach ±1%.

- It has a variety of applications: as a result of the diversification of the forming materials, various forming materials are available to enable the production of sintered elements for different purposes. Sintered parts for different purposes, such as the production of plastic functional parts for structural verification and functional testing, metal part moulds, precision casting wax mould, and sand mould can be used.

SLS is a layered manufacturing technology with incomplete melting. In general metal manufacturing, SLS materials consist of two types of powder materials, those with high and low melting points. During the laser sintering process, the low melting point of powder particles melts, while the high melting point of powder particles does not melt as the temperature increases. The low melting point of powder particles acts as an adhesive which

mixes the high melting point powder materials to form the final part. The metal parts manufactured by this process contain certain voids and do not yet reach full densities [46].

In general polymer manufacturing, polymer powder can be supplemented by other additives such as carbon or glass fibres to enhance the thermal and mechanical behaviour of the polymer element. Otherwise, due to the large spot diameter of the laser beam, the internal porosity of the final part can be of considerable size [47].

2.1.2   Processing parameters which influence SLS

The SLS production process is relatively complex, and is influenced by many factors. In SLS, the laser beam raster scans the outer layer of the powder during the sintering process i.e. the beam moves in the x-direction at various y-positions, which is clearly shown in **Figure 2.3**. Some scanning factors which impact the method, as well as the intensity of energy delivered to the powder's surface, are the laser spot diameter (D), the laser beam velocity (U), scan spacing (S), the fill laser power (P) and the vector length (L) of the scans. All of these factors work in the way shown in the following sections [48].
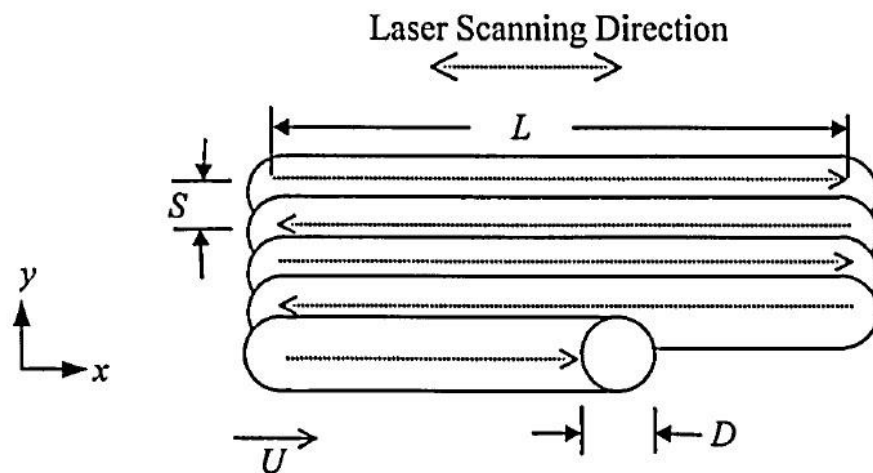
Figure 2.3: Processing parameters and elements which influence the SLS process [48]

2.1.2.1   Laser spot diameter

SLS processes mainly use CO_2 and Yb-fibre lasers, related to the different sort of material. SLS processes mainly rely on CO_2 lasers ranging from tens to hundreds of watts average

11

power because polymers are marked with more absorption in terms of their operating wavelength, which is also useful in the sintering of oxide ceramics and composite. In contrast, the laser sintering of metal powders requires Nd:YAG lasers, or more commonly Yb-fibre lasers. They produce a laser beam of 1064nm in wavelength. This could be approximate to the high absorptive range used by metal powders [49]. The SLS process with a reliance on medal power, known as direct metal laser sintering (DMLS) has the capacity to distinguish from SLS with a basis of polymer. In addition to metal powders, Nd:YAG and Yb-fibre lasers can also be widely applied in the sintering of carbide ceramics. Instead of the operating wavelength, additional laser factors impact the mechanical features and geometry of SLS printed elements. Laser power and scanning speed are the main factors impacting the sintering procedure [39]. Scan spot diameter is the distance from the reflector of the scanner to the outer layer of the powder bed; this affects the scanning speed of the sintering plane. The scan speed is varied by adjustment of the rotation speed of the reflector.

2.1.2.2 Fill laser power

The laser beam's feature of interest is its laser power which forms the energy used in the powder bed (pulsed or continuous). The continuous laser has a fixed diameter which continuously emits light moving in a linear manner at a fixed scan speed across the cross point of the elements. Different lasers are generally marked with a fixed level of energy output, and in the majority of applications the heat is allocated in a similar manner, leading to the homogeneous melt of the powder through a bed of powder.

Hooreweder et al. [50] observe that laser beam scanning and energy absorption are modelled by the use of a SLS machine, relying on the analytical ray-tracing model which performs the calculation of the possible sintering zone factors (width and thickness). This energy required to fuse certain powder elements is based on this equation:

$$E_m = (c_p \times \Delta T + c_l) \times \rho \times V \qquad (2.1)$$

where:

c_p **specific heat** ($K_J/K_g K$)

V **volume of the (spherical) particle (***mm*^{3}**)**

ρ **density (***kg/mm*^{3}**)**

c$_l$ **latent melt energy (***K$_J$/K$_g$***)**

ΔT **increase needed for melting (***K***)**

This process determines a plain contrast of the absorbed energy E_i to E_m if any part has the capacity to absorb sufficient energy to melt. Based on the most horizontal molten elements, it evaluates the sintering zone dimension [27].

2.1.2.3   Melt pool dynamics

Examination of the behaviour of the final parts of the molten material reveals oscillations due to the high-speed laser processing and the high thermal gradients induced to the powders. During processing, the solid phase presented formation is influenced by these oscillations, thus during the material's molten stage, different phenomena exert influence on its size and shape [51].

Two phenomena, wetting and capillarity, are guided by the interface and surface energies present in the molten material. Capillarity means a lack of assistance of external forces and the capacity of a liquid to move in a confined space. Wetting means a solid surface and the capacity of a liquid to make connections. With SLS technology, in order to successfully build components, it is crucial for both liquid and solid features. The liquid wets the underlying material differently, relying on the condition of the solid material as well as the molten conditions [52].

In this case, a spreading coefficient is adopted to explain the wetting behaviour. The spreading of the liquid is favoured, because the coefficient rises positively; this is divided into tiny spherical droplets in a process called 'balling' as the molten material becomes less stable on the solid when the wetting angle rises. During laser processing, temperature gradients go up because of the non-uniform heating, therefore the balling's formation is related to the induced capillary instabilities [51].

2.1.2.4 Discussion

The SLS process can improve the quality of the product fabricated by appropriate selection of the optimum values. **Table 2.1** indicates that material properties, laser power, scan speed, and layer thickness are four main elements which influence the mechanical properties of the SLS process [53]. For example, the laser power controls feed bed temperature which influences the end properties. If the temperature is too high, this causes premature melting; if the temperature is too low, complete sintering results with poor edge definition, in which layers do not adequately fuse with the layers below and are not melted throughout. Therefore, within an SLS printed part, many particles have cores which cannot be melted and may not enter a fully melted state during the sintering process. In order to melt the particles fully, these areas arise in which there is insufficient energy available to be input to the powder. According to the machine parameters, it is necessary to define a universal energy density because the proportion of the powder is determined by the amount of energy input used by the material [54]. However, it is hard to grasp the nature of these parameters' impact on products' features due to the complexity of the process.

Table 2.1: Dependence of output parameters of SLS on the input parameter [54]

	$Target^a$	$Target^b$
Factor	Value	Value
Laser power (W)	3.71	3.82
Scan speed (mm/s)	41.9	48.9
Energy density (J/mm^2)	0.35	0.31
Response	Optimum value	Optimum value
Density (g/cm^3)	0.728	0.656
Flexural modulus (MPa)	337.1	289.7
Stress at 10% (MPa)	49.3	46.2
Desirability	0.69	0.43

[a] The target involves maximum stress, maximum flexural modulus, and maximum density.
[b] The target involves maximum stress and maximum flexural modulus, and minimum density.

2.1.3   Materials used in SLS

The SLS process is unable to be restricted to specific categories of materials; in theory, metals, ceramics, composites, and powder-based thermoplastics can be used in the production of SLS parts. When manufacturing components by SLS, materials of interest are selected according to the required conditions of the previous product. The thermal and physical properties of the material (such as specific heat, thermal conductivity and density) determine the resultant thermal historical behaviour. In general, in a process such as SLS, thermal conductivity is one of the principal thermal physical properties which affect the processing of materials, and the coefficient of thermal expansion is the critical value of the residual stress produced in the process of determining the solidification of molten materials. The above properties depend on the materials used, and the chemical composition of the material generally determines the behaviour of the materials. The main material types used in the process include the following: [16, 55-57]:

- Wax: The traditional waxes used for investment casting (alkane wax, fatty acid wax, and others), were characterised by low wax mould strength, rendering it difficult to meet the requirements of fine and complex structure castings, and the moulding accuracy was poor, therefore DTM represents a low melting polymer wax composite material [55].

- Nylon: Nylon materials can be transformed into functional parts by use of the SLS method. Currently, nylon materials with four components are widely used commercially:

    (1) Standard nylon, which can be used to make models with good heat resistance and corrosion resistance.

    (2) DuraForm GF, not only has the same performance as DTM nylon, but also improves the dimensional accuracy of parts and reduces surface roughness.

    (3) Fine nylon medical grade, which can be steam sterilised by high temperature autoclave for five cycles.

(4) ProtoFormTM composite is a glass-strengthened DuraForm GF. This kind of modified material, compared to unreinforced DTM nylon, has better processing performance, whilst improving heat resistance and corrosion resistance [56].

- Metals: The use of metal powder for rapid prototyping is the trend of laser rapid prototyping from prototype manufacturing to rapid direct manufacturing. It greatly accelerates the development of new products and has broad application potential. In the selective sintering method of metal powder, three types of metal powders are commonly used:

  (1) a mixture of metal powder and organic binder

  (2) a mixture of two metal powders, one of which has a lower melting point and is sticky, which is the role of the binder

  (3) A single metal powder sinters the unit system, especially the high melting point metal, which needs to reach the melting temperature in a relatively short time, and requires a high-power laser. The problem is the low density and poor mechanical properties of the parts due to their porous structure [16].

- Polycarbonate: The research on polycarbonate sintering moulding is relatively mature. Its moulded parts have high strength, good surface quality, and easy demoulding. They are principally used to manufacture lost foams for metal parts in the aviation, medical, and automotive industries in investment casting, and in various industries as general-purpose plastic mould; examples include DTM polycarbonate of the DTM Company. However, polycarbonate is more expensive than polystyrene. Some researchers have focused on polycarbonate (PC) and discussed its sintering process in order to improve the precision of moulded parts [55].

Due to the use of powder materials in the SLS process, the absorption value of bulk materials is different to that of powder materials. A complex process is required to obtain direct measurement of the absorption of powdery materials; it is proven by a numerical models that the absorption of the metal powder layer used in SLS is significantly greater than its value on the plane. This phenomenon is due to the multiple scattering present in

the powder bed, such as the interaction of beams with a rough surface (particle size of approximately 50m) and short wavelength (1070nm). **Table 2.2** shows the published material properties of these powders [58]. It is necessary to grasp the impact and the available range, which can have an effect on end part properties.

Table 2.2: Manufacturer published properties for SLS powders from Stratasys [58]

	Nylon 11	Nylon 12	Polycarbonate	Nickel alloy	TiAl
Tensile strength (MPa)	36	45	35	767	1007
Tensile modulus (MPa)	1392	1700	1950	205000	129000
Tensile elongation (%)	32	20	4	34	16
Part melting point (◦C)	163	184	147	1300	1640
Powder average size (um)	25-92	25-92	25-92	30-60	30-60

The particle size and distribution of the material affect the sintering properties, mainly the surface finish, accuracy and sintering rate of the sintered part. The size of the material particles affects the flatness of the laying powder and the minimum laying thickness, thus limiting the layer thickness of the sintered process. If the material particles are too large, the minimum layer thickness is limited; if the material particles are too small, the powder's adhesion is affected by its electrostatic effect. Also, particle size affects the sintering rate between adjacent particles. Particle size affects the surface roughness and feature accuracy of the part, the sintering rate during the SLS process and the density of the powder bed base. As the particle size of the material decreases, the thickness of the powder layer decreases, which allows a thinner layer to be laid down during the SLS process to improve the principal error of the part. The use of thinner powder layers further improves the sintering between the layers and therefore the density of the part. The powder size also affects the lay-up process, with larger particle sizes producing rougher surfaces. However, if the particle size is too small and becomes fluffy due to electrostatic effects, the powder lay-up process becomes more difficult. Meanwhile, friction, adhesion and other surface forces become relatively high, resulting in a relatively loose laying of the powder at the

bottom of the bed. This problem becomes even more acute once the particles become sub-micron or nano-sized. The nanosized powder is 10% lower than the normal laydown density; such a low density makes it almost impossible to sinter such nanosized powders together under the SLS process [59].

The distribution of granularity generally affects the laydown density, with a maximum level of 74% for particles of the same size. Different sized powders can increase the compactness, as smaller particles can fill the voids [60].

In addition, powder packing density is extremely tight in order to achieve a high SLS processing density. Therefore, in common with other powder processing processes, a wider distribution of particle sizes is applied, rather than a single particle size. Particle size dispersed powders have a higher laydown density compared to single particle size powders. Naturally, this theory only holds true for spherical particle shapes. In general, spherical laydown powders are more effective than other shapes because they flow better than other irregular shaped particles. Therefore, when the processed material is spherical and the size distribution is dispersed, smaller particles are more likely to fill in the voids of larger particles, while the powder density of the layer further influences the density of the sintered part. This is due to the fact that a higher bed density leads to better thermal conductivity and therefore improves the sinterability of the bed substrate. At the same time, a high substrate density ensures a low shrinkage rate.

The quality of the powder layer affects the quality of the finished part, and a new layer of powder is generally smoothed out by a counter-rotating roller. The surface of the layer is relatively flat because the excess powder can be flattened out relatively well. The variables of the roll laying mechanism, such as the linear speed of the roll, the rotation speed of the roll, the feed ratio, the roughness of the roll, and the layer thickness work together to determine the bed density. While all variables have an effect on the density, the feed ratio and layer thickness exert a stronger effect on the density of the bed base and therefore further influence the density of the part. The feed ratio and layer thickness are controlled by the movement of the feed cylinder and the part processing cylinder. The feed ratio is the ratio of the inward movement of the feed side piston to the outward movement of the part side piston. The value is typically approximately 2 to ensure that sufficient powder is supplied to the part cylinder. The layer thickness is a key variable in determining

the quality of SLS machined parts. Generally, a lower layer thickness has a higher part density; lower layer thicknesses provide better sintering between layers and therefore improve part density [60].

2.1.4　Sintering theory

Sintering is the process by which particles bond and grow. The particle system is marked with an excess surface energy compared to dense materials, and sintering refers to the transition from a high energy state to a low energy state, a thermodynamically irreversible process whose free energy reduction is the driving force for the process to proceed. The higher the excess surface energy the particle system has before sintering, the easier this transition process is, and the greater the sintering activity becomes [61].

The sintering process involves the following six theories: surface diffusion vapour transport, lattice diffusion from surface, lattice diffusion from grain boundary, grain boundary diffusion and plastic deformation, and each of the above sintering theories has its own scope of application. For example, Frenkel's model for sintering [62] is only applicable to substances with low viscous flow activation energy (mainly organic substances). The surface diffusion mechanism is applicable to sintering at lower temperatures or relatively fine powders, while the evaporation and solidification mechanisms are suitable for sintering with high vapour pressure, and sintering by atmospheric activation, or in the sintering of relatively fine powders. In contrast, the evaporation and solidification mechanisms are found to be suitable for sintering at high vapour pressures and for sintering by atmospheric activation. In practice, powder sintering is an extremely complex process; sometimes the various mechanisms may occur alternately or simultaneously in a single sintering process [63].

Generally, metal powder sintering processes can be divided into two principal categories: sintering without external forces and sintering with external forces. Sintering without external forces can be divided into two categories: solid phase sintering (SPS) and liquid phase sintering (LPS). Solid phase sintering is a heat treatment process which occurs below the melting point temperature of the powder material. In solid phase sintering, the driving force for the connection between the powder particles is provided by the diffusion drive. In general, the diffusion rate is relatively low, thus solid phase sintering is a relatively

long process. Liquid phase sintering is generally a process of binary or multi-component powders where the sintering temperature exceeds the melting point of one of the components, thus creating a liquid phase. The liquid phase may persist for an extended period of time during sintering, known as long-life liquid phase sintering, or for a shorter period of time, known as transient liquid-phase sintering [64].

Liquid phase sintering allows for a high degree of dense sintering of powder materials without the application of external forces. Although in some cases liquid phase sintering can cause large distortions in the specimen, this process remains widely used for the preparation of aerospace and aerospace materials such as powder Ti alloys, or high temperature powder alloys, hard alloys, and electrical contact elements. It is generally accepted that the liquid phase sintering of powder materials consists of three main stages: I. rearrangement II. dissolution precipitation and III. solid phase sintering.

The powder particle rearrangement stage means that, at a sufficiently high temperature, the low melting point powder material melts, forming a liquid phase which fills the holes, and with the flow of the liquid phase, the particles slide, rotate and rearrange, with the sintered body rapidly becoming dense. It can be claimed that powder particle rearrangement is the most significant and critical manifestation of the important role of liquid phase sintering. Liquid phase sintering without external pressure allows the powder material to reach a high degree of densification, mainly because the particles can be rearranged in the liquid phase environment.

The second stage of liquid phase sintering is the dissolution-precipitation stage, where the diffusion process is intensified. The angular, micro-convex, and microfine particles of large particles are dissolved in the liquid phase and re-precipitate on the surface of the large particles when the solid phase is supersaturated with concentration during the liquid phase. During this stage, the particle shape changes and so-called 'adaptive shape' changes occur, which contribute to the denseness. Later in this stage, some solid phase particles form sintering necks.

The third stage of liquid-phase sintering is the solid-phase stage, where the sintering neck grows further and grain growth is accompanied by coarsening of the pores. This process takes a longer time.

For the SLS process, the powder materials are generally binary or multi-component powders, i.e. the powder material consists of a mixture of high- and low-melting point particles. Due to the high scanning speed of the laser beam (10-100 mm/s), the interaction time between the laser beam and the material is relatively short (typically in the order of microseconds), i.e. the laser beam melts the low melting point powder material in a relatively short period of time to produce the liquid phase, which immediately cools and solidifies when the laser beam is removed. Therefore, during the SLS process, the liquid phase is instantaneously generated and solidified. At the same time, the liquid phase is present for a relatively short period of time, with no time for dissolution-precipitation and solid phase sintering to occur, thus the liquid phase sintering mechanism of SLS exists only in the first stage of conventional powder sintering, i.e. the rearrangement stage [65, 66].

In summary, the SLS sintering mechanism is a type of instantaneous liquid phase sintering without external forces in powder sintering theory. Meanwhile, due to the characteristics of the process, only the first stage of conventional liquid phase sintering (i.e. the rearrangement stage) occurs during the sintering process and the dissolution-precipitation and solid phase sintering stages of conventional powder sintering are suppressed. When the 'virgin sintered part' (i.e. a raw part which has just been sintered and not yet post-treated) is manufactured, it can be post-treated to further improve the mechanical properties of the part by reheating and retaining it.

2.1.5   Technology challenges

Some drawbacks of AM need to be resolved by technological development and further research despite the advantages of AM, in terms of the ability to print complex structures, customisation, and freedom over design. Arising from two mechanisms, the residual thermal stress, the cooldown phase of molten top layers, and thermal gradient mechanisms (TGM) were found in SLS parts described by Mercelis and Kruth [67]. Combined with the relatively slow heat conduction of the material in TGM, the rapid heating of the top surface creates a steep temperature gradient. It is restricted by the significantly cooler lower layer, which induces elastic compressive strain as the top layer expands. However, the upper layer's yield strength is reduced, allowing it to be plastically compressed at an increased temperature. In order to introduce tensile stress in the build direction, the cooling of the

plastically compressed upper layer leads it to shrink, which induces a bending angle to the laser source [68, 69]. Beyond the solidification trace, this mechanism which occurs in the solid phase is relatively significant.

In a similar manner to TGM, the cooling of the molten top layer (shrinkage) induces stress. Because of thermal contraction, it shrinks when the material solidifies and cools. The cooler underlying material restricts this shrinkage, resulting in compressive stress in the underlying material, and tensile stress in the top layer [69].

If the tensile stress exceeds the solid material's ultimate tensile strength (UTS) at a given temperature and point, both mechanisms may exhibit stress relief through fracturing. Solid phase fracturing is regarded as hot cracking [70].

Further, while a large amount of post-processing is usually required to achieve end-use parts, the disadvantages of the SLS process include a poor final surface finish. Building the temperatures in the build volume as well as thermal variations can lead to curling of parts and significant warping, both of which, in tandem, change the part strength, with incomplete melting introducing un-melted particles. They continue to pose challenging issues for the technology, although the reliability of the build part properties has significantly improved, permitting many more applications. Mechanical properties of the produced part in the SLS process are not only affected by the process parameters, but by the base material itself. Analysis of the various parameters and the breakdown of the SLS process is significant and influences the part's end properties. Some of the parameters influence the end mechanical properties more than others, and parameters are also mutually influential. The result is a complex interlinking network of various factors; however, this falls outside of the scope of this research study. Thus, three of the most critical parameters are highlighted in this case: anisotropy, degree of particle, and temperature [69, 71].

The use of the SLS process ranges from metals to ceramics, and once it is available as a powder, it is possible to process almost any material. Nylon-12 is the most widely-used material which is composed of SLS, however, in general, polymers involving other semi-crystalline as well as amorphous polymers are also widely dealt with. For end-use applications, sintered Nylon-12's good mechanical properties provide an example. However, where the currently unreliable production of end-use parts limits the use of AM in the industry, the reproducibility of the mechanical properties poses a challenging issue.

During the sintering process, an understanding of the resultant microstructural changes provides a better understanding of the material, especially within the structure, of the presence of un-melted particles for fracture [71].

2.2   Experimental literature in SLS fracture

There are several studies [44, 72, 73] which focus on SLS processed products' fatigue performance. However, there is a lack of information and comprehensive data on the influence of the defects under cyclic loads caused by SLS treatment on mechanical properties which can evaluate the process microstructure-properties relationship while emphasising the initiation of cracks and the growth of cracks. However, some studies [74, 75] highlight a persistent problem; there remains a significant flaw in SLS processing, although much progress has been made and extensive investigations have been carried out on various materials. After the given process-related defects (i.e. pores and residual stress) and matrix conditions (which are often quite fragile after treatment), post-treatment is required to achieve high fatigue performance. This requirement has led to a lengthy process chain, resulting in an increased cost.

2.2.1   Production parameters

Chen et al. [76] applied the Tauchi method to study shrinkage variation and fracture resistance in the X, Y and Z directions during the sintering phase of SLS processing, and presented the problem of shrinkage compensation from different perspectives. The shrinkage and fracture resistance of SLS has been measured by adjustment of the machining direction and the bending of the machining has been analysed. It has been noted that machining direction plays an important role in SLS fracture.

In addition, Pan et al. [77] carried out experimental studies on cemented carbide, polymer and steel powder materials, analysing the effect of processing parameters on sintering properties based on experimental studies. Meanwhile, the influence of processing parameters on sintering performance has been analysed on the basis of experimental studies. These experiments demonstrate that the strength of the sintered parts does not depend significantly on laser power, scanning speed and scanning interval within a certain range.

The study demonstrated no significant relationship between the strength of the sintered part and the individual parameters of laser power, scanning speed and scanning interval. In contrast, it is demonstrated that warpage is caused by the thermal expansion coefficient of the sintered and non-sintered phases. The difference in thermal expansion coefficients of the sintered and non-sintered phases, as well as the temperature difference at different locations of the scan trajectory and the height direction of the powder layer, have been shown to be the results of warpage. Pan et al. [77] also suggests that a number of experimental studies have been carried out with the use of the roll laying method of SLS machining, which provides a basis for sintering high quality machined parts. This provides a basis for sintering high quality parts.

In addition, using numerical analysis, Borzan [78] investigated energy transfer, heat transfer, and sintering, analysing the effects of laser power, laser beam velocity, scan spacing, laser beam diameter, scan line length on the processing temperature field, density and strength of printed parts. As input laser energy increases, the density and strength of SLS printed parts significantly enhances. Further, Borzan highlighted the fact that there is no significant change in fracture performance, and it should be more impacted by the sintering mechanism because the microstructure of the printed part is influenced by the sintering mechanism.

2.2.2   Sintering mechanism

Kruth and other academics [79-81] conducted in-depth studies, publishing a number of articles classifying the sintering mechanism of SLS, selective laser melting (SLM) and direct metal laser sintering (DMLS) processes, which have contributed to the understanding of SLS sintering theory. The classification of the sintering mechanisms of SLS and DMLS processes has played an important role in the understanding of SLS sintering theory. For example, SLS techniques are classified into four main categories according to their different joining mechanisms: solid state sintering, chemically induced binding, liquid phase sintering partial melting, and full melting. In addition, the team carried out experimental studies on the effect of Nano powders on the sintering properties of SLS, such as sintering temperature and density.

By establishing a shrinkage model for the SLS forming process, Dong et al. [82] investigated the shrinkage form and its pattern of formed parts during SLS processing. The results of the study showed that shrinkage is related to the degree of sintering and the amount of warpage is proportionate to the shrinkage rate of sintering. The warpage is proportionate to the square of the cantilever length, the shrinkage rate, and inversely the sum of the two layer thicknesses. The composition of forming shrinkage is also investigated, and a model for the calculation of temperature-induced shrinkage, sintering shrinkage, and crystallisation shrinkage is proposed. The relationship between sintering shrinkage and the sintering process is also investigated on this basis, highlighting the fact that it increases with increasing sintering power, increases with decreasing scan interval, and is also related to the length of the sintering scan line, but not the forming direction. In preheating, the effect of radiation preheating density on powder preheating has been studied, and a heat flow density field model is proposed and compared with the experimentally measured preheating temperature field, which shows that the model is of great importance for the design of budget devices and the control of the forming process.

Wudy et al. [83] conclude that the mechanical properties of SLS sintered parts based on polymer powder are poor, and conducted a resin reinforcement study on sintered prototype parts. The effect of curing temperature on the dimensional accuracy of the sintered parts during epoxy resin curing was investigated, and the changes in the mechanical properties and SEM photo microstructure of the machined parts were analysed at different curing temperatures. The relationship between the morphological structure of the fracture surface of the material and the tensile properties and impact was investigated, and the post-treatment conditions were optimised. The changes in hardness, compression, tensile and impact of HB1, HB3A, and HB3B materials after post-treatment were investigated in relation to the untreated materials and the changes of microstructure was observed by SEM. The test results show that the fracture performance of the sintered parts with enhanced post-treatment improved considerably.

2.3   SLS process reflections

This Chapter reviews the relevant academic work which has been conducted in the field of SLS.

This chapter firstly analyses the basic process principles of SLS machining, examining SLS machining process in detail, especially some of the main factors which affect the quality of SLS machined parts. An understanding of the conditions affecting SLS processes is also referenced in the literature. However, potential gaps in knowledge are identified when seeking to understand the evolution of microstructures within components manufactured through SLS. The focus of this study is to bridge this knowledge gap through the development of a tool which supports the understanding of this phenomenon in more detail.

In the SLS process, the laser scan spacing should be smaller than the laser spot radius in order to ensure uniform scanning laser energy distribution. As the thermal conductivity of polymer powders is very small, the temperature gradient between the laser zone and its adjacent area is large; the sintered part is prone to warpage and deformation. Therefore, it is necessary to preheat the polymer powder sintered material and increase the temperature of the powder bed as much as possible. SLS of polymers is a very complex and unstable thermal conductivity process. The use of heat transfer models has the potential to simulate changes in the temperature field during laser sintering, and to support the rational selection of process parameters. Both crystalline and non-crystalline polymers can be used as SLS forming materials, but there are significant differences between the two in terms of sintering behaviour and sintered part properties. Laser sintering of non-crystalline polymers occurs above the glass transition temperature (T_g), with low volume shrinkage during the sintering and high forming accuracy; however, due to the polymer's high apparent viscosity, sintering speed is slow and does not result in dense sintered parts, which produces poor mechanical properties. In contrast, crystalline polymers produce a melt-curing mechanism during laser sintering, which can be directly sintered into dense parts.

The essence of the SLS mechanism is the study of a series of physical and chemical phenomena which occur while the powder material is processed by laser beam; meanwhile

the optimisation of the process parameters is effected by the control of various processing parameters in order to ultimately ensure that the sintered part meets the required forming quality. Due to the complexity of the sintering process and the limitations of the analytical tools, the SLS mechanism has not been sufficiently studied and remains only partially understood. The study of laser-material interaction has provided useful theoretical support for the SLS sintering mechanism. However, the majority of current studies are at micro scale; advances in observation methods and theories render it easier to explain the homogeneity of the sintering tissue, the generation of pores and cracks, and the sintering deformation both at microstructure level, and also at the kinetic and even electronic levels; this is likely to play an important role in the improvement and application of SLS technology.

Based on the findings in this section, further research into fracture mechanics and FEM applied to SLS fracture are discussed in the following section.

Chapter 3

FEM applied to SLS fracture problems

Today, the analysis of crack growth and fatigue life is an important issue in mechanical- and aeronautical engineering. In these engineering sectors, the structure is subjected to repeated cyclic loading within the range where the stress is far below the yield strength; when stress concentration at the crack tip exceeds the critical value, rapid instability growth occurs, resulting in brittle failure of the structure. Inevitably, in all engineering materials, there are initial defects such as fine-scale cracks, inclusions and fine-scale holes. At the beginning of cyclic loading, the growth rate of cracks is extremely slow, but after a period of accumulation, the cracks grow rapidly and in the vicinity of the crack tip, there is a sprouting and accumulation of microscopic initial defects, which interact with the main crack. Eventually, brittle damage occurs without warning, which can cause major engineering accidents [84].

Fracture mechanics often work with strong discontinuities and clearly define cracks which maintain continuity in the displacement field of plastic and fracture mechanics. In some ways, the theory of continuous- and discrete methods can be combined and revised, and fracture mechanics can be used to resolve the weak discontinuity problem [85]. In this particular project, a damage-based cohesive law is used for fatigue fracture analysis, i.e. the extended finite element method (XFEM), which is a discontinuous method [86, 87].

XFEM is a numerical analysis method for fatigue crack expansion based on fracture mechanics. Compared to conventional finite processes, XFEM has unparalleled advantages in modelling crack extension and is widely used in discontinuous media problems such as metallic cracks, non-metallic inclusions, holes, and concrete cohesive cracks. For the existence of fracture in SLS printed parts, it is important to establish the XFEM model for material nonlinear analysis as a guide.

In this chapter, firstly, the fundamental aspects of fracture- and damage mechanics are briefly discussed, followed by a general understanding of XFEM. A literature review on

research into SLS fracture modelling follows, in which currently-published understandings are discussed, with an emphasis on areas of divergence and opportunity. It is these areas of opportunity which provide the focus for the research presented, and a valid research gap is identified.

3.1   Fracture mechanics

Fracture mechanics are the theoretical basis of the design of damage tolerances for structures, and are divided into linear elastic fracture mechanics and elastic plastic fracture mechanics. Linear elastic fracture mechanics are applicable to the case of small-scale yielding near to the crack tip; elastic plastic fracture mechanics are applicable to the case of large-scale yielding near-tip cracks [88].

3.1.1   Linear elastic fracture mechanics
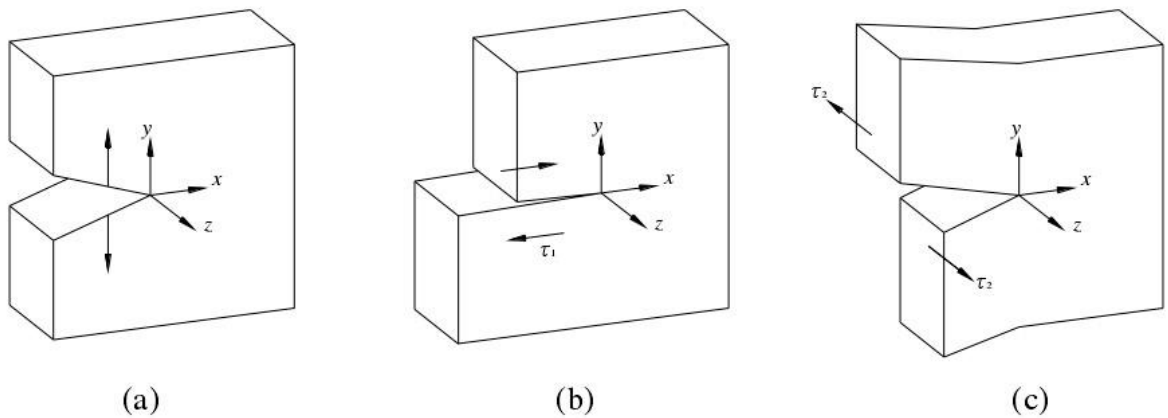
Figure 3.1: Three modes of fracture [89]

On the assumption of linear elasticity of material, the stress field has a $r^{1/2}$ singularity near the crack tip. In 1921, Griffith [89] firstly identified initial defects as the cause of brittle damage in materials below yield strength, and used the change in energy as a criterion for judgement of the continuation of crack extension. Irwin [90] developed Griffith's theory by considering material yielding at the crack tip, introducing the sensitive intensity factor (SIF) and energy release rate in 1957. In 1963, Wells [91] introduced the crack opening

angle (COD) as a parameter of material fracture strength for elastic plastic analysis. In 1972, Rice and Levy [92] introduced the path-independent J-integral, which was widely used to describe the stress and strain fields for the elastic-plastic extension of cracks.

According to the relative displacement of the crack surface, fracture mechanics divide the fracture, enabling a crack to propagate into an opening type (Mode I), a sliding type (Mode II) and a tearing type (Mode III), as shown in **Figure 3.1** [89].

A Mode III crack is often seen as a three-dimensional fracture problem. In practical engineering, the role of shear cannot be ignored, and the actual two-dimensional fracture problems are mainly model I-II crack problems. The study of SLS part cracking should be addressed two questions:

(1) In what direction does the crack expand?

(2) Under what conditions do cracks begin to expand?

The determination of cracks' critical conditions is very important for the study of fracture. In recent years, many researchers [75, 93, 94] have proposed crack fracture criteria by means of theoretical studies and experiments. These theories determine the directional angles, which mostly converge to similar expansion paths. For example, these include the theories of critical plane stress, maximum circumferential stress, maximum energy release rate, and the maximum strain energy density.

The stress intensity factor uniquely characterises the strength of the crack tip stress field and is an important parameter in determining the fracture of a material. The methods used to calculate the stress intensity factor are displacement extrapolation, virtual crack expansion, virtual crack closure technique (VCCT), and interaction integration. A research study by Zerbst et al. [95] demonstrates that the interaction integral method has the highest accuracy. This method uses area points rather than line integrals to calculate interaction integrals, subsequently deriving the stress intensity factor. The crack propagation in actual engineering mainly consists of compound cracks, and its shearing effect cannot be ignored. For compound cracks, the direction angle of crack propagation is considered as a function of compound stress intensity factors K_I and K_{II}. In research into crack growth rates after the proposition of the classic Paris formula, a large number of experimental studies proposed its modification, to take into account various additional factors such as the stress intensity factor threshold, stress ratio, and the interaction of overload and low load.

3.1.2   Elastic plastic fracture mechanics
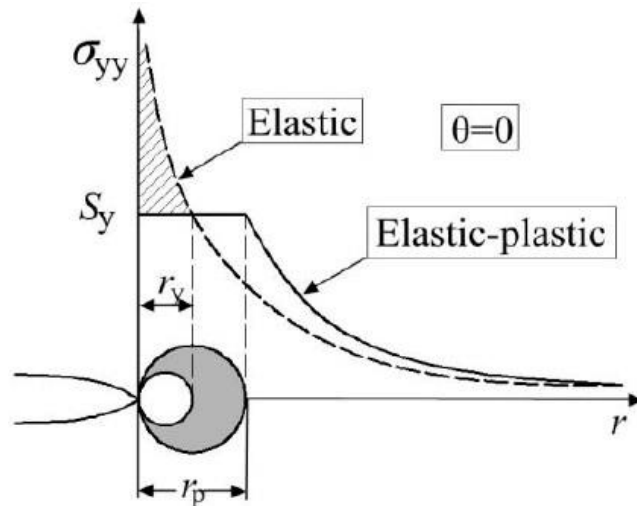
Figure 3.2: Stress distribution and plastic zone around the crack tip [96]

According to the assumption of linear elastic fracture mechanics, the stress at the crack tip is theoretically infinite. Without consideration of the yield of the crack tip material, a conservative numerical solution is obtained. When the size of the plastic zone at the crack tip is small, the results of linear elastic fracture mechanics remain strongly representative, and the majority of brittle materials fall into this category. As the size of the plastic zone is close to the crack size, it is elastic plastic fracture, and low and medium strength steel generally exhibit elastic plastic fracture. On the assumption of material elastic plasticity, a larger plastic zone appears at the crack tip; the stress distribution is shown in **Figure 3.2** [96].

Irwin [33] developed a second-order approximation method for a small plastic zone based on the redistribution of stress at the crack tip. Dugdale and Barenblatt [97] assume that the stress is equal to the yield strength in the plastic zone, replacing the actual crack length with the effective crack length, and proposing a conditional yield zone model and a cohesive force model. Wells [91] proposes a new failure criterion for elastic plastic fracture, i.e. crack opening displacement (CTOD). In brittle materials, the crack opening angle is almost zero, while in elastic plastic materials, due to the large deformation of the crack tip

material and the dullness of the crack tip, the crack opening angle cannot be ignored. Therefore, the first- and second-order CTOD methods are proposed.

Based on the theory of energy conservation, Eshelby [98] defines a series of path independent line integrals, named J-integrals, in the name of energy-momentum tensor. Rice and Rosengren [92] develop the J-integral theory, establishing the relationship between J-integral and energy release rate, and using J-integral as the basis for failure judgement of elastic plastic fracture. Hutchinson, Rice and Rosengren [92, 99] study the singularity of the J integral, establishing the well-known HRR singular field; this laid an important theoretical framework for elastic plastic fracture mechanics.

3.1.3   Fatigue crack growth models
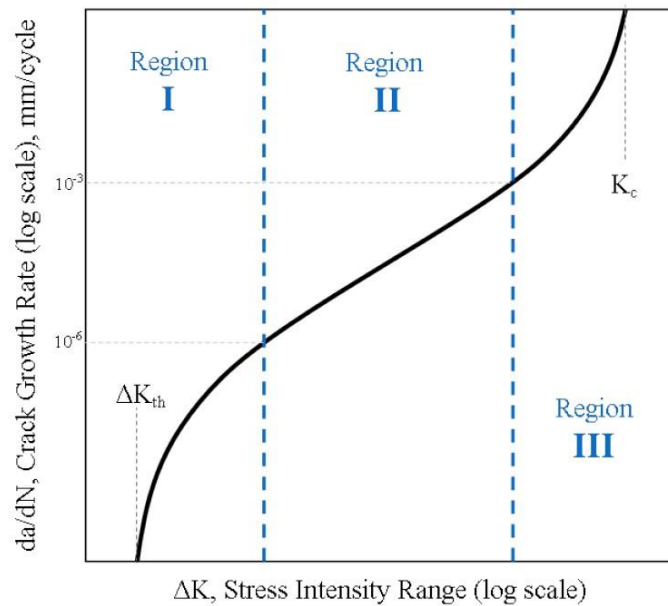
Figure 3.3: Three regions for typical patterns of crack growth rate [100]

This cycle may initiate new cracks or lead to the growth of existing defects in the structure. In order to clearly understand the failure of printed engineering structures under fatigue, it is necessary to take the crack initiation test . The purpose of the crack initiation test is to determine the number of cycles required for crack growth from the existing division. However, in the start-up test, there was no pre-crack in the sample, and the number of cycles required for a new crack was determined. In the crack growth experiment, crack

32

length **a** and the number of cycles **n** are collected in order to determine the crack growth rate. According to the experimental data on crack growth, the relationship between the crack growth rate and load can be identified. Here, the energy release rate is usually calculated by an analytical formula based on linear elastic fracture mechanics (LEFM) [101, 102]. **Figure 3.3** shows three different regions of crack growth rate, which are different to experimental observations. Region I and Region III represent early development of a fatigue crack and the fatigue crack growth at very high rates, respectively. Region II defines a stable crack propagation system, which can be described by Paris' law [100].

The fatigue crack growth (FCG) model is an empirical model according to fracture mechanics, which describes experimental data by fitting parameters of empirical curves in this form [103]:

$$\frac{da}{dN} = f(\Delta K, R)$$

(3.1)

The stress intensity factor (SIF) K was introduced by Irwin in 1957 around the crack tip after his analysis of the stress field, for static fracture analysis [104]:

$$K = F\sigma\sqrt{\pi a}$$

(3.2)

where **a** is the crack length while **F** is the geometry factor which relies on the relative crack length $\alpha = a/b$.

In 1961 Paris et al. proposed the concept of using a simple empirical **Equation 3.3** to apply linear elastic fracture mechanics (LEFM) to fatigue [103]. Paris's law describes fatigue crack growth rate, **da/dN**, as a power law function of applied energy release rate. and is today the most common model used for FCG analysis. It has been developed to reduce the fatigue experimental data and to characterise fatigue crack propagation for a large range of load levels.

$$\frac{da}{dN} = C_P(\Delta K)^{mP}$$

(3.3)

$$\Delta K = F\Delta S\sqrt{\pi a}\underline{\quad}$$

(3.4)

where C_P and mP are constants which rely on the material, frequency of the cycles and the environment, and S is the stress range.

3.1.3.1 Paris model

Paris' law is a simple format, and can more accurately describe the growth of fatigue cracks at the stable stage; it meets the requirements of general engineering structure fatigue design and verification. It is most commonly used in fatigue crack growth rate formulae [105]. Due to the internal dispersibility of the material's structure and mechanical properties, and the errors in external conditions such as specimen size, measurement technology and test environment, the material parameters usually obtained from the test have a certain degree of dispersibility. In engineering applications, the material parameters in Paris' law are often taken as certain values (the average value is the most common), but this processing method cannot provide failure probability or reliability indicators. In order to carry out structural durability and damage tolerance design, and in-service safety evaluation, the method of probability statistics should be used to study the fatigue crack growth rate, and the corresponding probability model should be established for fatigue reliability analysis [106].

3.1.3.2 Walker model

Compared to the Paris model, the Walker model has strong capacity to predict the stable crack propagation stage, with a simple form and fewer parameters [107]. The Walker model is a mathematical formula commonly used in engineering applications to describe crack growth rate. It can be applied to crack growth data with different stress ratios. The model is given by the following relationship:

$$\frac{da}{dN} = C_W(\overline{\triangle K})^{mW} = C_W(\frac{\triangle K}{(1 - R)^{1 - \gamma W}})^{mW}$$

$$\text{(3.5)}$$

$$\triangle K = K_{max}(1 - R)$$

$$\text{(3.6)}$$

Where the constants C_W and m_W are very similar to the constants in the Paris model (see **Equation 3.3**) C_P and m_P. The Walker model's crack growth rate is a modified model of the stress ratio **R**. According to the test data of the fatigue crack growth rate **da/dN** and

the stress intensity factor amplitude ΔK, the fitting curve of the crack growth relationship under different stress ratios can be made. The parameter ΔK is an equivalent zero-to-tension stress intensity which leads to a similar growth rate as the actual K_{max}, R combination. The third curve fitting parameter, γW, is a constant for the material. This parameter may be obtained from data of the various R values, linear regression or trial and error. It is possible that there is no value to be found for γW, then the Walker model cannot is not valid. If $\gamma W = 1$ then ΔK equals ΔK and the stress ratio has no effect on the data [105].

3.1.3.3   Forman model

Taking into account both the stress ratio and the influence of fracture toughness, Forman proposed the following model to study the propagation law of fatigue crack growth in the Region II and III (**Figure 3.3**). Forman's model for the fatigue crack growth rate includes the correction of the stress ratio and the correction of the fracture toughness Forman's model is given by the following relationship [105]:

$$\frac{da}{dN} = \frac{C_F(\Delta K)^{my}}{(1-R)K_c - \Delta K} = \frac{C_F(\Delta K)^{my}}{(1-R)(K_c - K_{max})} \tag{3.7}$$

where K_c is the fracture toughness. If crack growth data for various stress ratios are available, these may be used by computing the quantity in **Equation 3.8** for each data point [108].

$$Q = \frac{da}{dN}[(1-R)K_c - \Delta K] \tag{3.8}$$

Different modifications have been proposed to the Paris model to address issues such as mode-ratio or load ratio on crack growth rate [108]. For the simulation of fatigue crack growth rate under different stress ratios, the accuracy of the fitting is related to the dispersion of the test data. Generally, the Paris model fitting formula does not change along with the change of the stress ratio. It represents the mean value formula of the overall data; the Walker and Forman model formulae themselves change with the stress ratio, and the

change trend is essentially the same: the increase in crack growth rate increases with the stress ratio. In the case of multiple stress ratios, the accuracy of the three models is gradually reduced.

3.1.4 Crack growth direction

The direction of crack extension is considered to be a function of the mixed-mode stress intensity factor present at the crack tip. Although there are several available guidelines for both two and three dimensions, they usually differ only in the initial kink angle, but then converge to a similar crack path. In two dimensions, these methods tend to give the crack extension angle, which is usually the minimisation direction K_{II} [109].

In two-dimensions (2D), the major standards for the crack extension direction are the maximum strain energy density method [110], maximum energy release rate [24], and maximum circumferential stress [111], and the critical plane approach. In the literature, other available standards are the generalised fracture criterion [112] and the standards of energy release rates. With finite elements, the standard which is most amenable to modelling crack growth is maximum circumferential stress, as the growth direction is given in a closed form solution in terms of the mixed-mode stress intensity elements. θ_c is given in a closed form solution in terms of the mixed-mode stress intensity factors. The maximum circumferential stress criterion is given as the angle θ_c given by:

$$\theta_c = -arccos(\frac{2K_{II}^2 + K_I\sqrt{K_I^2 + 8K_{II}^2}}{K_I^2 + 9K_{II}^2})$$

(3.9)

3.1.5 Crack growth magnitude

At every cycle of fixed amplitude fatigue, crack growth can be micro-scale. Two main approaches are suggested in the literature for crack extension in a given simulation iteration of a constant amplitude load. The first approach assumes that known and limited growth will occur in a given iteration, while the second considers that some control laws, such as the fatigue crack growth law, can be used to find corresponding growth increments in a particular iteration. For the situation of variable amplitude loading with unknown

correction factor model for given fracture geometry, the method for constant amplitude loading is no longer effective, and each cycle must be modelled in order to predict the amplitude and path of fracture growth [113].

3.2   Interface damage approaches

Interface damage approach is taken into account in the modelling of SLS printed parts [106]. The use of different modelling methods of delamination has been widely researched in the modelling of composites. The most commonly used methods of calculation are surface-based cohesive behaviour (SBCB) interaction, cohesive elements, and virtual crack closure technique (VCCT). The advantages and disadvantages of these methods in SLS print part modelling, are described in detail below [114, 115].

3.2.1   Virtual crack closure technique (VCCT)

Before the appearance of the virtual crack closure technique (VCCT), many academics had been exploring this issue for some fifty years. The earliest method of using finite element to calculate the crack initiation toughness was to model the specimen with cracks through finite element. During the modelling process, a very fine mesh was created near the crack tip, and then adjusted according to the front edge of the crack tip. The extrapolation of the element extracts the corresponding stress and displacement, and finally calculates the crack's fracture toughness. It is evident that this method is complex to operate, creates a heavy workload, and requires extremely high mesh quality, especially at the crack tip [16]. Subsequently, Irwin [22] proposed the strain energy release rate (SERR), which created a new opportunity for the use of finite element to solve fracture toughness. Researchers developed the virtual crack extension technique (VCET) through the concept of corresponding variable energy release rate. This method uses the finite element to model the specimen with cracks. The first step involves the loading of the model, then the extraction of the stress at the crack tip node; in the second step, the crack propagation distance is assumed and rebuilt. Subsequently the same load is applied, displacement is extracted at the node of the original crack tip, and the fracture toughness of the material according to the strain energy release rate is obtained. The VCET method does not require

37

high grid quality, and the theoretical method is easy to understand, but the calculation process is more complicated. On this basis, Rybicki [33] and Raju [35] modified and mathematically explained the VCET, obtaining the VCCT. Compared to the VCET method, the VCCT method is much simpler. Only one step of finite element analysis is required to obtain the strain energy release rate, and accuracy is also guaranteed. In the VCCT, it is assumed that the opening displacement of the node at the tip of the virtual crack is approximately equal to the opening displacement of the node behind the actual crack tip.
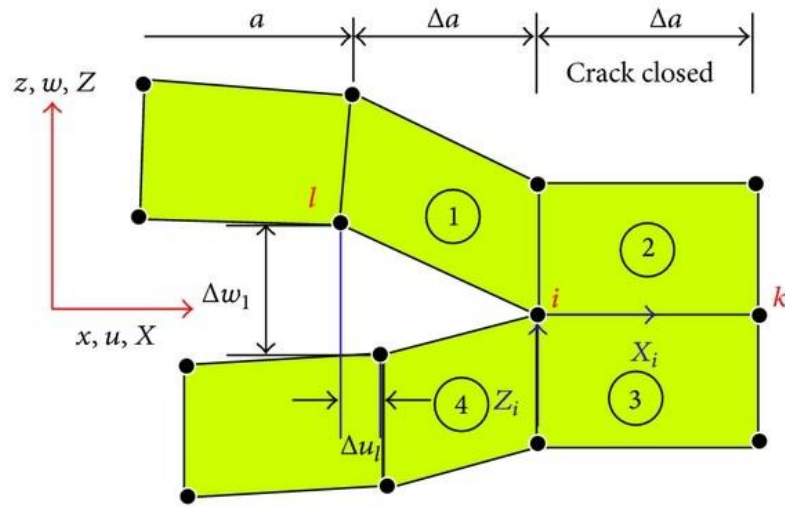
Figure 3.4: VCCT crack propagation scheme [116]

In VCCT, the energy released Δa during the crack propagation is equal to the energy required to close the crack with a size equal to Δa. This technique requires a two-step solution because it uses the force of the first step before crack propagation and the displacement value of the second step. In **Figure 3.4**, the energy required to close the crack between points **i** and **j** is calculated as [116]:

$$\triangle E = \frac{1}{2} \left[X_{1i} \triangle u_{1i} + Y_{1i} \triangle w_{1i} \right]$$

(3.10)

Where X_{1i} and Y_{1i} represent the shear and opening forces at node **i** in step 1.

The shear and normal openings of node **i** in step 2 are Δu_{1i} and Δw_{1i}.

3.2.2   Cohesive element

The cohesion element model is a numerical method used to simulate crack path propagation. The essential theory of this method is based on elastoplastic fracture mechanics. It assumes that ideal linear elastic materials have crack nucleation initiation and crack propagation during the fracture process. The earliest cohesion model is that of Dugdale[93] and Barenblatt [31] whose original proposal was to solve the problem of the singular point of the crack tip in linear elastic fracture mechanics. They divided the crack into two parts: one part is a free surface, the other part has a cohesive force zone, and advanced the hypothesis of the crack tip cohesion zone. This hypothesis considers that, within a critical range, the cohesion of the crack surface is a function of the opening displacement, namely traction-separation law.

This approach is the use of cohesion element to simulate the fracture of SLS printed parts [114]. In the cohesion element zone, the cohesion force increases with opening displacement, but there is a limit value for the cohesion force. When the cohesion force does not reach this value, the material is in the linear elastic deformation stage; when this limit value is reached, the material begins to enter the shape deformation stage. When the cohesive force drops to zero, the material is completely broken and fracture occurs. At this point, the cohesive energy of the material reaches its maximum value. This value is termed the 'critical value of cohesive energy'. It is clear that the important features of the cohesion model are the limit value of cohesion force and the critical value of cohesion energy.

Because the cohesion element model is simple and effective, it can be calculated in finite element methods and the technology is relatively mature. It has been included in commercial finite element software, such as ABAQUS software, and has been applied in many projects.

3.3   eXtend Finite Element Method (XFEM)

Due to the limitations of the above methods, the advantages of the finite element method have gradually evolved. In contrast to the above methods, the finite element method generates a high level of accuracy in solving the stress and displacement fields at the crack tip. Through the connection between the stress, displacement and the stress intensity factor,

the finite element method has become an efficient solution for the stress intensity factor. Accurate numerical solutions are widely used in research into crack propagation problems.

The finite element method has many advantages, such as being suitable for arbitrary geometry and arbitrary boundary conditions, as well as various nonlinear problems. Abaqus is a popular suite of finite element analysis software. It provides linear and nonlinear analyses of mechanical and fluid dynamics, including multi-body systems and multi-physical field coupling [26, 118, 119]. In this case, the crack issue is internal object geometric discontinuity problems caused by the mutation; a problem of this nature is the strong discontinuity problem. To resolve the crack issue, Abaqus provides two commonly-used methods. One is based on the conventional finite element method (CFEM) of research into the crack problem; this method requires the user to establish the model grid which is consistent with the actual situation of cracks. Another approach is based on the extended finite element method (XFEM) for crack problem research; there is no need for the user to establish the model grid which is consistent with the actual situation of cracks. Based on the platform of Abaqus, XFEM inherits all the advantages of CFEM. In addition, there are other various advantages of CFEM. Firstly, the division of the grid has nothing to do with internal structures' geometrical or physical interfaces. Secondly, as the stress and deformation contours cluster, such as the crack tip, the precision of meshing is not required. Thirdly, when crack initiation is stimulated, the grid subdivision does not have to be divided again [59, 120-122]. Therefore, relative to CFEM, XFEM is especially effective in strong discontinuity problems such as crack growth problems.

The extended finite element method (XFEM) is a finite element method in which the interpolation of enrichment functions is added to the standard approximation.

Please note that this article does not use the multi-scale Fe method [103].

$$u^h(x) = u^{std} + u^{enr} = \sum_{j=1}^{n} N_j(x) \cdot u_j + \sum_{B \in \Gamma_{enr}} \cdot \sum_{k=1}^{m} \Psi_k(x) \cdot N^B(x) \cdot a_k^B \tag{3.11}$$

where N_j and N^B are respectively shape functions for normal as well as enriched nodes u^{std} are displacement associated with additional degrees of freedom. e.g. the jump occasioned

by a crack in the displacement field, $\boldsymbol{u}^{enr}$, displacements of standard degrees of freedom, as explained in the following sections. $\boldsymbol{a}^{B}_{k}$ are the added degrees of freedom and $\boldsymbol{\Psi}$ is a special function to effectively computed the discontinuity associated with a crack or the asymptotic field ahead of the crack tip [123].

The advantages of XFEM can be summarised as follows:

- Allowing cracks to be carried inside or through the element, the meshing can be carried out irrespective of the crack shape, and no re-sectioning of the mesh is required to simulate crack extension, saving computational costs.

- Using Heaviside enrichment at the crack face and crack tip to simulate discontinuities, adding additional degrees of freedom to the element nodes near the crack face and crack tip, and capturing the crack tip singularity field by means of a shape function which satisfies the appropriate properties, allowing accurate solutions to be obtained on coarse meshes.

- It is applicable to a wide range of material properties and multi-media problems, and is more applicable to problems such as geometric and contact nonlinearities than the boundary element method.

- Most of the elements remain conventional finite elements, which can be effectively combined with conventional finite elements for large scale finite element parallel computation techniques, and its programmes are easy to write into commercial finite element software [124].

3.3.1   Heaviside enrichment

For the modelling of cracks in uniform materials, two different enrichment schemes are used. For elements cut entirely by cracks, the re-amide concentration function is employed [125]:

$$\Psi(x) = \begin{cases} +1 & \text{if } x \geq 0 \ (above \ crack) \\ -1 & \text{if } x < 0 \ (below \ crack) \end{cases}$$

This form displays discontinuity or 'jump function', which offers a similar stress and strain field on both sides of the crack. Around the cracks, the approach is to work on adding further virtual, independent degrees of freedom to the elements [125].

(a) Smooth crack.   (b) Kink crack.
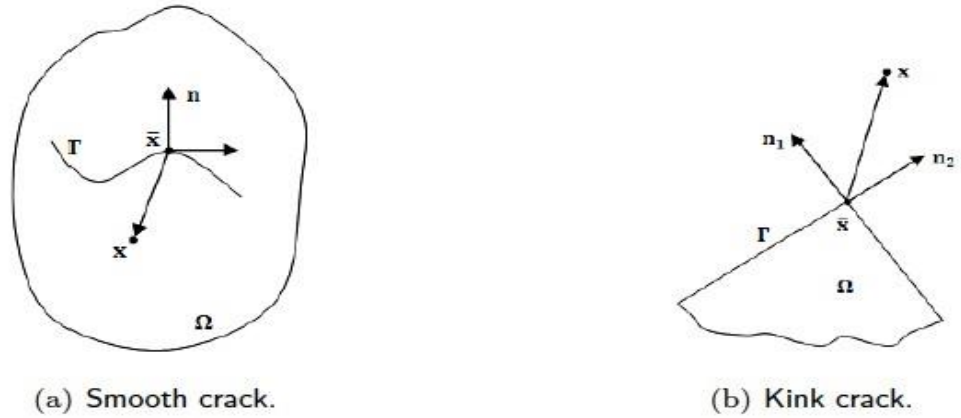
Figure 3.5: Evaluation of the Heaviside function [125]

3.3.2   Tip enrichment

The tip of the belt around the fracture often needs additional concentration to show a special asymptotic field, ultimately requiring additional degrees of freedom. This is achieved through the following functions [103]:

$$\Psi_\alpha(x)_{\alpha=1-4} = \left[\sqrt{r}\sin\tfrac{\theta}{2}, \ \sqrt{r}\cos\tfrac{\theta}{2}, \ \sqrt{r}\sin\theta\cos\tfrac{\theta}{2}, \ \sqrt{r}\sin\theta\cos\tfrac{\theta}{2}\right] \tag{3.13}$$

where in the local crack-tip coordinate system, r and θ are the polar coordinates. By the crack, the Heaviside function in **Equation (3.11)** cut the element, while in the element containing the tip, the crack tip's enrichment functions in **Equation (3.12)** introduces a discontinuity across the crack. Only **Equation (3.12)** is adopted, when a node is enriched by **Equations (3.11)** and **(3.12)** [103].

3.3.3   Inclusion enrichment

Sukumar was the first individual to trial the use of enrichment in XFEM to represent the material interface. This form of concentration is [126]:

$$\Psi(x) = |\sum N_I(x)\zeta_I| \qquad (3.14)$$

where for the material interface level set function, ζ_I are the nodal level set values. However, this solution has led to a mixed problem between the unenriched and enriched elements. In order to improve convergence speed, a minimisation problem is proposed, and convergence is improved; this enrichment has been shown to have optimal convergence. It should also be noted that the enrichment function is zero on all nodes, thus it does not require moving, like a set of other enrichment functions [127].

3.3.4   XFEM crack growth

The technique of calculating the stress intensity factor of mixed function by XFEM is adopted. The literature review conducted by Paris and Belytshko identifies the procedures, advantages and disadvantages of different computing technologies. The most common technique, based on their previous research, is to use interaction integrals in the form of domains extracted from J-integrals. When used with the appropriate mesh, the method has a high accuracy rate under different crack conditions.

In summary, it is the domain form of the interaction integral, where the line integral is converted to an area integral, which is the extension of the J-Integral. The energy release rate is obtained by the J-Integral, and the stress intensity factor of the mixed mode is obtained from the mutual integral [106].

XFEM was initially used for the numerical simulation of elastic crack extension and was later developed to simulate a variety of discontinuity problems. In the context of fracture mechanics, Yazid et al. [94] and Luycker et al. [128] reviewed the application of XFEM in the simulation of various types of cracking. XFEM has been used to simulate elastic cracking, single and multiple cracking, cracking under static and dynamic loading, cracking in homogeneous and non-homogeneous materials, for example functional gradient material cracking, bio-material interface cracking, cracking in isotropic and anisotropic materials, two-dimensional cracking and three-dimensional cracking problems.

In terms of materials, Dolbow [35] applied the XFEM method and interaction integration techniques in order to calculate composite stress intensity factors for cracks in materials with functional gradients. Chen and Zhang [129] applied XFEM to carry out a study of sub-interface crack expansion paths in bio-materials. Zhang et al. [32] used XFEM to simulate the entrapment problem in viscoelastic media.

In the case of dynamic crack growth, Menouillard et al. [130] used XFEM to simulate dynamic crack extension using explicit time integration techniques. Liu et al. [101] combined spectral units and extended finite elements to effectively improve the numerical perturbation problem in dynamic crack extension simulations. Duddu [131] used the XFEM method and level set method to simulate dynamic crack development in rate-independent materials. Prabel et al. [132] used the XFEM method to simulate dynamic crack propagation in elastic plastic media.

In the case of three-dimensional cracking, Sukumar et al. [133] extended XFEM to three dimensions for the first time to study planar type I cracking, and Gasser et al. [23] numerically simulated three-dimensional crack extension in concrete using the extended finite element method. Hosseini et al. [17] used the three-dimensional extended finite element method to simulate the fatigue expansion of semi-elliptical cracks in Al-Li alloy, considering the linear variation of the closure stresses along the crack wave front, and the numerical simulations and experimental data agreed.

3.3.5   Limitations of the use of XFEM within Abaqus

As mentioned, due to its relatively recent introduction, the XFEM implementation in Abaqus remains affected by certain relevant limitations [134]:

- It is still not available in Abaqus/Explicit

- A crack cannot turn more than 90 degrees within an element

- There is no crack branching

- Parallel processing of elements is not allowed

- Only single or non-interacting cracks can be contained in the domain

- Fatigue crack growth phenomenon cannot be modelled

- Only linear continuum elements can be used, with or without reduced integration

- Only general static and implicit dynamic analyses can be performed.

3.4   XFEM in heterogeneous material crack

When analysing actual engineering problems, in many cases, the material is assumed to be isotropic and uniform. However, in fact, the materials used in the project are non-uniform on a certain scale, and there are often many interior defects, such as holes, inclusions, and cracks. These defects seriously affect the overall performance of the structure and reduce its service life. The question of how to accurately model and simulate these defects and analyse their influence on fracture parameters and crack propagation is of great significance to ensure the safety of structures. The finite element method was first used to simulate this nature of problem. By meshing all non-uniform parts, this kind of problem can be simulated more accurately. However, this processing method involves a significant number of computing grids, which consume a large amount of computer memory and CPU space; on the other hand, for the crack growth problem, each sub-step needs to be redrawn, which greatly limits application of the finite element method in the crack propagation of heterogeneous materials.

The combination of XFEM and the level set method enables various types of discontinuities (holes, inclusions, cracks, and material interfaces) to be independent of the calculation grid. For crack propagation problems of heterogeneous materials with a large number of discontinuities, this saves time; the cumbersome operation of modelling various discontinuities and meshing is eliminated, and the problem of mesh redrawing caused by crack propagation is avoided. On the basis of this characteristic, XFEM has been used to conduct extensive research into the crack growth of non-uniform materials containing holes and inclusions [135].

Based on XFEM, Daux [136] simulated the problems of porous holes, multi-branch cracks and cracks caused by holes. Sukumar [133] combined the XFEM and horizontal set method to simulate the problem of holes and inclusions, and Huynh and Belytschko [137] used XFEM to study the fracture problems of two-dimensional and three-dimensional composite material, while Chen and Zhang [129] used XFEM to study interfacial crack propagation in dual materials. Pathak et al. [138] used XFEM to analyse the fatigue life of a flat plate with a large number of randomly distributed discontinuities. Jiang et al. [118] studied the influence of holes, inclusions and cracks on the dynamic stress intensity factor of the main crack based on XFEM. Kumar et al. [139] proposed a homogenised XFEM to evaluate the fatigue life of edge cracks in a discontinuous plate. In recent years, many academics have studied the homogenisation and equivalent performance of heterogeneous materials based on XFEM [140, 141]. In the majority of the abovementioned studies, traditional XFEM was used. For problems with a large number of discontinuities, only a very fine global computing grid can be used, and computing efficiency requires development.

3.5   SLS fracture modelling

On the basis of the research background [10, 68, 141], it is unnecessary for the prediction of macrostructure performance to have a better microstructure representation. Specifically in terms of strength, metallographic characterisation and damage, it has examined the properties as well as the performance modelling of SLS materials. With a simple macro scale model to successfully predict dynamic damage, it is not yet possible to adequately represent the SLS, and the microstructure's effect is highly significant.

The physical simulation of the SLS process refers to the study of the change laws of physical quantities (fields of temperature, stress, and deformation) in the process, with the aim of understanding the material sintering process in depth, and ultimately improving the quality of sintered parts. The sintering process is deconstructed into temperature field, stress field, deformation field and microstructure field. This deconstruction is helpful to enable analysis of the evolution laws of the sintering process, and is very valuable in the calculation of the deformation and stress of sintered parts. The microstructure of a material

depends not only on its chemical composition, but also on the thermal history of its sintering process. The microstructure, especially its influence in the laser sintering heat-affected zone and melting zone, is more noteworthy.

Through the quantitative analysis of these state fields, it is helpful both for researchers to understand the microstructure formation of SLS sintering process, and to analyse the influence of various process parameters on the quality of sintered parts. Currently, due to the incomplete mathematical description of the above-mentioned physical fields, in-depth research into the physical process of SLS is required.

Gusarov, Laoui and Wang [143, 144] provide insights into the evolution of the powder temperature field in SLS, which is essential for the study of the sintering mechanism and optimisation of the sintering process parameters. They first analysed the contact heat transfer between two particles, and subsequently analysed and discussed the effective heat transfer coefficients of face-centred cubic and body-centred cubic powder accumulation models, which laid the foundations for the theoretical analysis of SLS temperature field and stress field.

Kolossov [145] proposed a SLS processing thermodynamic model which considers heat transfer nonlinearity and phase change, and used a three-dimensional finite element method to analyse the temperature change and the deformation of the sintered part during the sintering process. Studies have shown that changes in material properties caused by temperature changes strongly affect the sintering process, and the density of sintered parts can vary between very loose (50% theoretical sintered density) and close to compact.

Dong et al. [146] used the finite element method to simulate the sintering process of the SLS single track in three dimensions. A finite element model considering heat transfer and sintering phenomenon in the sintering process is established. Due to the continuous movement of the laser beam, the model considers the instantaneous phenomenon of laser sintering through the change in the coordinate system, dynamically analyses the heat transfer problem in the sintering process, and introduces the convective heat transfer phenomenon into the model. Although this model can more comprehensively analyse thermal phenomena during processing, it is more complicated than other models. Tests prove that the model can be tested under certain conditions.

Shiomi et al. [147] focuses primarily on the finite element simulation of the metal SLS process. They simulated the evolution of the temperature field and instantaneous stress field during the sintering process of a single-layer metal powder. By analysing the deformation and stress distribution of the sintered sample, they inferred identification of the most likely place to break when the sintered sample was formed. Secondly, colleague academics conducted research on the generation and elimination of residual stress during the sintering process, and found that holding at 600-700°C for one hour can reduce residual stress by approximately 70% [148].

One of the key factors is the microstructure behaviour of an un-melted particle. It has been noted that, with regard to the growth of dynamic cracks under loading within the sintered material of an SLS particle, its behaviour is significantly affected by the presence of un-melted particles [27].

Furthermore, during the rapid melting of metallic powdered feedstock, the SLS process creates large thermal gradients. In solidification, certain alloys suffer from thermally induced microcracking which cannot be damaged by process optimisation. It is difficult to decide on the optimum processing parameters for a given printed engineering part. Therefore, in order to decide on the appropriate parameters required to create an acceptable part, when adopting geometries or new materials, experimentation is usually required. For example, for building tissue using SLS, the design of experiments (DOE) technique was used to study the optimum processing parameters by Partee et al. [149]. Ibbett et al. [27] simulated the onset and propagation of microcracks through the adoption of XFEM. However, very few papers have studied microcracks in printed engineering parts obtained by SLS. With regard to the further development of SLS, there is some research on the critical topics of microcracks in products. Therefore, there are no definite conclusions about the possible effect of SLS on microcracks.

3.6   Summary

In this Chapter, the current state of the art situation in fracture mechanics, interface damage approaches and XFEM has been briefly explained. A literature review about XFEM in heterogeneous material crack and fracture modelling follows, in which currently-published

understandings are discussed, with an emphasis on areas of divergence and opportunity. It is these areas of opportunity which provide the focus for the research presented. Several conclusions can be drawn from this Chapter:

- Discussion of the application of the crack growth simulation algorithm is proposed in this paper in actual engineering terms. By presenting the detailed fatigue crack model and interface damage approach, comparing and analysing the solution and simulating the results of traditional finite element method and XFEM, the effectiveness of XFEM is verified.

- Research into crack growth in heterogeneous materials, and analysis of the effects of various types of discontinuities such as inclusions, holes, and cracks on crack growth at macro and micro levels is presented. Under the framework of XFEM, various discontinuities can be independent of the computational grid, thus the mesh refinement method proposed in this paper can be fully utilised to refine the grids near to the discontinuities. For various types of microscopic defects, multilevel mesh refinement is performed on the local area of the defect, and the problems at different scales are unified into a set of meshes for calculation. Through different numerical examples, the effectiveness of the above method is verified, and the influence of the type, location, size, and other parameters of micro-defects on the growth of macro-cracks is analysed.

- Among the SLS thermophysical process, many academics have constructed 3D temperature field and stress field finite element analysis models. These models need to take into account the convection, radiation boundary conditions, and the nonlinear characteristics of the material's thermophysical properties, and include the process of sintering powder materials into solid blocks, along with the problem of drastic changes in thermophysical properties.

- Un-melted particles are identified as one of the key parameters which may cause a crack in an SLS printed part; further study of un-melted particles will be discussed in the following chapter.

Chapter 4

Study of DPM in microcrack paths of printed engineering parts obtained by SLS

With applicable level set methodology, voiding and inclusion modelling in the eXtended finite element method (XFEM) are to be clarified. To demonstrate the flexibility and application of XFEM, analysis on microcrack paths in selective laser sintering (SLS) printed components is provided in this chapter. This investigation involves modelling of strong (displacement fields) and weak (strains fields) discontinuities. The un-melted particles and holes, causing those discontinuities, are seen to lead to the existence and propagation of microcracks. In this chapter, circular inclusions and holes are modelled for different particle densities and particle distribution patterns in materials to characterise their effect on crack behaviour [27, 150].

In the next step, the proximity of un-melted particles in SLS printed engineering parts made of nylon 12 has been proven to be fundamental and influential in cracking and the eventual failure in previous reports [27, 151-153]. After that, state-of-the-art degree of particle melt (DPM) and XFEM are presented, beginning with a general understanding of SLS printing process and commonly discussed DPM mechanism. Simulations of crack invitation and subsequent evolution were modelled by the integration of constitutive and fracture laws. Then the detailed research for nylon 12 is carried out to understand the material mechanism in SLS fracture problem. Three tests on numerically studying samples are carried out with varied distribution of unmelted particles by XFEM. Model development has gone through multiple stages in this field. Each of these phases attempts to improve functionality and accuracy of previous results. The occurrence and propagation of microcracks were

simulated. Therefore, comprehensive crack behaviours' data and comparative numerical analyses could indicate how the DPM in the SLS component affects and controls crack initiation and expansion. Specific model validations and limitations in the applied techniques are discussed.

4.1   Background

It is widely known that, in SLS printing process, the foundational powder (for instance, nylon 12 is applied in this study) is allocated in a powder bed when a laser beam sinters the pattern of each slice (the cross section of CAD) on the powder bed. As the powder is cured, one layer, with close tie to the prior one, will be printed. The component is printed via the repetition of this process [1, 7]. The mechanism of the SLS has bonding microstructure, it is affected by some parameters leading to inhomogeneity in the final component, such as the input of energy, scan speed, print orientation and part bed temperature.
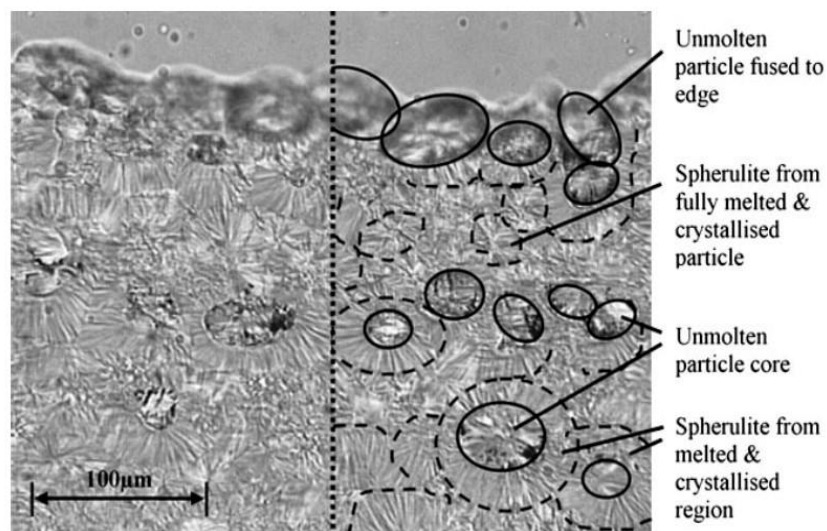
Figure 4.1: The microstructure of a standard SLS part manufactured from Duraform PA (nylon-12-based powder accessible from 3D Systems) [154].

In addition to the reduction in inhomogeneity of SLS printed specimens, some investigators [74, 152-156] indicated that the un-melted core exists in the microstructure of specimens with the help of different methods such as a differential scanning calorimetry (DSC) test and electron microscopy. They found a strong correlation between un-melted cores and

mechanical properties of the final part. **Figure 4.1** [154] indicates micrograph of the cross-section of SLS printed part with full melted and crystallised particles and un-melted cores. The reason to the un-melted core existence is their failure in achieving the fully melted state during SLS process.

The DPM is defined by the proportions of the existence of both melted and crystallised parts, and un-melted particles within the component [156]. The amount of energy density input to the part can adjust the DPM of the final part, therefore characterising an appropriate energy density based on the material behaviours and printing parameters is necessary. Andrew number is applied to measure the energy density in **Equation 4.1** as follows [153]:

$$Andrew\ Number = Energy\ Density = \frac{(Fill\ Laser\ Power)}{(Scan\ Speed \times Scan\ Spacing)} \tag{4.1}$$

As the energy density increases, the DPM grows but the amount of un-melted particles drop off. In this process, material transfer from a 'double phase' structure with both melted and crystallised regions, and un-melted particles to a 'single phase' structure with only melted material. The mechanical properties (i.e. Young's Modulus and tensile strength) of the material rise dramatically when the DPM increases, but after a certain DPM point, the mechanical properties start to drop. One of reasons to this phenomenon is that is once the melting process is completed, this 'single phase' structure material becomes a new material due to the change of molecular structure mechanism. Since the excess input energy can lead to locally vaporise the polymer, gas bubbles will be occurred. The higher number of gas bubbles, the greater the porosity of the final parts. Another reason to this phenomenon is that too much energy will spill-over into regions near the part during the SLS process. It can lead to support part to be caked to the final part, making worse mechanical properties of the part [74]. Among this procedure, DPM plays an important role in the mechanical properties of printed parts. Furthermore, these unfinished melting process brings the inclusion of un-melted particles in the layer, Hitt et al. [151] stated that the presence of these un-melted particles is caused by crack induction and stress concentrations. It is concluded that when setting up the simulation of the model, the DPM is the most important parameter for its effect on the region of un-melted particles and fracture behaviour.

There are several possible polymers (as long as it is a powder) can be processed in the SLS, in different applications. In this chapter, only nylon-12 will be studied, and its advantage is that nylon-12 is the most available manufactured SLS polymers in industry. The excellent material properties of printed nylon-12 make it notable in the market. The crack behaviour of SLS processed nylon-12 products has only been mentioned in a few papers [27, 50, 157-159]. Thus, comprehensive data on effects of defects induced by SLS processing on mechanical properties under cyclic load which allows for an evaluation of procedure–microstructure–property connections with an emphasis on both crack initiation and crack growth are currently not available according to the review of previous literature. However, a fatal problem has been pointed out by several studies, and there is still a major drawback on the process of SLS compared to the convectional progress. It is truly necessary for post-treatment to achieve high fatigue performance, because of the given-related defects, i.e. residual stresses and pore, and material conditions that are brittle after processing. Nylon-12 used in this experiment, is assumed to be under the general post-treatment.

4.2   Numerical implementation

The extended finite element method (XFEM) adopted in this chapter, is a finite element method by which the interpolation of enrichment functions are added to the standard approximation [119]. After that, the solid elements are counted, which have been divided by the enriched function. The crack propagation mechanism implied in this method relies on the initiation criteria such as the evolution criteria, which depends on the material energy release rate. There are two distinct types of damage modelling within an XFEM framework, the virtual crack closure technique (VCCT) and cohesive segment approach [35, 160].

4.2.1   Improved XFEM technique

The research of XFEM method focuses on the use of enrichment functions to better describe discontinuities such as the crack tip displacement field and particle inclusion problems, and the Heaviside function and the low-order terms of the Westergaard crack tip

singular field function are used to simulate isotropy. The linear elastic crack model uses the material interface enrichment function to simulate the weak discontinuity of the material interface. This makes the particle inclusion interface and the crack independent of the grid, and there is no need to remesh when the crack propagates. The displacement approximation of XFEM is:

$$u^h(\boldsymbol{x}) = \sum_{i \in G} N_i(\boldsymbol{x})\boldsymbol{u}_i + \sum_{j \in G_0} N_j(\boldsymbol{x})H(\boldsymbol{x})\boldsymbol{a}_j + \sum_{k \in G_1} N_k(\boldsymbol{x}) \sum_{l=1}^{4} \varphi_l(\boldsymbol{x})\boldsymbol{b}_k^l + \sum_{m \in G_2} N_m(\boldsymbol{x})\chi(\boldsymbol{x})\boldsymbol{c}_m$$

(4.2)

Where N_i, N_j, N_k and N_m are finite element node shape functions, G represents the collection of regular element nodes (all nodes), G_0 means a collection of element nodes for crack penetration, G_1 is a collection of crack tip element nodes and G_2 is a collection of interface element nodes of particle inclusions. $H(x)$ represents the enrichment function of crack surface nodes, $\varphi_l(x)$ is the enrichment function of crack tip nodes and $N_m(\mathbf{x})\chi_m(\mathbf{x})$ is the interface shape function of particle inclusions.

The node displacement of the enrichment unit is not the real node displacement. In order to make all the nodes are real node displacements, **Equation 4.2** needs to be transformed into the following equation:

$$u^h(\boldsymbol{x}) = \sum_{i \in G} N_i(\boldsymbol{x})\boldsymbol{u}_i + \sum_{j \in \mathcal{G}_0} N_j(\boldsymbol{x})\left(H(\boldsymbol{x}) - H(\boldsymbol{x}_j)\right)\boldsymbol{a}_j$$
$$+ \sum_{k \in G_1} N_k(\boldsymbol{x}) \sum_{l=1}^{4} \left(\varphi_l(\boldsymbol{x}) - \varphi_i(\boldsymbol{x}_k)\right)\boldsymbol{b}_k' + \sum_{m \in G_2} N_m(\boldsymbol{x})\chi(\boldsymbol{x})\boldsymbol{c}_m$$

(4.3)

4.2.2 Crack propagation and the level set method

XFEM has been developed on the basis of level set method. This approach has been proven to be difficulty in solving fracture problem because it failed maintain the previous crack surface in a frozen state when crack propagates, letting aside the evaluation of signed distance function in this procedure. Adjustments and adaptations have been required since

the implementation of level set method in curve interfaces, such as crack. Apart from that very set of level marked as φ, the second set level, ψ, is also required in the measurement of crack tips.

Basically, the zero-level set of function $\psi(x,t)$ is to denote 1D crack growth. The intersection of the zero-level set of function $\psi(x,t)$ and its counterpart, $\varphi^k(x,t)$ is at the end of the crack where k is the number of tips. Based on previous statements assumes that ψ is orthogonal to φ and the notes are to denote level set function values [92].

$$\varphi_i \psi_i = 0 \tag{4.4}$$

According to the similar finite element shape function, the functions are interpolated in the mesh and they are now be written as in **Equation 4.5** and **Equation 4.6**.

$$\varphi^k(x,t) = \sum_{j=1}^{n} N_j(x)(\varphi^k(x,t)_j) \tag{4.5}$$
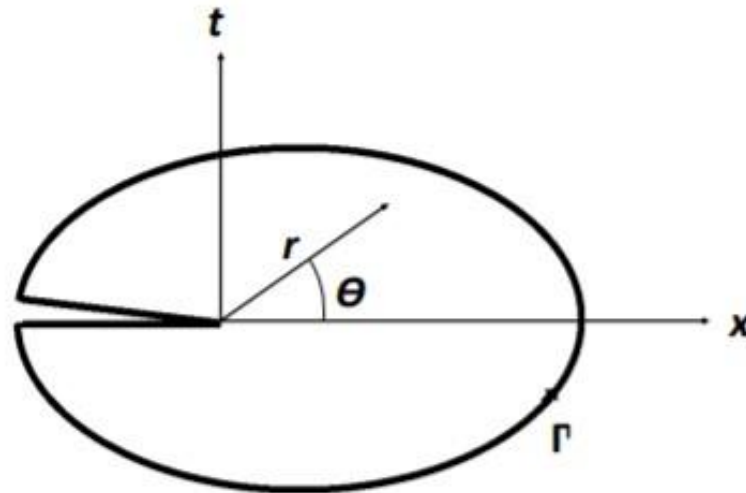
Figure 4.2: Crack tip deformation field coordinates and paradigmatic contour Γ [92].

$$\psi(x,t) = XN_j(x)\psi_j(x,t) \tag{4.6}$$

However, the zero level set of ψ cuts through the entire domain even when the crack is actually embedded in it. An assumption of the part is generated and it is unlikely to change neither its shape nor its moving paths once the crack has emerged. The consistent updates of φ^k and ψ functions lead to the recalculation of the φ function, which are used to model the crack growth. The crack growth direction of Θ, is one of the factor in φ^k and ψ evolution. The velocity vector $v = (v_x, v_y)$, which is normal to the interfaces, is determined by the continuous displacement of the crack tips.

$$\varphi^k_{n+1} = \varphi^{k,r} - \Delta t \, \|v\| \tag{4.7}$$

Abaqus/Standard commercial software failed to estimate the exact time of the test to be performed as it is a Newton-Raphson solver. For this reason, the iterations are computed without time step. The calculation of increment iteration by this stimulation equals the velocity multi-ply by the time difference (Δt). In this equation, the velocity parameter is to measure the displacement (i.e. crack propagation) on the surface of printed material.

$$r = \sqrt{\varphi(x,t)^2 \psi(x,t)^2} \tag{4.8}$$

$$\Theta = \tan^{-1}\left[\frac{\psi(x,t)}{\varphi(x,t)}\right] \tag{4.9}$$

This analysis tales references from local coordinate, among which XFEM is to measure the crack propagation at edges.

4.2.3   VCCT and cohesive segment approach

There are some methods modelling crack propagation in Abaqus, such as cohesive segment approach and virtual crack closure technique (VCCT). The cohesive method requires two elements: a damage initiation criterion and a damage evolution law. The damage initiation criterion reminds Abaqus of the beginning of damage When the level of stress or strain reaches a particular level of "strength" specified in the measurement. Then, there are six available options: Maximum principal stress, train, maximum nominal stress, strain, a quadratic superposition of the nominal stress and strain [161].

The crack propagation direction for the max principal stress or strain criterion is always perpendicular to the max principal stress or strain. Otherwise it is need to specify the crack propagation direction. The damage evolution is based on the effective separation after damage initiates. The simplest way to define damage evolution is to specify the effective separation at failure (i.e. when Damage = 1). The cohesive method can be used with or without the presence of an initial crack.

The VCCT does require the presence of an initial crack, and it is determined by the energy release rate $\mathbf{G}$ (i.e. the amount of energy released from the structure when the crack propagates, forming a new surface). Mathematically, $\mathbf{G}$ represents the energy released per unit area [161].

VCCT defines a fracture criterion instead of triggering and propagation. The fracture criterion is based on the calculation of the critical energy release rates for normal and shear separation Essentially, crack propagation occurs when $\mathbf{G}$ exceeds the critical energy release rate..

4.3   Material

The nylon 12 powder for SLS process is a melt-curing process and therefore the melting and crystallisation characteristics of nylon 12 powders are decisive for the sintering process and the final quality of the sintered part.

The melting process of crystalline polymers differs from that of low molecular crystals, which melt in a narrow temperature range of about 0.2°C. The melting process remains almost at a temperature where the two phases are in equilibrium until the crystals are completely melted. In contrast, the melting of crystalline polymers takes place over a wide temperature range, called the melting range, in which the crystalline polymer appears to melt and warm up at the same time. This is because crystalline polymers contain crystals of varying degrees of perfection, with the more imperfect crystals melting at a lower temperature and the more perfect crystals melting at a higher temperature. The melting point and melting range of crystalline polymers are less related to the size and distribution of the molecular weight than to the crystallisation history, the degree of crystallisation and the size of the spherical crystal. The lower the crystallisation temperature, the lower the

melting point and the wider the melting range; the higher the degree of crystallisation and the larger the spherical crystal, the higher the melting point. **Figure 4.3** shows the DSC curve of nylon 12 sintered material measured using a differential scanning calorimeter at a temperature rise rate of 10°C/min [162].
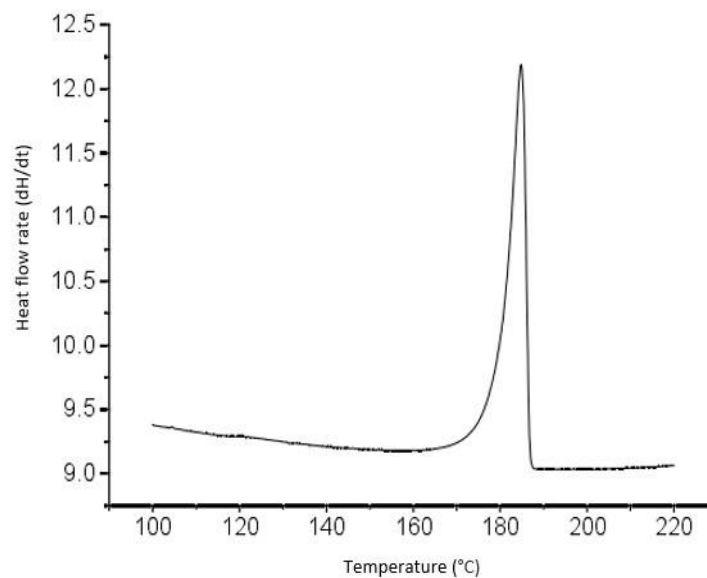
Figure 4.3: Sintered nylon 12 material DSC heating curve [162].

As can be seen in **Figure 4.3**, the sintered nylon 12 has a steeper melt peak, a higher melt onset temperature, a narrower melting range and a higher latent heat of fusion of 93.9 J/g as measured by DSC. These characteristics are all beneficial to the sintering process. Due to the higher melt onset temperature, the preheating temperature of the powder can be increased and the temperature gradient between the sintered layer and the surrounding powder can be reduced. The high latent heat of fusion prevents the powder particles adjacent to the laser scanning area from melting due to heat transfer, which helps to control the dimensional accuracy of the sintered part.

Nylon 12 crystallises as it cools from the molten state and the rate of crystallisation is very temperature dependent. Since the rate of crystallisation is the sum of the rate of nucleation and the rate of grain growth, the temperature dependence of the rate of crystallisation of nylon 12 is the result of the combined effect of the temperature dependence of both. At temperatures close to the melting point, nylon 12 molecular chain segments move vigorously, nuclei are not easily formed or the nuclei formed are unstable,

and the number of nuclei formed is small, making the total crystallisation rate small; as the temperature decreases, the rate of nuclei formation increases greatly, and at the same time, as the polymer chains have sufficient activity, they can easily diffuse to the nuclei and discharge into the lattice, so the grain growth rate also increases, so the total crystallisation rate When the temperature continues to decrease, although the nucleation rate continues to increase, the melt viscosity increases, the polymer chain segment diffusion ability decreases, and the grain generation rate slows down, resulting in a decrease in the total crystallisation rate; when the temperature is below T_g, the chain segment movement is "frozen", and the nucleation and When the temperature falls below T_g, the chain movement is "frozen" and both nucleation and grain growth rates are very low, making the crystallisation process practically impossible. **Figure 4.4** shows the DSC curve of the HS sintered material from the molten state at 220°C down to room temperature at a rate of 10°C/min.
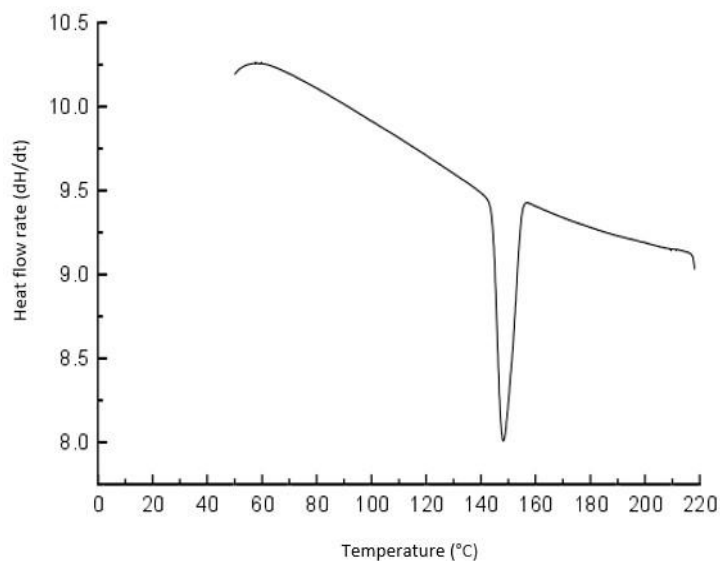
Figure 4.4: Sintered nylon 12 material DSC cooling curve [162].

The onset of crystallisation of the sintered nylon 12 was 154.8°C, the peak of the crystallisation peak was 148.2°C and the crystallisation termination temperature was 144.3°C. The crystallisation of the sintered material mainly occurs between 144.3°C and 154.8°C. Above 154.8°C, the crystallisation rate of the sintered material is slow and the

crystallisation process is difficult because the nuclei are not easily formed. difficult to carry out. The crystallisation rate can be adjusted by controlling the operating temperature during the sintering process to reduce the shrinkage stress caused by crystallisation. The tendency of the sintered part to failure due to shrinkage stresses caused by crystallisation can be reduced by controlling the operating temperature during sintering.

4.4   Test1: Effect of the location of nylon-12 inclusion within the domain of the crack behaviour

In this research, the computational result is to be compared with the numerical result shown in [27] to validate the XFEM fracture modelling technique based on VCCT and cohesive segment approach. Normally, the SLS printed parts are weaker in the build direction due to the inter-layer bonding mechanism. In this study, the interlayer strength is not considered and the 2D simulation is completed in a printed plane workpiece.

4.4.1   Simulation of FEM model

This section start with the concentrate on the evolution of an onset and propagation of microcracks FEM model. The model to be evaluated is able to anticipate how the DPM affects and controls crack initiation and propagation in SLS components. Therefore, in order to make the whole simulation similar to the actual SLS printed parts, additional assumptions and validations should be generated in the simulation. At the end of the section, the results of model evaluation will be analysed and discussed from various aspects. The FEM plane strain statics analysis will be carried out using the software package Abaqus/Standard 2017.

The geometrical analysis of the model in this research depends on the numerical result and the modelling information acquired from the research of J.Ibbett et al [27]. In order to save computer capacity and improve modelling efficiency, the model form is simplified from 3D to 2D. Commonly, the geometry of the printed component is considered as a cuboid in a normal 3D space. However, as the simulation developed in this section is in 2D, the circle is demonstrated as an un-melted particle, and the remaining part is represented as a melted particle.

A 30 mm long and 60 mm height workpiece shown in **Figure 4.5**, was to simulate to achieve a balance between accuracy and computational cost of the model. The chosen plate has an un-melted hole with 5 mm radius cantered at five different location (0, -23), (0, -19), (0, -15), (0, -11), (0, -7). *l* represents the distance between the centre of the inclusion and the centre of workpiece, and these five distinct locations of un-melted particle will be revealed in the result. Since J.Ibbett et al [27] only give the choice of the three locations for the study, the effect of the inclusion location within the domain of the crack behaviour cannot represent clearly. Furthermore, the direction of the crack need to be investigated by using more choices of the inclusion location. The crack edge has an initial length of 7.5 mm. A plane strain state is to be applied to increase loading to fracture acting on the workpiece and allowing crack progression.
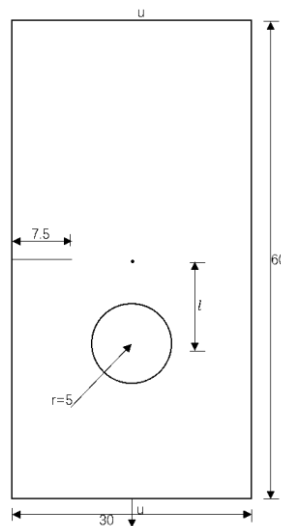
Figure 4.5: Geometry and boundary conditions of Test 1.

A range of literature have been researched which are the varying material properties and examining how the tensile strength and Young's modulus changed with energy density of printed parts. Duraform PA Nylon-12 (3D Systems) and PA12 powder grade (PA2200, EOS GmbH) are two most popular nylon-12 powder grades used in the literature [49]. These two types of nylon-12 powder are widely used in functional prototyping and, increasingly in SLS. The tensile properties of nylon-12 are specified by a set of different process parameters. According to **Table 4.1**, Hopkinson et al. [152] suggested that as energy density increases, Young's modulus, tensile strength and elongation at break of

nylon-12 printed part rise significantly. For instance, the range of Young' modulus increased from 2300 MPa to 2800 MPa when energy density changed from 0.0085 J/mm^2 to 0.012 J/mm^2. Ajoku et al. [148] and Caulfield et al. [163] studied the same grade of material, with marginal amount of energy density input and the whole range of print orientations and found that the tensile properties of part (from Ajoku et al. [148]) decrease slightly. However, due to different sets of processing parameters from Caulfield et al. [163], part bed temperature was extremely low, so Young's modulus dropped down dramatically but tensile strength had been remaining to be investigated. The similar behaviour was also found in Usher et al. [164] and Amado-Becker et al. [165] which illustrated that DPM grew, the tensile properties of final part increased. The range of tensile properties again varied noticeably, which was proven to be affected by water condition of powder and test temperature. In PA2200, the tensile properties seemed varied sightly, and also showed the similar trend as Duraform PA.
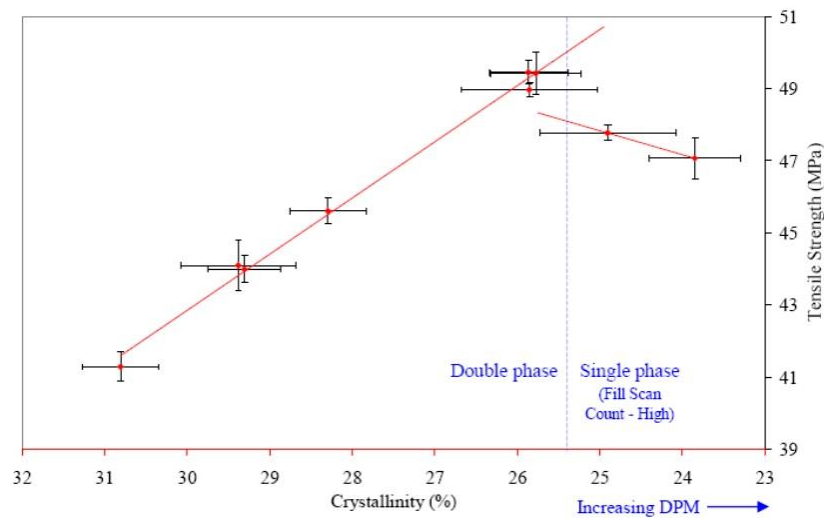
Figure 4.6: Effect of DPM on tensile strength [153].

Amado-Becker et al. [165] stated that as the density reached a maximum value of 977 (kg/mm^3) at an energy density of 0.032 (J/mm^2), the material behaved in an almost isotropic form, presenting average values for Young's modulus and Poisson's ratio, 2310 MPa and 0.408, respectively. Considering all of the literature investigated, it would seem sensible to accept 2000 MPa as ideal high-performance in Young's modulus. To assess a rough value of Young's modulus and tensile strength for un-melted cores, **Figure 4.6** from [153],

is used as reference. Referring to a certain point between 'single phase' structure and 'double phase' structure as mentioned in Section 4.1, the tensile strength and Young's modulus of un-melted cores around ten percent higher than the fully-melted material. Therefore, the value of Young's modulus in un-melted cores is set up as 2200 MPa in this case. The maximum principal stress for damage evolution is 10 MPa and normal mode fracture energy is 6.3 mJ/mm^2 corresponding to [166].

**Table 4.1: Parameters of SLS on Nylon-12 mechanical properties in the literature.**

Author	Material	Machine	Young's Modulus (MPa)	Tensile Strength (MPa)	Elongation at Break (%)	Energy Density (J/mm^2)	Key Factors
Hopkinson et al. [152]	Duraform PA	3D Systems SLS Vanguard	2300-2800	41-49	4-14	0.0085-0.012	DPM
Ajoku et al. [142]	Duraform PA	3D Systems SLS Vanguard	1800-2050	41-49	8-9	0.015	Print orientations
Caulfield et al. [163]	Duraform PA	DTM Sinterstation 2500	700-1100	-	5-16	0.0079-0.028	DPM and print orientations
Usher et al. [164]	Duraform PA	DTM Sinterstation 2500	600-1900	30-52	2-16	0.015-0.06	DPM and print orientations
AmadoBecker et al. [165]	Duraform PA	DTM SLS 125 former	500-2310	-	-	0.012-0.032	DPM
Salazar et al. [158]	Duraform PA	-	1720-2010	45-57	4.4-10	-	Temperature
Seltzer et al. [159]	Duraform PA	-	1170-1720	-	5-10	-	Water condition
Drummer et al. [167]	PA2200	DTM Sinterstation 2000	1600-2000	52-55	10-14	-	-
Dadbakhsh et al. [104]	PA2200	DTM Sinterstation 2500	-	32-35	16-18	0.056	Virgin and in-process aged powders
Majewski et al. [153]	PA2200	EOS Formiga P100	1250-3800	35-71	7.5-20	0.043	Thickness and print orientations
Brugo et al. [157]	PA2200	EOS Formiga P100	1600	58	15	0.056	-
Amel et al. [168]	PA2200	EOS Formiga P100	2000	47	6	0.056	-
Lammens et al. [166]	PA2200	EOS Formiga P395	1830-2100	46-57	3.6-15.5	-	Print orientations
Dewulf et al. [169]	PA2200	EOS Formiga P395	1520-1700	39-47	4.3-19	0.024-0.042	DPM
Cano et al. [110]	PA2200	-	550-2020	33-72	4-53.8	-	Temperature and print orientations

Crespo et al. [170]	PA2200	-	1700	45	20	-	-
Chen et al. [79]	PA12 (VESTOSINT)	HK P320 SLS system	300	39	70	0.015	-

4.4.2   Model validation

The basic principle of XFEM is to take into account known features of the solution of a problem in the approximation of the unknown field. In fracture mechanics, the displacement field is enriched with a discontinuous function across the crack surface, which allows the simulation of crack growth in a finite element framework without the need to build a conforming mesh at each step of the propagation, functions with singular derivative near the crack front that span the near-tip expansion of the displacement field, which improve the accuracy of the method. Even though the mesh does not need to match the crack surface, in practice, the size of its elements must be small enough with respect to characteristic lengths like the crack length and the crack radius of curvature. The mesh available from the structural analysis with the FEM of a safe component is not appropriate for the damage-tolerance analysis of this cracked component with the XFEM. For this reason, a mesh refining procedure tailored to the XFEM is desirable. A simple approach is to divide recursively the elements that are close to the crack until their size is deemed small enough. A more sound approach is to refine the mesh on the basis of an error estimation. In this case. the element meshing in this analysis is grounded on linear elastic solid element in **Figure 4.7**. The specimen is meshed randomly with a refined zone in the middle and un-melted parts by CPE4 elements (a 4-node bi-linear plane strain quadrilateral). The crack edges, un-melted part and the dotted line are meshed with h_{mid}, while dashed lines with h size finite elements. The trajectory of transition between the different zones are linear.
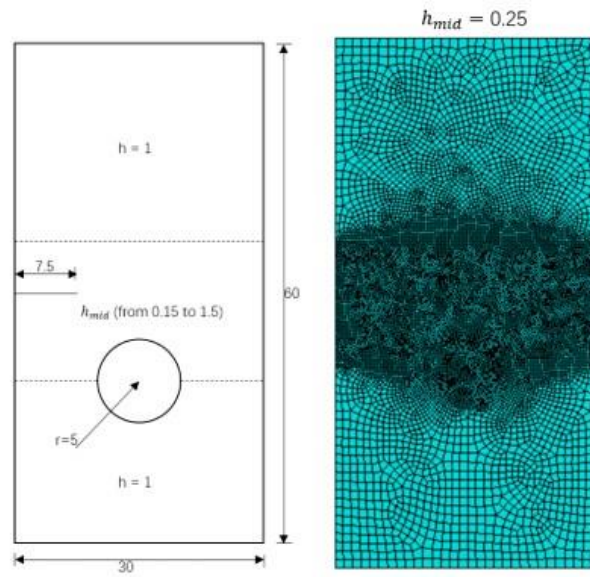
Figure 4.7: Schematic illustration of mesh seed distribution of Test 1 and finite element mesh for h_{mid}=0.25mm.

Mesh sensitivity analysis was intended to get the mesh size to its optimum scale which will generate a balance between certainty, running time, and storage (capacity). **Table 4.2** shows the result of the mesh sensitivity analysis on Test 1, when l equals 7 mm. The approximate global size of finite element (h) is set up as 1 mm. As the mesh size (h_{mid}) decreases, the amount of von mises stress, tresca stress and max principal increase dramatically. From **Figure 4.8**, it can be seen that after a mesh size (h_{mid}) of 0.25mm the stress values remaining unchanged by an appreciable amount, but there is an exponential rise in the number of nodes and elements, resulting in an increase of the running time and storage requirement but without much increase in the certainty of the stress. Hence, to guarantee the optimum performance, a mesh size (h_{mid}) of 0.25mm is selected for meshing both specimen models.

Table 4.2: Mesh sensitivity analysis results for Test 1, when l=7mm.

| Mesh Size h_{mid} (*mm*)	Von Mises Stress (*MPa*)	Tresca Stress (*MPa*)	Max Principal Stress (*MPa*)	Number of Nodes	Number of Elements
1.5	3.21E-01	4.03E-01	3.90E-01	1010	920
1.0	4.02E-01	5.64E-01	5.77E-01	2027	1901
0.75	4.69E-01	6.70E-01	6.80E-01	2629	2491
0.625	5.40E-01	7.75E-01	7.85E-01	3167	3020
0.5	6.02E-01	8.96E-01	8.99E-01	4091	3929
0.375	6.91E-01	1.00E+00	1.10E+00	5833	5645
0.3	7.79E-01	1.13E+00	1.23E+00	7985	7772
0.25	8.68E-01	1.25E+00	1.34E+00	10486	10249
0.225	8.86E-01	1.29E+00	1.39E+00	12355	12101
0.2	8.96E-01	1.32E+00	1.42E+00	14823	14545
0.15	9.06E-01	1.33E+00	1.45E+00	23703	23363
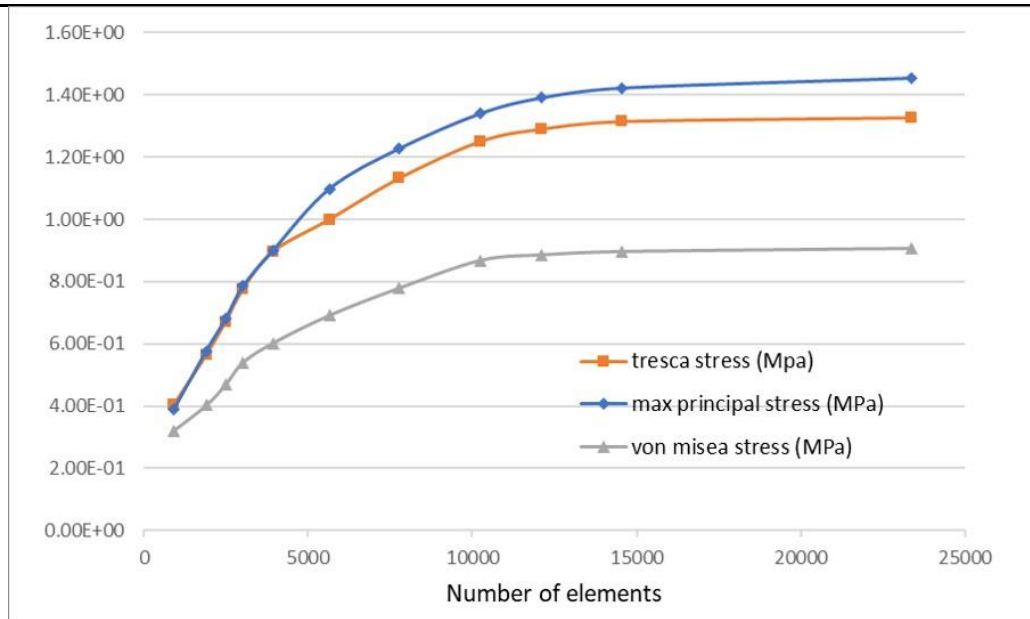
Figure 4.8: Mesh sensitivity analysis results for Test 1, when l=7mm.

Residual is calculated after running the regression model and it is the differences between the observed values and the estimated values. The norm of residuals is a measurement of the level of fitness, where the smaller the value is, the higher level of

fitness is, therefore it is applicable in validating this model by using **Equation 4.10**. f^{int} representing the internal energy, and f^{ext} representing the external energy.

The main function code for calculating the norm of residual in MATLAB is seen in Appendix A. This function is formed via the leading of the output data for internal energy and external energy. In order to apply **Equation 4.10**, the matrices of internal energy and external energy data are transferred to the vectors. Thus, the norm of residuals analysis results can be generated as **Figure 4.10** shown with most values in norm of residual below 0.5. It can be seen that from **Figure 4.10**, the values of the external energy and internal energy starting to grow at the beginning; when time is around 0.2, the external energy continue to grow, but the internal energy fall off to about 7 MPa. The reason to this phenomenon is that only takes about 0.2 time period to complete penetrating the whole plate, after which the plate is break into two parts, and the simulation only takes a few more time to finish the process. Therefore, it is energy dissipation due to penetration of the plate that makes external and internal energy different.

$$Norm\ of\ Residual \quad = \quad \frac{f^{int} - f^{ext}}{f^{ext}} \qquad\qquad (4.10)$$
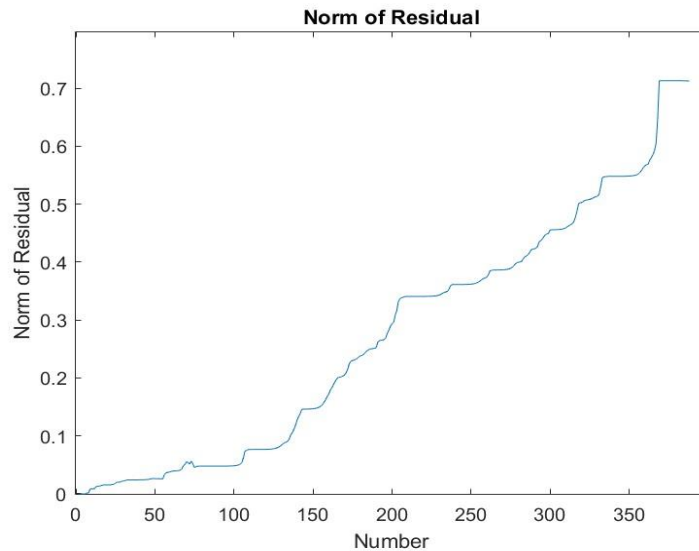
Figure 4.9: Norm of residuals analysis result.
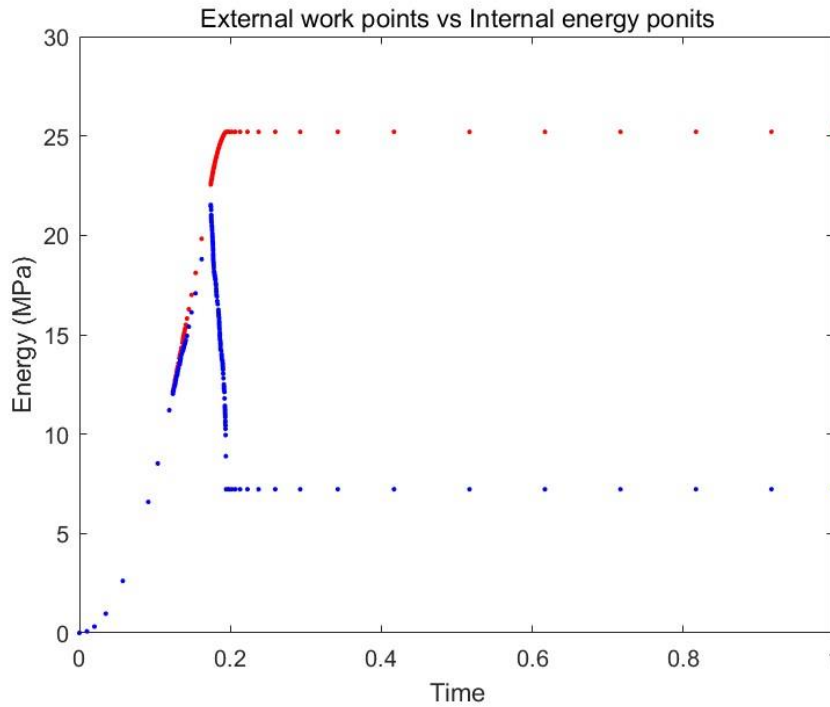
Figure 4.10: Comparison of the external energy and internal energy.

In addition, the crack behaviour measured in the simulations achieved a significant result in comparison with J.Ibbett et al. [27] results, as depicted in **Figure 4.11**. In the result of J.Ibbett et al. [27], since the crack did not penetrate the sample, the crack path is not the same as the result of the simulation. The values of stress field for the simulation and J.Ibbett et al results are similar. Furthermore, the inhouse code was used in J.Ibbett et al. [27], however, but the software package Abaqus/Standard 2017 was applied in this study. Different assumptions might be made for these two analyses. Therefore, the visual validation does not seem to be suitable for this study.
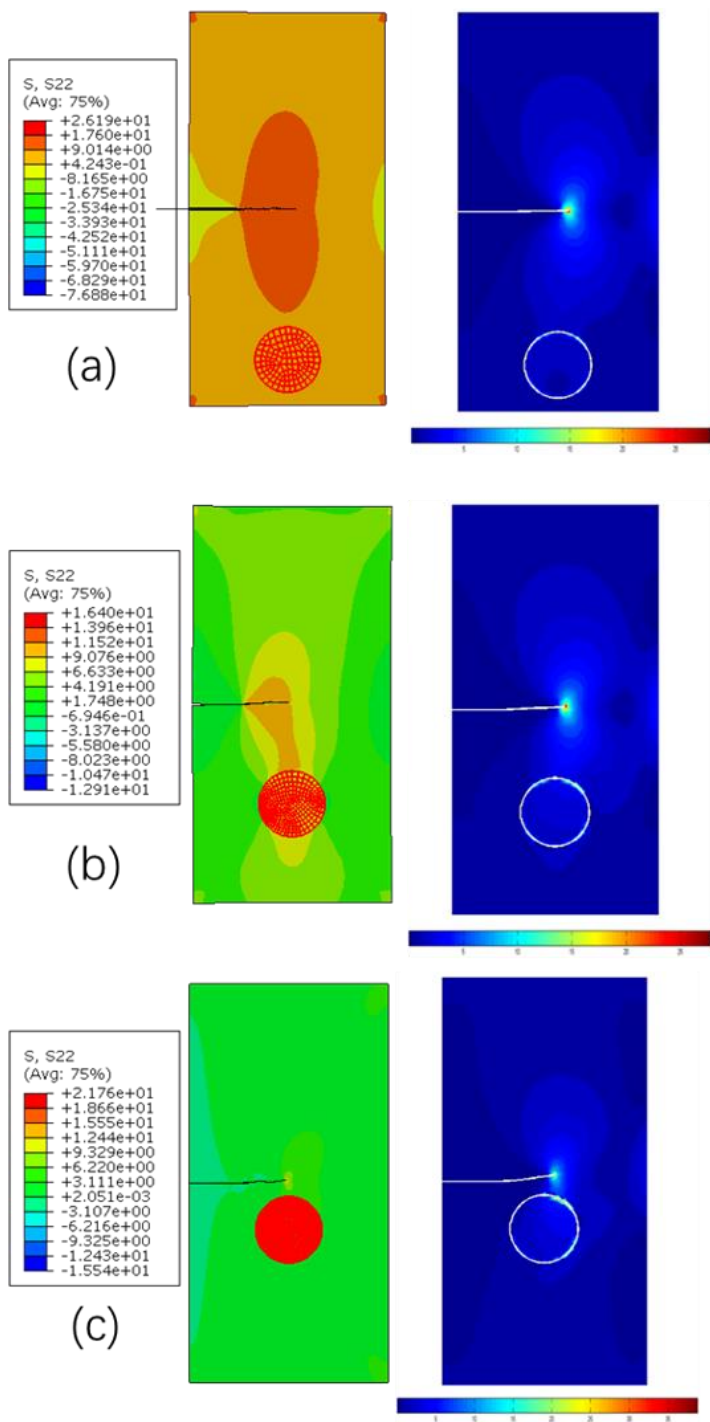
Figure 4.11: (a) l=23mm, (b) l=15mm, (c) l=7mm. Compare with computational crack propagation with different location of un-melted particles in Test 1 (lhs) and in J.Ibbett et al. Von-Mise stress field (MPa) results (rhs).

4.4.3   Results and discussion

According to **Figure 4.11**, the crack path only showed slightly different behaviour in distinct location of un-melted particles, but it is difficult to observe results of crack path and length. In XFEM simulation in Abaqus, there are two types of field output to describe the crack behaviour. Namely, PHILSM indicates signed distance function in describing the crack surface, and PSILSM indicates signed distance function in describing the initial crack front. However, the draft field output cannot generate crack length and geometric parameters of crack. To calculate the 2D crack length, firstly, the crack length of single element needs to be determined, and then the total length of the crack can be obtained by cumulative summation. Since the crack tip cannot stay inside the element, but not the boundary of element, it can be generally concluded that the crack is a straight line in the element. In **Figure 4.12**, the two intersection points of the crack on the boundary of the element can be found as it is determining by the position when PHILSM is equal to zero among those four nodes. Therefore, the geometric parameters of crack can be calculated. The CrackGeo V1.3 Plug-in was integrated within ABAQUS framework to indicate the crack path and length in zooming detailed by using this mechanism. The CrackGeo V1.3 is an ABAQUS post-processing plug-in. When the model uses XFEM and Cohesive elements to simulate cracks, it can extract two-dimensional and three-dimensional crack data, includes the number of cracked elements, the length of the crack and the final shape of the crack.
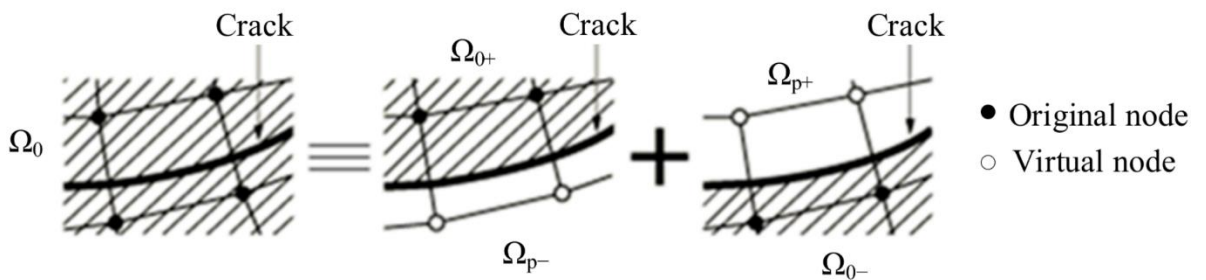

Figure 4.12: The mechanism of calculating the crack length.

In this case, the crack path and length were plotted in coordinate as **Figure 4.13-4.17** shown. In the crack path figures, the coordinates of pre-defined crack are from (-15,0) to (-7.5,0). The coordinates of the plate are (-15,30), (15,30), (15,30) and (15,-30). To get the

zooming detailed results, **Figure 4.13-4.17** only show the middle section of the plate. Therefore, the crack tip starts to open at point (-7.5,0), and then move upwards. Furthermore, the crack length unit (mm) was described as length against simulation time.

The stress/strain field near the inclusion is destroyed. When crack propagation is involved, the direction is affected by the nature and location of the particles, such as the opening displacement/mode. One of the focuses of this experiment is the impact of inclusion location and stiffness on crack growth under plane strain. **Figure 4.5** gives the definition of inclusion via analysis on un-melted particles. The particle size is used as the characteristic length of the sample, and the inclusion diameter is used to describe all sizes. The results show that the direction of crack propagation is immensely affected by inclusions.

Cracks attempt to stay away from inclusions, and the pattern is accelerated as the inclusions move closer to the initial position of the crack. Another examination that can be made by this test is **Figure 4.18** indicates that the interfacial stress tends to increase when the crack approaches the inclusion. There are two approaches, VCCT and cohesive segment approach, used in each simulation, which give a comparative result. In some cases in **Figure 4.13-4.17**, VCCT results are similar to the results of cohesive segment approach as **Figure 4.14**, **Figure 4.16** and **Figure 4.17** show, which enhanced the reliability of those results. Both results shows tortuous crack path, the crack path of VCCT result is generated more smoothly than the results of cohesive segment approach, and the reason to this phenomenon is that the method of VCCT opening crack is based on the combination of the critical energy release rates of normal and shear separation. This phenomenon can also be explained in crack length results, VCCT trend usually takes 0.2 simulation time to complete the crack growth, while the trend of cohesive segment approach is more linear. Therefore, The two approaches are in overall good agreement with each other, with the exception of the first instants of propagation where the cohesive segment approach process zone has to shape up, whereas the VCCT starts with a sharp crack.
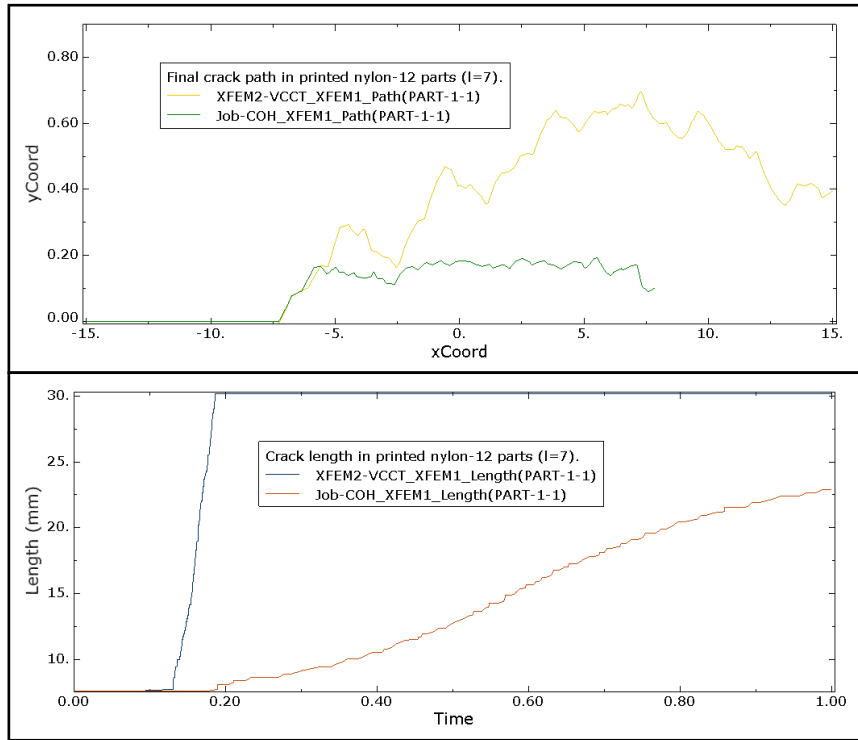
Figure 4.13: Zooming in crack path (upper figure) and crack length (bottom figure), coordinates in mm, when l=7mm.
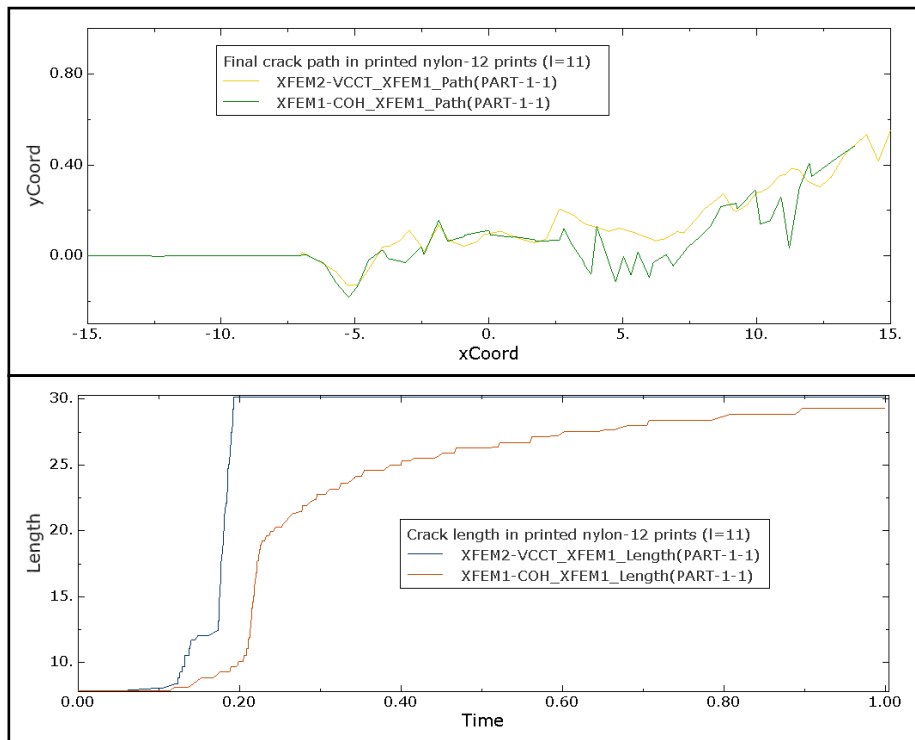
Figure 4.14: Zooming in crack path (upper figure) and crack length (bottom figure), coordinates in mm, when l=11mm.
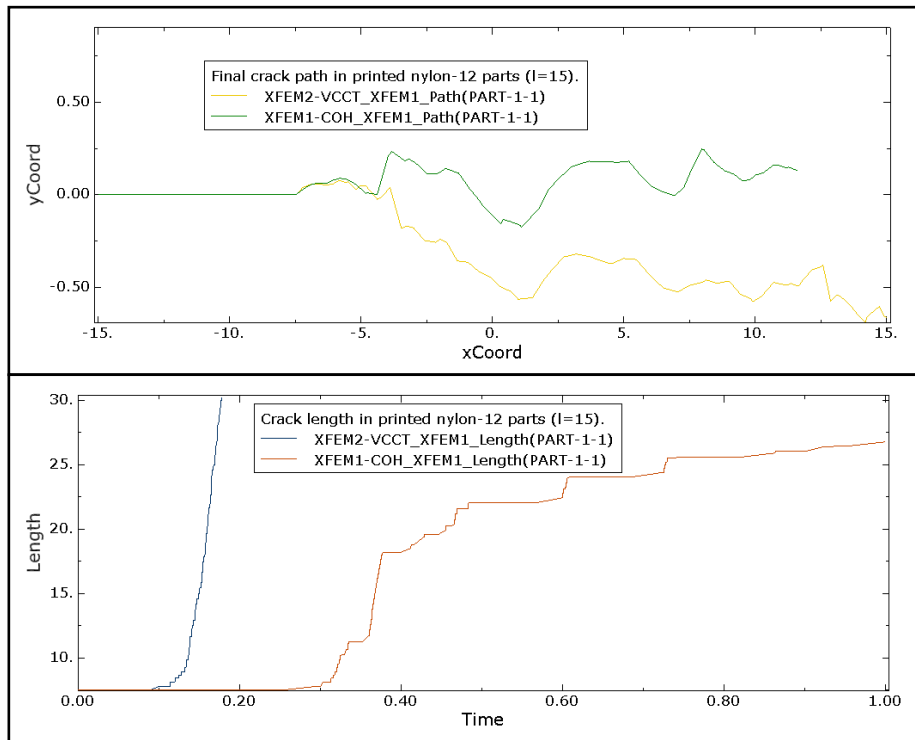
Figure 4.15: Zooming in crack path (upper figure) and crack length (bottom figure), coordinates in mm, when l=15mm.
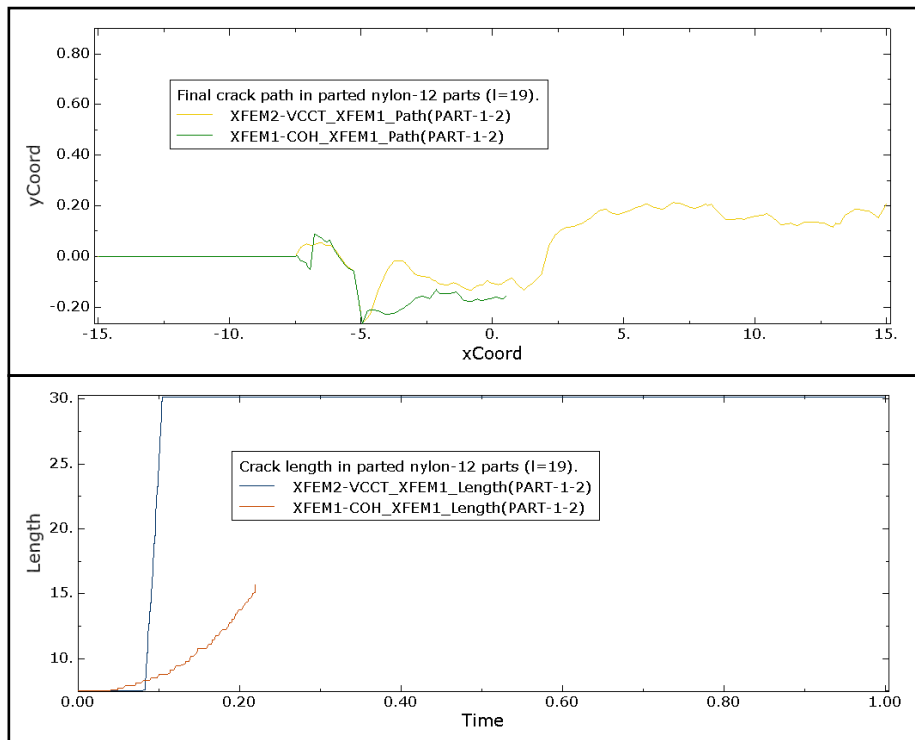

Figure 4.16: Zooming in crack path (upper figure) and crack length (bottom figure), coordinates in mm, when l=19mm.
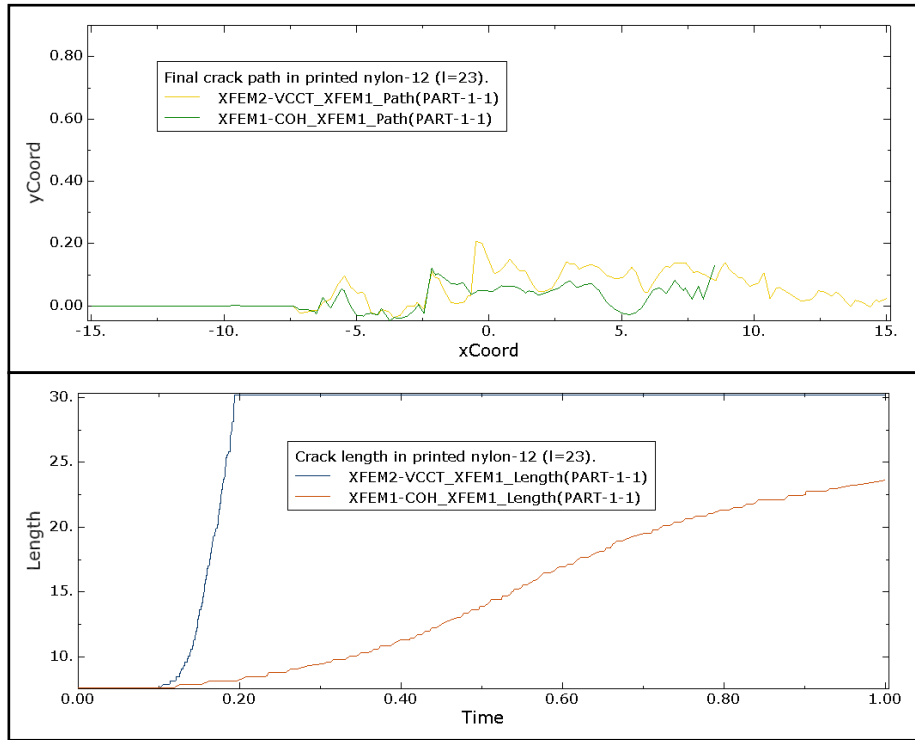
Figure 4.17: Zooming in crack path (upper figure) and crack length (bottom figure), coordinates in mm, when l=23mm.
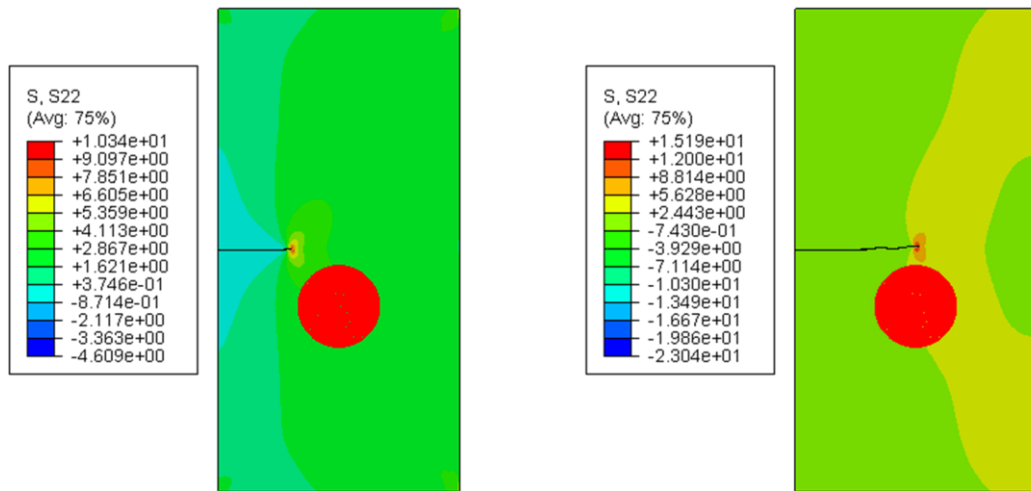
Figure 4.18: Figure depicting S22 stress field (MPa) and crack evolution: initial (lhs) and crack approaches the inclusion (rhs) when l=7mm.

4.5 Test 2: Effect of the proximity of two nylon-12 inclusions within the domain the crack path

The second experiment investigated how the proximity of two particles affects crack behaviour. By Setting up an offset edge crack in the sample, similar to the one in Test 1, adding two particle inclusions and leaving a small gap or "bottleneck" between them to observe the effect of the concentrated area between them. The aim of this experiment is whether particles will act as stress concentrators when they are close to each other, thereby inducing cracks to approach them. The accuracy of the second test will be examined by comparing with the numerical results reported in [27] as to justify the XFEM simulation based on VCCT and cohesive segment approaches. The numerical modelling is also to be adjusted to functions as more practical internal cracks under Mode I fatigue loading.

This section firstly introduces the simulation of FEM model, then the model validation will be presented. The results of simulation will be discussed based on the results of Test 1.

4.5.1   Simulation of FEM model
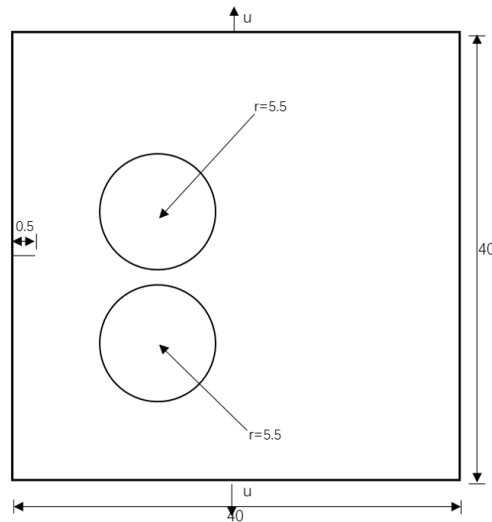
Figure 4.19: Geometry and boundary conditions of Test 2.

The software package Abaqus/Standard 2017 was used to predict the likely crack path for two particle inclusion's plate condition. In the analysis, the sample plate, 40 mm high and 40 mm wide was set up as shown in **Figure 4.19**. The pre-defined crack was approximated by taking very small initial length of 0.5 mm in the centre. The coordinates of inclusion centre locations are set up as (10, 5) and (10, -7) where both un-melted particles have 5.5 mm radius. There is only 1 mm gap between two un-melted particles, and the centre of this gap is 0.5 mm lower than the centre of the plate. Therefore, this gap can be used for examining the crack path and stress concentration. A plane strain state is applied with increased load to fracture further the workpiece and allow crack progression.

From Test 1, the same mechanical properties of nylon-12 is used in this section. The un-melted particles are assumed ten percent stiffer. The maximum principal stress for damage evolution is set up as 10 MPa and normal mode fracture energy is 6.3 mJ/mm^2 referring to [166].

4.5.2   Model validation

The plate FE model, as mentioned in Section 4.3, is based on linear elastic element (CPE4 element). **Figure 4.20** shows the increased number of elements is to allow the crack propagation and stress distributions between the two particles to be seen more clearly. The technique of mesh is free mesh, and the mesh algorithm is set up as advancing front.
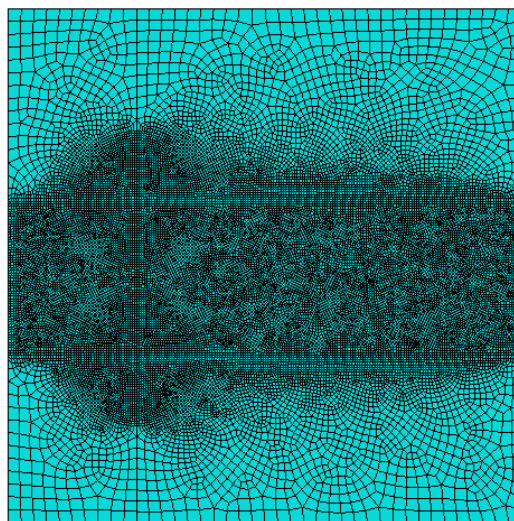
Figure 4.20: Schematic illustration of mesh seed distribution in Test 2.

In order to improve the mesh size, mesh sensitivity analysis has been implemented. The approximate global size of the element size is set up as 1 mm, and different local seeds of the element size start from 1 mm to 0.1mm. **Table 4.3** shows the result of the mesh sensitivity analysis for Test 2. As the mesh size decreases, the amount of von mises stress, tresca stress and max principal increase dramatically. In **Figure 4.21**, it can be seen that after a mesh size of 0.2 mm the stress values do not change with noticeable amount, but there is an exponential rise in the number of nodes and elements, which will result in an increase of the processor time and storage requirement but without much increase in the accuracy of the stress results. Hence, to get the optimum performance, a mesh size of 0.2 mm is selected for meshing both specimen models.

Furthermore, the crack behaviour measured in the simulations generated a significant result in comparison with J.Ibbett et al. [27] results, as depicted in **Figure 4.23**. In the result of J.Ibbett et al. [27], since the crack does not penetrate the sample, the crack path is not the same as the result of the simulation. The values of stress field for the simulation and J.Ibbett et al. results are similar. Furthermore, the in-house code was used in J.Ibbett et al. [27], but the software package Abaqus/Standard 2017 was applied in this study. Different assumptions are to be made for these two analyses.

Table 4.3: Mesh sensitivity analysis results for Test 2.

Mesh Size (*mm*)	Von Mises Stress (*MPa*)	Tresca Stress (*MPa*)	Max Principal Stress (*MPa*)	Number of Nodes	Number of Elements
1.0	4.11E-01	5.24E-01	5.89E-01	2111	2034
0.75	4.89E-01	6.20E-01	7.30E-01	2653	2566
0.625	5.50E-01	7.24E-01	8.95E-01	3804	3716
0.5	6.52E-01	8.46E-01	1.03E+00	5272	5179
0.45	7.49E-01	9.53E-01	1.13E+00	5766	5645
0.35	8.28E-01	1.06E+00	1.25E+00	9490	9387
0.3	8.88E-01	1.15E+00	1.34E+00	12208	12099
0.25	9.23E-01	1.23E+00	1.39E+00	16832	16700
0.2	9.56E-01	1.28E+00	1.47E+00	24751	24618
0.15	9.61E-01	1.30E+00	1.50E+00	41627	41474
0.1	9.66E-01	1.31E+00	1.53E+00	89362	89169
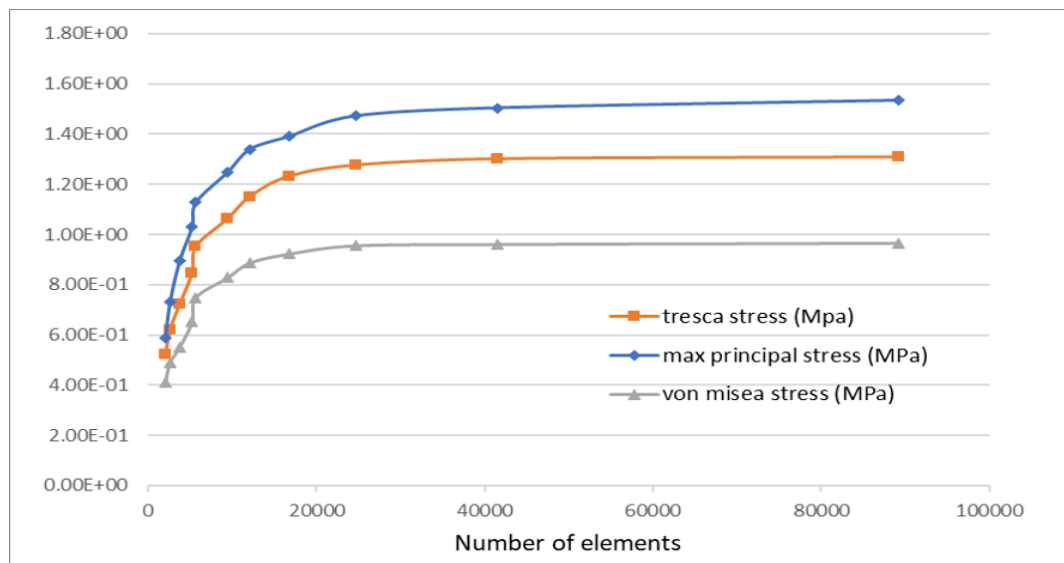
Figure 4.21: Mesh sensitivity analysis results for Test 2.
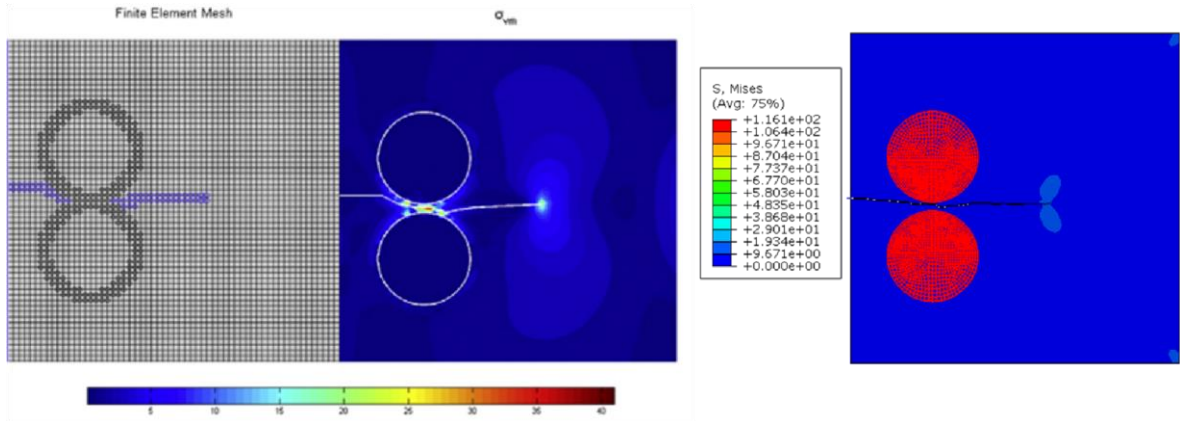
Figure 4.22: Compare with computational crack propagation affected by two nylon12 inclusions in Test 2 (rhs) and in J.Ibbett et al. Von-Mise stress field (MPa) results (lhs).

4.5.3 Results and discussion

It can be seen from **Figure 4.23** that the crack has steered towards the gap between the two particles and passed through the other side. Red regions between the two particles indicate a higher level of stress in graphs.
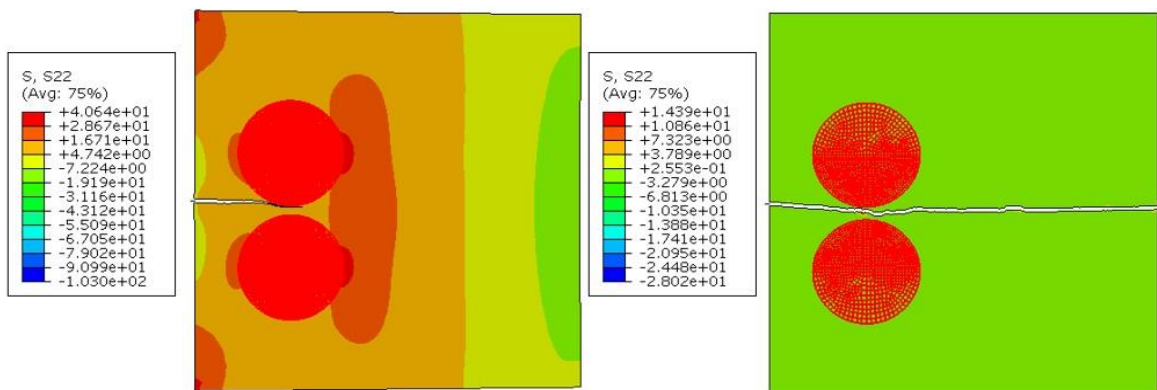
Figure 4.23: (a) l=23mm, (b) l=15mm, (c) l=7mm. Compare with computational crack propagation with different location of un-melted particles in Test 1 (lhs) and in J.Ibbett et al. Von-Mise stress field (MPa) results (rhs).

80

The CrackGeo V1.3 Plug-in was applied to indicate the crack path and length in zooming detailed as **Chapter 4.4.3** mentioned. Therefore, the crack path and length were plotted in coordinate as **Figure 4.24** shown. In the crack path figures, the coordinates of pre-defined crack are from (-20,0) to (-19.5,0). **Figure 4.24** only shows the middle section of the plate. Therefore, the crack tip starts to open at point (-19.5,0), and then move downward. Furthermore, the crack length unit (mm) was described as length against simulation time.

Test 2 affirms that a 'bottle neck' of two particles triggers the crack 'steering' towards that location, where the proximity leads to an extreme concentration and increase of the stresses. This would certainly result in fatal damage of the material in most cases.
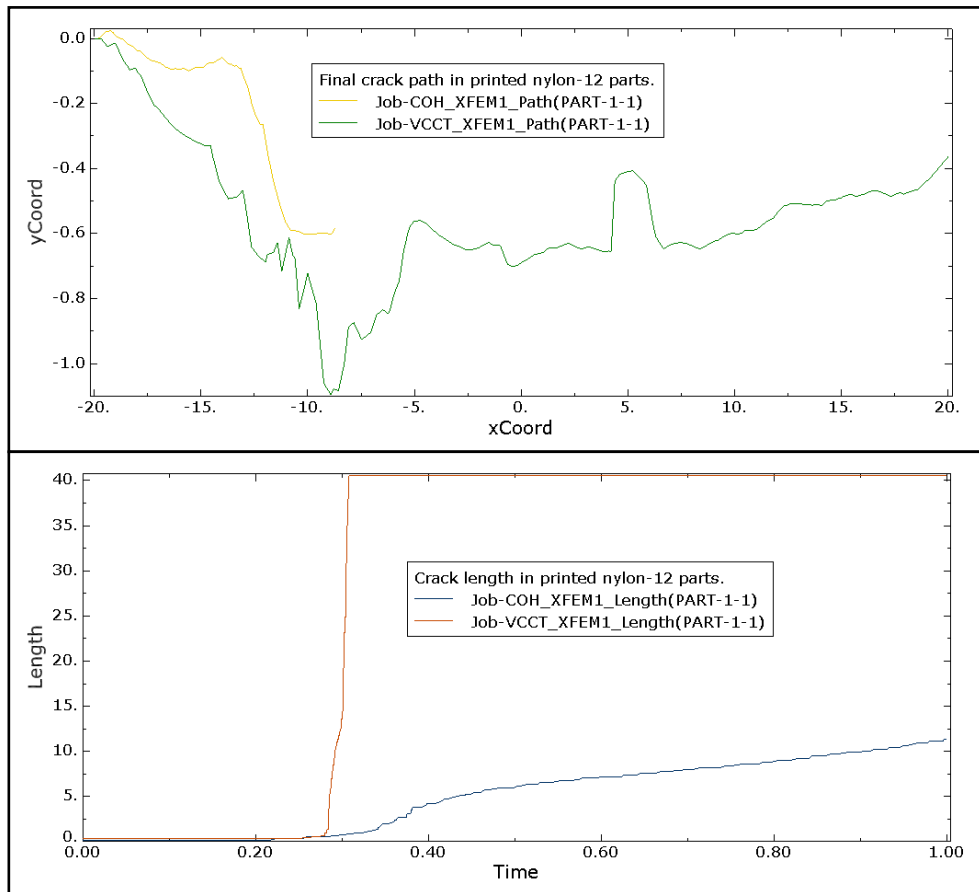
Figure 4.24: Zooming in of Test 2 in crack path (upper figure) and crack length (bottom figure), coordinates in mm.

4.6 Test 3: Effect of porosity within the domain of crack behaviour

During the use of SLS components in the real world, pores are highly likely to become unstable. In contrast to pore morphologies, sizes and their arrangement lead to different stress distributions in the component. Moreover, micro-cracks inevitably exist in SLS components. Under the influence of holes, the stress concentration generated at the tips of the micro-cracks can easily lead to their unstable growth. Therefore, it is a matter of strong significance to study the influence of the interaction between cracks and holes on the stress field at the crack tip. In this section, we take a SLS printed component with randomly distributed hole morphology size as an example to simplify the mechanical behaviours such as crack growth during the use of SLS printed parts, and study the interaction between cracks and holes, in order to predict the crack propagation path.

Test 3 simulation is closer to a real case. The geometrical configuration of porosity arrangement has been reproduced from [152].

4.6.1 Simulation of porous structure model

Generally, pore morphology can be approximately round or elliptical, single or randomly distributed. According to the SEM photographs of SLS parts, the calculation model can be simplified to a basic configuration which includes both round and elliptical holes; moreover, the development of contemporary modelling technology makes it possible to prepare SLS parts with controllable porosity. Therefore, in this section the ordered arrangement of porous structures is studied.
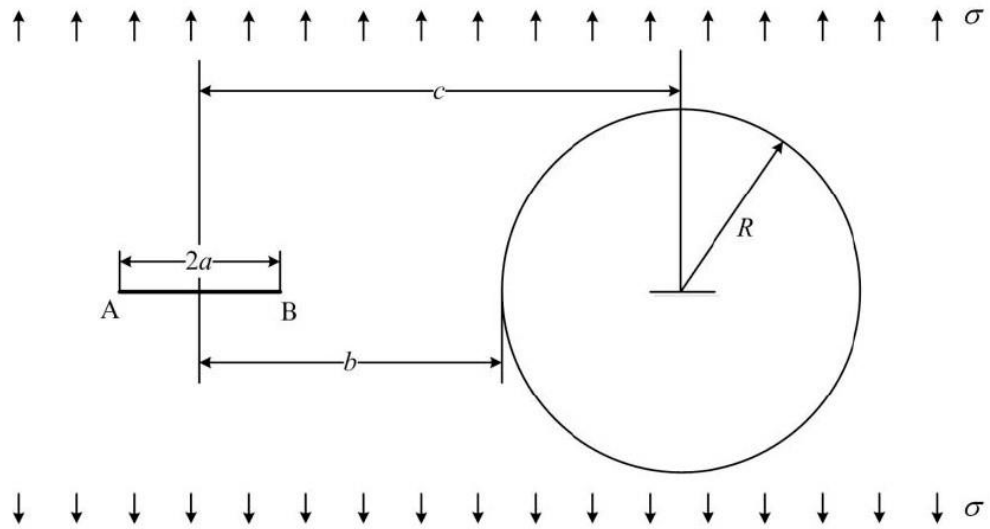
Figure 4.25: The basic configuration of a crack near a circular hole subjected to uniform normal stress

The model used for reliability verification is shown in **Figure 4.25**. There is a crack with a length of 2a in the infinite plate. A circular hole with a radius R is close to the crack. The centre of the circular hole is on the crack extension line. The distance between the crack centre and the hole circumference is b, and the distance between the crack centre and the hole centre is c=1m, the infinite plate bears uniform normal stress in the direction perpendicular to the crack surface. Taking the half length of the crack as: a=0.1, 0.2, 0.3, 0.4, 0.5m, the radius of the hole R=0.1, 0.2, 0.3, 0.4, 0.5m, both ends bear uniform normal stress σ=1.0Pa, elastic modulus E=1000Pa, Poisson's ratio = 0.25. It can be observed that, for XFEM, the boundaries of cracks and holes are independent of the grid boundary.
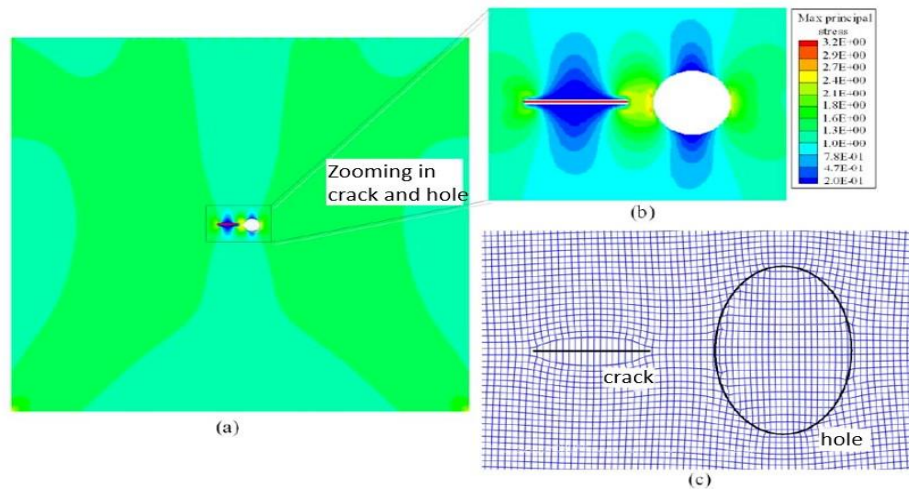
Figure 4.26: (a) The maximum principal stress diagram; (b) Zooming in the maximum principal stress diagram of cracks and round holes; (c) Mesh deformation diagram (deformation magnification 20 times).

Figure 4.26 (a) is the maximum principal stress diagram of the above model (a=0.4m, R=0.3m). The maximum principal stress diagram of the crack and circular hole area is enlarged as shown in **Figure 4.26** (b), **Figure 4.26** (c) is a grid deformation diagram magnified 20 times. It can be seen from the figure that the grid of cracks and circular hole boundaries penetrating the cell is opened under normal stress.

Figures 4.27 are respectively (a) Displacement diagram in the x direction (b) Displacement diagram in the y direction; (c) Stress diagram in the x direction; (d) Stress diagram in y direction; (e) Shear stress diagram. It can be seen from the figure that the existence of holes affects the stress distribution of the crack tip field, that is, the crack tip closer to the circular hole has a larger stress value. Therefore, this section focuses on the crack tip on the side of the hole, and studies the interaction between the crack and the hole and the influence of the hole on the stress field at the crack tip. To analyse the feature of this interaction, the calculation result of the normalised stress intensity factor is shown in **Figure 4.28**.
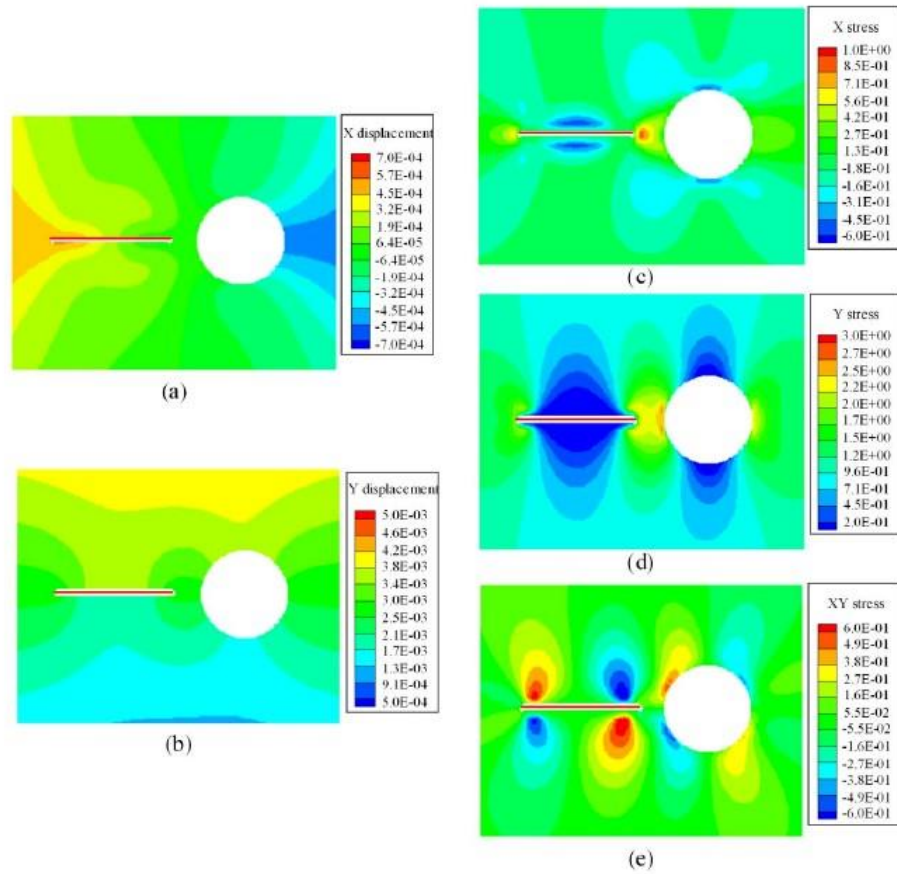
Figure 4.27: (a) Displacement diagram in the x direction; (b) Displacement diagram in the y direction; (c) Stress diagram in the x direction; (d) Stress diagram in y direction; (e) Shear stress diagram.

Figure 4.28 shows that, with the increase of the crack length, F_1 shows an increasing trend, and the longer the crack length and the closer to the hole, the faster F_1 increases. In addition, as the aperture size increases, F_1 increases accordingly. When a/b is equal, the larger the aperture size, the larger the F_1. The above results illustrate that the crack length and aperture size affect the normalised crack tip stress intensity factor F_1 to varying degrees. When the pore size is small, the F_1 retains a small value, and when the pore size increases, the F_1 increases significantly. The a/b related to the crack length also affects F_1. F_1 increases nonlinearly with the increase of a/b. The larger the a/b value, the greater the increase in the F_1 value. The above results are also consistent with the literature referenced [10].
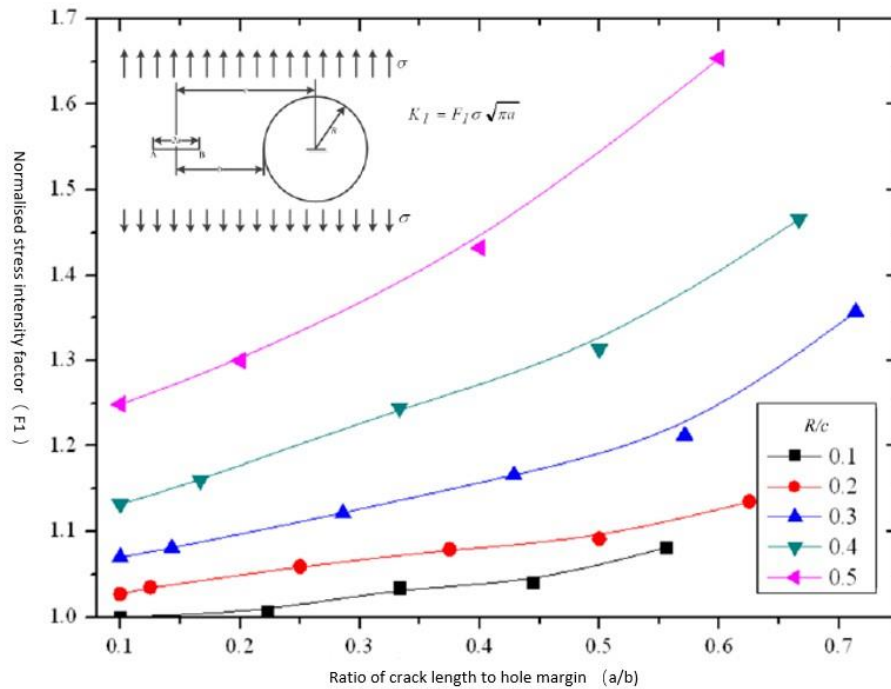
Figure 4.28: Normalised stress intensity factor F_1 vs. a/b
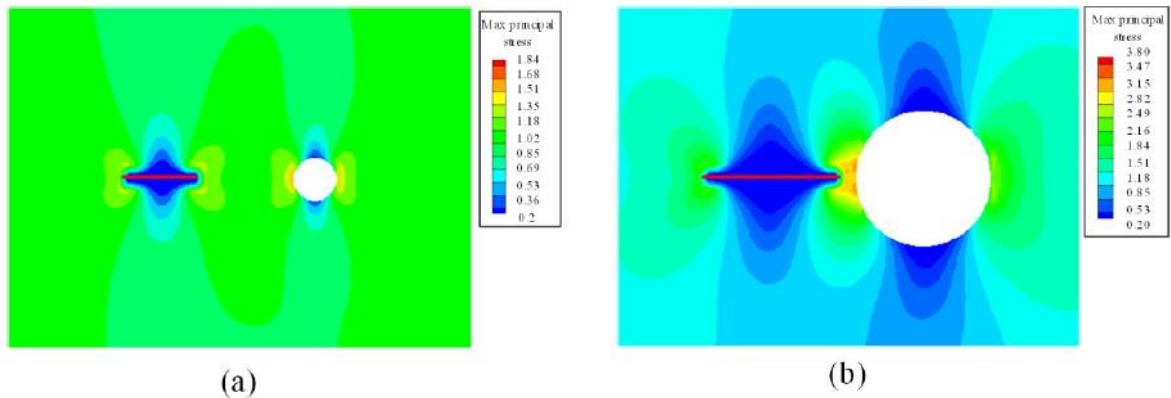
Figure 4.29: **Contour plots of different crack lengths and hole sizes**

Figures 4.29 are respectively: (a) the maximum principal stress diagram with half crack length a=0.2m and circular hole radius R=0.1m. (b) The maximum principal stress diagram with half crack length a=0.4m and circular hole radius R=0.3m; from **Figure 4.29 (a)**, it can be seen that, when the crack is shorter and the radius of the hole is smaller, the stress at the crack tip of the field is less affected by holes. It can be seen from **Figure 4.29 (b)**

that, when the radius of the crack and the hole increases, the stress field of the crack tip near the hole is strongly affected by the hole, and the stress intensity factor at the crack tip also increases sharply. This leads to rapid destruction of the material.

4.6.2   Simulation of the SLS model

According to Hopkinson et al. [152], the manufacturing parameters of SLS's printed parts are applied as shown in **Table 4.4**. The part bed point is set up as 148◦C, with a scan speed of 6300mm/s, scan spacing of 0.15mm and laser power set at 9.5W. Under these parameters, Young's modulus of the final SLS printed part is 1019MPa and Poisson's ratio is 0.344.

Table 4.4: Build parameters used to produce the SLS part in Test 3 [152].

Part bed set-point	Scan speed (mm/s)	Scan spacing (mm)	Laser power W
148	6300	0.15	9.5
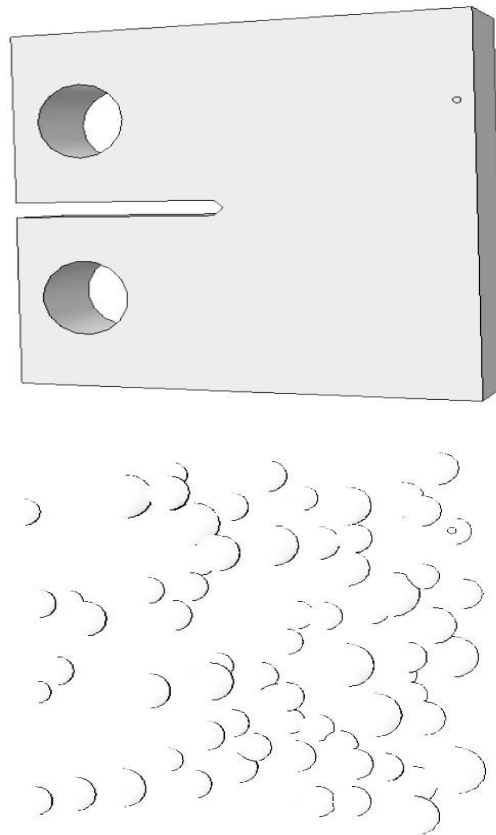
Figure 4.30: **The upper figure: the geometry of SLS printed part; the bottom figure: the inside location of the holes.**

For SLS printed parts, DPM not only affects the un-melted particles, but also influences the porosity of the part. As the DPM increases, the porosity of the part drops significantly. **Figure 4.30** illustrates the geometries of SLS printed part from the standard compact specimen (ASTM E1820-11) and the inside location of holes is random. Some results are shown from **Figure 4.31** by applying the technique in Test 1 and Test 2.

It can be noted that there is no significant difference in the crack path of the 3D SLS model, even it is already zooming in. Since the location of the holes is quite complicated in this coordinate system, there is no effective way to analyse the effect of holes in cracks of the SLS model. Furthermore, simulation of the simplified SLS 2D model is discussed in the next section.
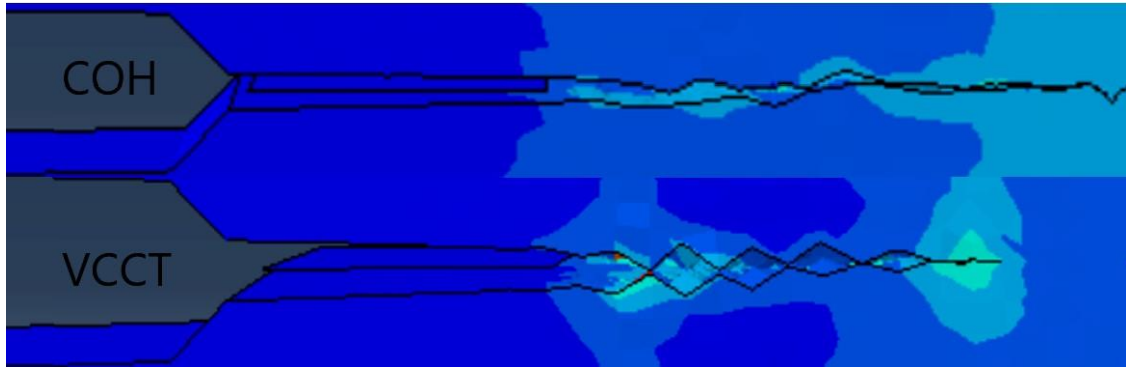
Figure 4.31: **Zooming in crack path of SLS printed part in COH (upper figure) and VCCT (bottom figure).**

4.6.3   Simulation of simplified SLS model
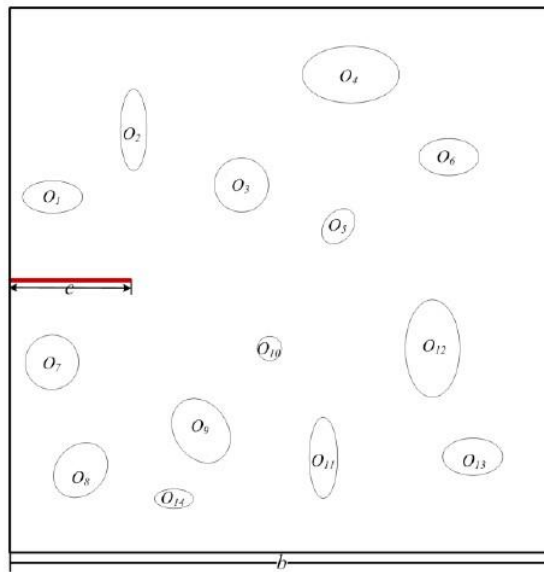
Figure 4.32: **Extraction of model in SLS printed parts**

As illustrated by **Figure 4.32**, a square plate with side length **b** = 5mm, and edge crack **c** = 1.1mm, the upper end fixed, the lower end model containing uniform normal stress ζ and shear stress η, elastic modulus **E** = $1019 MPa$, Poisson's ratio **v** = 0.344 is used. For all 14 holes, the morphology and size are shown in **Table 4.5**, where (take the lower left corner of the plate as the origin, x_0 is the x-coordinate of the pore centre, y_0 is the y-coordinate of

the coordinate centre, R_a is the long axis radius, and R_b is the short axis radius, θ is the angle between the long axis and the x-axis direction).

Table 4.5: **The hole size of the printed SLS part**

No. of holes	x_0 (mm)	y_0 mm	R_a (mm)	R_b (mm)	θ
1	0.38	3.25	0.28	0.17	0.00
2	1.13	3.88	0.38	0.13	90.0
3	2.13	3.38	0.25	0.25	–
4	3.13	4.38	0.45	0.26	0.00
5	3.00	3.00	0.18	0.13	66.3
6	4.00	3.63	0.28	0.17	0.00
7	0.38	1.75	0.25	0.25	–
8	0.63	0.75	0.28	0.22	63.5
9	1.75	1.13	0.32	0.25	116.6
10	2.38	1.88	0.11	0.11	–
11	2.88	0.88	0.38	0.13	90.0
12	3.38	1.88	0.45	0.26	90.0
13	4.25	0.88	0.28	0.17	0.00
14	1.50	0.50	0.18	0.09	0.00

The crack propagation path of the SLS printed parts with different loading ratios is simulated and predicted, and the manufacturing process of porous SLS printed parts is also considered. In this section, this process is simulated as an increase in porosity, that is, an increase in pore size. The crack propagation is synchronised, and the crack propagation step length is selected as one-eighth of the crack length in the previous step. For porous SLS printed part with different pore sizes, the step length is selected as 1/20 - 1/30 of the long axis and short axis of the pore size. In this section, the porous SLS printed parts under different loading ratios are studied. At the same time, the above crack growth and hole expansion modes are selected for calculation. Through calculation, it can be seen that the loading ratio has a greater influence on the crack growth path.
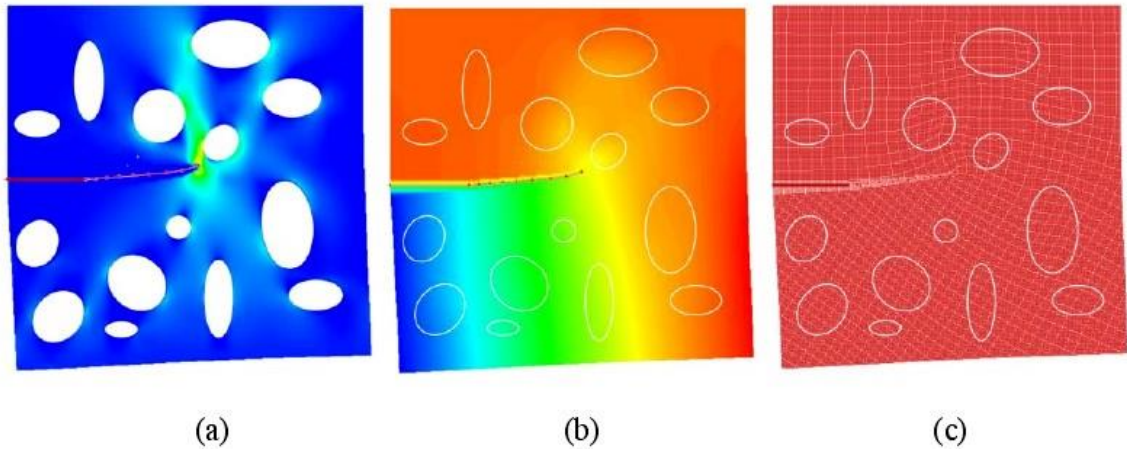
**Figure 4.33: Diagram of calculation results (loading in y direction at the bottom):
(a) maximum principal stress; (b) displacement in y direction; (c) Mesh deformation
diagram.**

When the loading at the bottom end is 10MPa, the crack firstly deflects slightly upwards, and its angle is smaller. It is more affected by holes 3, 5, and 10 which are closer to the crack tip, and it finally it deflects to hole 5.
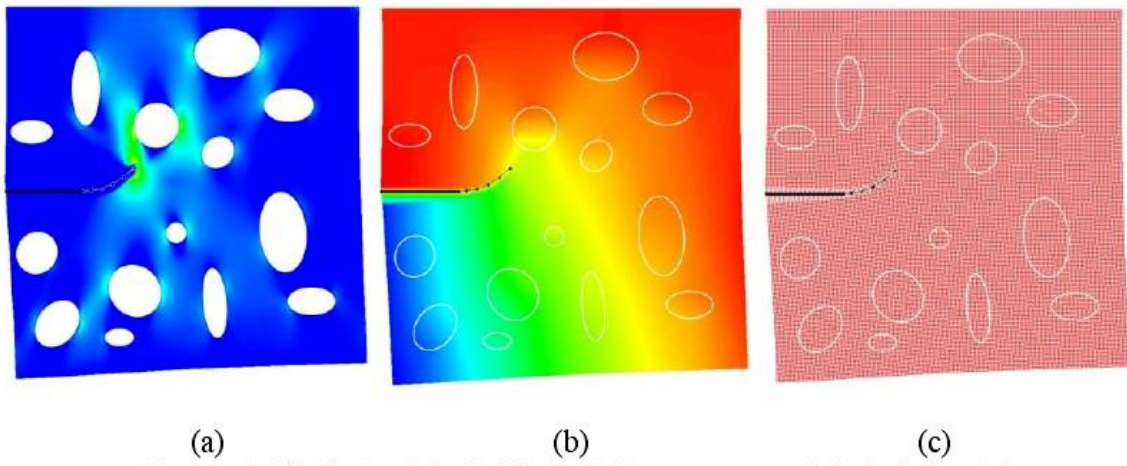
**Figure 4.34: Diagram of calculation results (loading ratio 1:2 at the bottom)
(a) maximum principal stress; (b) displacement in y direction; (c) Mesh deformation
diagram.**

When the loading ratio is 1:2 at the bottom, as shown in **Figure 4.34**, the initial expansion angle is larger than that under vertical loading. With the occurrence of hole reaming, the crack is most affected by hole 3, and it is expanding. After a short path, it deflects to the hole 3 and finally penetrates the hole 3.

4.7   Summary

In XFEM, by introducing the enrichment function of the crack strong discontinuity problem and the enrichment function of the weak discontinuity inclusion into the displacement solution space, the boundary of these discontinuities is independent of the physical grid, thereby reducing dependence on it; whilst improving efficiency, it meets the accuracy requirements. Based on the extended finite element method, the interaction between the un-melted particles, porosity and the crack propagation of the matrix is studied. During the crack propagation, the optimisation algorithm in **Section 4.2** is used to further improve the calculation efficiency.

Three tests indicated that the DPM has a critical effect on the crack behaviour of SLS printed engineering part under load. The mechanism of how un-melted particles affect crack behaviour was examined in **Section 4.4** and **4.5**. It was seen that the location, number and size of un-melted particles bring about significant changes in crack length and path. Moreover, the volume of the holes affects the crack path as mentioned in **Section 4.6**. According to the results of three tests, the role of the DPM in the crack behaviour of SLS printed engineering part can be summarised as follows:

- As un-melted particle is close to the initial crack, and the crack seeks to stay away from the un-melted particle. However, this change in the crack's direction is too small or sometimes has few discernible effects.

- As un-melted particle is closer to a crack, the crack path is more strongly influenced.

- The existence of a 'bottle neck' of two un-melted particles has the most critical effect on a crack path.

- As the hole is close to initial crack, the crack seeks to stay close to the hole.

Based on these findings summarised during the SLS process, it is important to optimise the value of the DPM and decrease the area of un-melted particles and holes. Therefore, the failure resistance of final printed part will be enhanced. In order to obtain more significant results, further material applications require consideration.

Chapter 5

Study of microcracks in thermoelastic fracture mechanics obtained by SLS

Selective laser sintering (SLS) of powder is a complex manufacturing process, involving a series of processes such as the interaction between a certain laser and material, the theory of powder sintering, and the physical and chemical changes involved in the forming process. In order to take a comprehensive approach to the SLS process and gain a detailed understanding of how to better promote its development, continuous in-depth study of the laser sintering mechanism is required. After years of investigation, academics have established that the temperature field, stress field and their changes play a vital role in the SLS fracture problem, which is useful in the study of the process mechanism and further discussion of the deformation and cracking of the workpiece during the sintering process.

XFEM has a range of advantages including: adaptability to complex geometric configurations, applicability to various fracture problems, reliability based on rigorous theory, and high efficiency suitable for computer aided implementation. It has become the most widely used numerical calculation method in engineering fracture analysis. Currently, analysis of, and research into, SLS temperature field and stress fields is mainly reliant on the finite element method.

In this Chapter, the crack under thermomechanical loading is analysed by XFEM. The method studied here uses XFEM formulation which can be enriched both in thermal and mechanical fields. Firstly, beginning with the background of SLS printed parts and XFEM in thermoelastic fracture mechanics, the related governing equations are presented in **Section 5.2**, after which the simulation of the thermoelastic fracture FEM model is provided. The results are given for a square plate with a central crack.

5.1   Background

Today, the thermoelastic crack issue has become increasingly important because many engineering components work under thermal and mechanical load. Several analytical and numerical approaches can be applied to address and seek to resolve these issues. For example, June et al. studied a square plate with a central crack and initial crack. Modified mapping-collection and complex variable approach was used, followed by measurement of the SIF of the part.

The numerical approach can usually handle more complicated problems than the analytical approach. There are many different numerical approaches, such as the finite element method (FEM), the boundary element method (BEM) and XFEM. Many authors [171, 172] report that XFEM is used in shear problems with thermal load, whereas few papers apply XFEM to the thermoelastic fracture problem. For the crack extension situation, XFEM can predict the SIF without precise mesh.

5.2   Numerical implementation

In the process of SLS, powder materials retain heat exchange processes such as convection, radiation, and thermal alternation. They continue to obey the laws described by the above-mentioned temperature and stress fields governing equations. However, selective laser sintering has its own elements, for example, powder materials. The asynchrony coefficient is generally significantly different from the inherent coefficient of the material. Generally, the resonance coefficient of powder materials is very low, and the thermal and physical properties of the material, such as its inductance coefficient, undergo significant change during the laser sintering process. In the selective laser sintering, when analysing the temperature field, the change in the material's thermophysical properties requires consideration. Meanwhile, phase change and laser Gaussian distribution also have a strong influence on temperature field distribution. These are all factors which should be considered for SLS thermoelastic fracture mechanics analysis.

The formulae for static linear isotropic thermal problems are:

$$\begin{aligned}
\mathbf{q} &= -k\nabla T \\
-\nabla\mathbf{q} + \bar{Q} &= 0 \\
\varepsilon &= \nabla_s\mathbf{u} \\
\varepsilon_T &= \alpha\,(T - T_0)\,\mathbf{I} \\
\sigma &= \mathbf{C} : (\varepsilon - \varepsilon_T) \\
\nabla\cdot\sigma + \bar{\mathbf{b}} &= 0
\end{aligned}$$

$$(5.1)$$

These formulae are in domain Ω bounded by ΓT which represents the temperature field, $\mathbf{q}$ is the heat flux, the displacement field is defined as u, ε represents the strain tensor and the stress tensor is defined as σ. Further, k is the diffusivity of the material, α represents the expansion coefficient and the isotropic fourth-order Hooke tensor is defined as $\mathbf{C}$.

In thermoelastic situation, the room of justifiable temperature and displacement field can be measured by:

$$T = \left\{ T \in H_1(\Omega) : T = \bar{T} \text{ on } \Gamma_T \text{ and } T \text{ discontinuous on } \Gamma_c \right\}$$
$$U = \left\{ \mathbf{u} \in H_1^3(\Omega) : \mathbf{u} = \bar{\mathbf{u}} \text{ on } \Gamma_u \text{ and } \mathbf{u} \text{ discontinuous on } \Gamma_c \right\}$$

$$(5.2)$$

Therefore, the XFEM includes the displacement field U and shape function $N_i(\mathbf{x})$. They are calculated from a crack-independent grid and take into account displacement jumps on the crack surface as well as stress singularities at the crack tip, where the enrichment function is multiplied by the shape function.

$$\mathbf{u}^h(\mathbf{x}) = \sum_i N_i(\mathbf{x})\mathbf{u}_i + \sum_{j\in J} N_j(\mathbf{x})h(\mathbf{x})\mathbf{a}_j + \sum_{k\in K} N_k(\mathbf{x})\left(\sum_{l=1}^4 \gamma_l(\mathbf{x})\mathbf{b}_{kl}\right)$$

$$(5.3)$$

96

5.3 Simulation of the FEM model
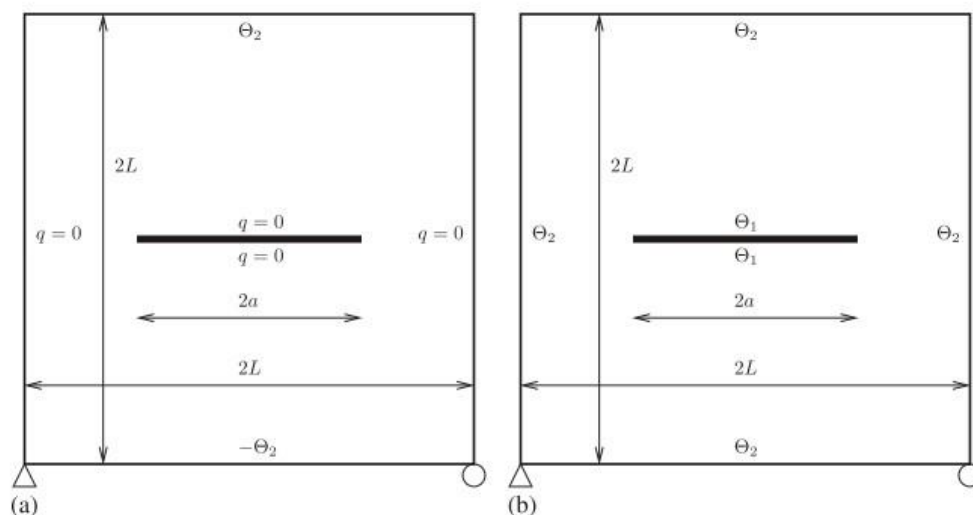
Figure 5.1: The plate with a crack in the middle: (a) adiabatic and (b) isothermal.

Simulation for the crack problem with thermal load is presented in this section. The mechanical properties of the material are set up as: Young's modulus is defined as $2.184 * 10^5 Pa$, Poisson's ratio is 0.3 and the coefficient of linear expansion is $1.67 * 10^{-5} per°C$.

To justify the ability of the numerical implementation for the temperature field by applying XFEM, the plate with a crack in the middle is exposed to two different groups of boundary conditions: **Figure 5.1(a)** shows a heat flux acts on the crack surface perpendicular under the adiabatic situation, **Figure 5.1(b)** demonstrates that the heat flux θ_1 acts on the crack in the middle and another heat flux θ_2 enforced at the plate boundary. $\theta_2 > \theta_1 = 0$. The length of the plate is 1, the radius of the crack a ranges from 0.1 to 0.6 with a step of 0.1. The element meshing in this analysis is 2933 nodes and 5868 elements, with the uniform characteristic length set up as 0.025.

5.4   Results and discussion

Figure 5.2 shows the temperature field in the plate with a centre crack under the adiabatic condition, and **Figure 5.3** demonstrates the temperature field in the plate with a centre crack under the isothermal condition when the radius of the crack $a = 0.3$.
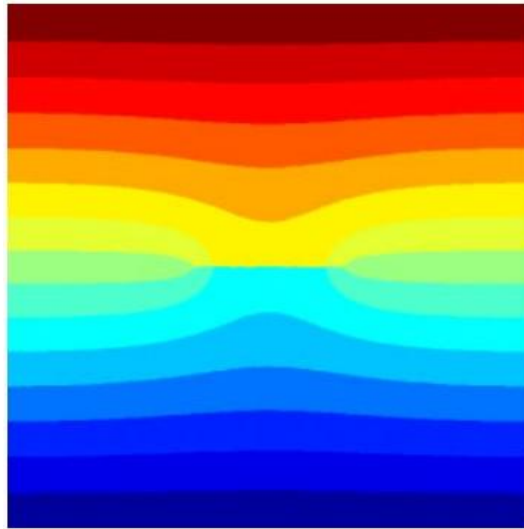
Figure 5.2: **Diagram of the temperature field in the plate with a centre crack (adiabatic)**
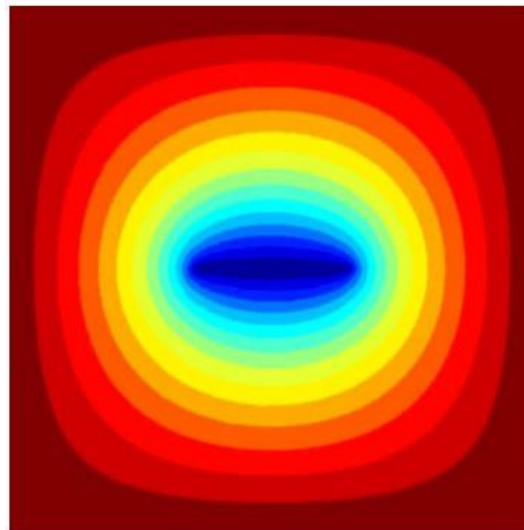
Figure 5.3:

Diagram of the temperature field in the plate with a centre crack(isothermal)

Table 5.1 indicates the comparison between the calculation, handbook [173] and [174]. The SIF is normalised by $\alpha(\Theta_2 - \Theta_1)E\sqrt{L}$. These results are very close to the literature [173, 174].

–

Table 5.1: **Calculation of normalised SIF**

a/W	Adiabatic crack (FII)			Isothermal crack (FI)		
	This test	**[36]**	**[93]**	**This test**	**[36]**	**[93]**
0.1	0.019	0.018	0.021	0.268	0.268	0.271
0.2	0.054	0.054	0.053	0.350	0.347	0.347
0.3	0.096	0.095	0.094	0.405	0.401	0.406
0.4	0.141	0.141	0.141	0.455	0.448	0.453
0.5	0.191	0.190	0.188	0.496	0.491	0.491
0.6	0.245	0.243	0.247	0.533	0.525	0.526

The deviation of the calculated SIF with the mesh sensitivity analysis result is shown in **Figure 5.4** as *a* is equal to 0.5. With characteristic length ranging from 0.01 to 0.1, separate mesh element sizes are applied. Unless using the large number of mesh element size, all results of the calculated SIF are within 0.7% for both conditions.
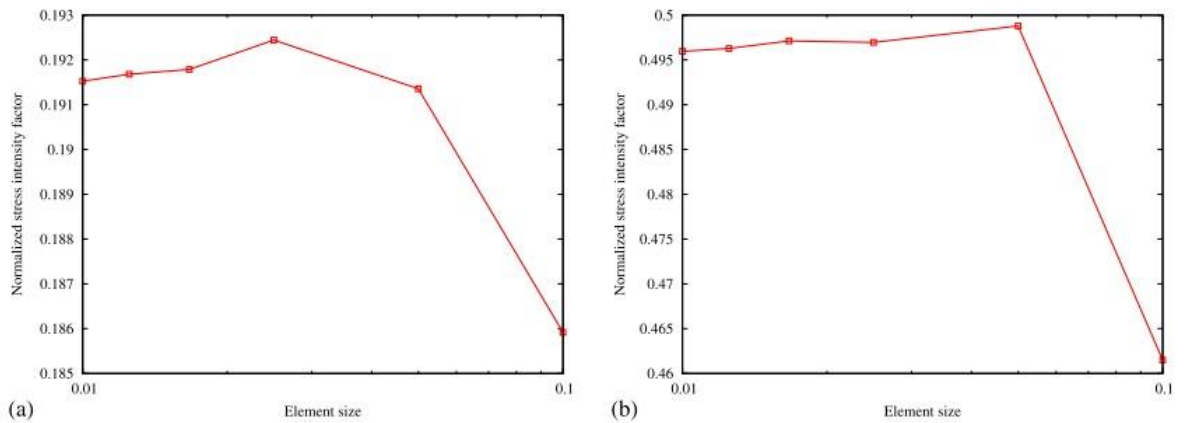
Figure 5.4: Mesh sensitivity analysis results of normalised SIF

Chapter 6

Conclusion

6.1 Conclusions

Microcracks are a common phenomenon in the SLS process, where the polymer powder material is cooled from its molten state during the sintering process, causing volume shrinkage due to temperature changes. There is a large volume change from the molten to the crystalline state, and the volume shrinkage comprises two parts, one being the volume shrinkage from the solidification of the melt and the other being the volume shrinkage from the crystallisation. When a polymer is in its molten state, the arrangement of the macromolecular chains is disordered. During crystallisation, the macromolecular chains are partly arranged in an orderly manner, and the gaps between the molecular chains are reduced; the higher the degree of crystallisation, the greater the reduction of such gaps and the greater the volume contraction. As a result, crystalline polymers have a stronger tendency to form shrinkage than non-crystalline polymers, and microcracks tend to be greater and more severe. Microcracks become a major process problem in the sintering of crystalline polymers.

The DPM is defined by the proportions of the existence of both melted and crystallised parts, and un-melted particles within the component. The amount of energy density input to the part can change the DPM of the final part; as the DPM increases, the volume of un-melted particles and porosity decreases. It should be noted that, when the amount of energy density input increases, but after a certain DPM point, the mechanical properties and fracture performance of the SLS printed part begin to drop.

In this paper, three tests are established on the improved sample models by the use of the ABAQUS finite element analysis platform, combined with the XFEM in order to simulate the influence of inclusions and holes on the deflection of the crack propagation path. In order to quantify the degree of influence, the CrackGeo V1.3 plug-in was used to indicate the crack path and length in zoomed detail. Un-melted particles were close to the

initial crack, and the crack attempted to stay away from the un-melted particle; as the hole was close to initial crack, the crack attempted to stay close to the hole. The existence of a 'bottle neck' of two un-melted particles has the most critical effect on the crack path.

Two approaches, VCCT and the cohesive segment approach, were used in each simulation. In some cases, the VCCT results were similar to the results of cohesive segment approach, however, the crack path of VCCT results is usually generated more smoothly than the results of the cohesive segment approach. The reason for this phenomenon is that the method of VCCT opening crack is based on the combination of the critical energy release rates of normal and shear separation. This phenomenon can also be explained in crack length results; the VCCT trend usually takes 0.2 simulation time to complete crack growth, while the trend of the cohesive segment approach is more linear. Therefore, the two approaches are in overall strong concurrence, with the exception of the first instance of propagation, where the cohesive segment approaching the process zone has to shape up, whereas the VCCT starts with a sharp crack. The cohesive segment approach is easier to use, and performs more efficiently, as the computation is lower down, at one order of magnitude, despite the less capable hardware used to run the analyses.

Further, the XFEM can be used to analyse the thermoelastic fracture problem. The displacement field of XFEM discretisation is similar to the temperature field discretisation. The test indicates that XFEM allows steady-state 2D thermoelastic problems to be dealt with precisely on a mesh independent of the location and length of the crack.

6.2 Limitations and suggestions for future studies

Fatigue crack growth of SLS printed part containing holes and inclusions is, in reality, a very complex problem, involving chemical composition, metallography, fracture macro analysis, and other factors. Due to the fact that this paper is mainly a numerical simulation of crack growth behaviour, the research content has various actual shortcomings. The analysis in this paper is generally designed to contain macroscopic material defects, but in reality actual material defects are not entirely macroscopic. In addition, in order to simplify the model, the defects studied in this paper are of regular shape, while the actual material defect shapes are diverse, and multiple types of inclusions and holes may coexist.

For SLS printed part, based on the research by [152], the crystallinity of a fully melted part and powder itself was found to be 25% and 47% respectively. Further to this, from the DSC data the Melted and Crystallised Material (MCM) crystallinity can be calculated along with the core crystallinity defined as being (1-%MCM), the DPM can be calculated using **Equation 4.1**. According to the inclusion size relative to the crystalline structure in **Chapter 4.4** and **Chapter 4.5**, the size of inclusion model can represent the crack of SLS printed part behave theoretically in the inclusion condition.

Generally, the radius of the hole is approximately $200\ \mu m$ in SLS printed part [175]. However, for the SLS model in **Chapter 4.6**, the size, orientation, aspect ratio for each holes are set up as SEM imaging of really part [175]. The location of each holes is random.

This paper does not classify crack propagation into inclusion particles and holes; it is necessary to simulate the trajectory of the crack propagation after entering the inclusion particles and holes in order to gain a clearer understanding of the influence of DPM and crack propagation. Moreover, this paper only considers nylon-12. In terms of practical problems, the properties of materials are diverse, thus a wider selection of material should be examined.

The three-dimensional crack characterisation and methods currently used are not perfect. When the crack passes through the part of the structure with a sharp increase in cross-sectional area, its shape is seriously distorted, which leads to errors in the simulation results. In order to improve the stability of the algorithm, it is necessary to propose a more complete three-dimensional crack characterisation and update the method of XFEM in future.

This paper does not consider crack growth in 3D thermoelastic fracture problem, therefore further investigation of this should be undertaken.

The volume shrinkage of sintered materials due to densification during sintering occurs mainly in the Z-direction, i.e. the height of the sintered layer decreases after sintering, which has little effect on the warpage of the sintered part in the XY plane (the first few layers). When sintering the first layer, if the temperature of the powder bed is low, there is a large temperature difference between the laser swept sintered layer and the surrounding powder; the sintered layer is quickly cooled and crystallised, resulting in shrinkage and curling of the edges of the sintered layer. When the curl is greater, the powder rollers

remove the first layer when the next layer is laid, rendering it impossible to continue the sintering process and necessitating a new sintering. During subsequent sintering, there is a tendency for microcracks to reduce gradually, but if the temperature difference between the newly laid powder and the sintered layer is large, this can nevertheless cause the fracture of the sintered part.

Strict control of the sintering temperature can resolve the fracture problem of sintered materials. When the powder bed temperature is close to the melting point of nylon 12, the laser input energy is just sufficient to melt the nylon 12, i.e. the laser only provides the heat required to melt the nylon 12, and there is no excess heat to raise the temperature of the sintered layer, thus avoiding fracture under such sintering conditions. Due to the low melt viscosity of nylon 12, the sintering process is quickly completed, resulting in a dense sintered layer. The temperature difference between the sintered layer and the surrounding powder is close to the melting point of nylon 12, so that the shrinkage stress caused by the temperature difference is minimal and can be released by stress relaxation. The temperature of the newly laid powder layer also quickly approaches the melting point of nylon 12 due to infrared heating and interfacial heat transfer, and the temperature difference with the previous layer is so small that it does not cause shrinkage of the previous layer. Microcracks can be avoided by controlling the cooling rate once the entire sintered part has been produced.

References

[1] K. Wong and A. Hernandez, "A Review of Additive Manufacturing", *ISRN Mechanical Engineering*, vol. 2012, pp. 1-10, 2012. Available: 10.5402/2012/208760.

[2] N. Guo and M. Leu, "Additive manufacturing: technology, applications and research needs", *Frontiers of Mechanical Engineering*, vol. 8, no. 3, pp. 215-243, 2013. Available: 10.1007/s11465-013-0248-8.

[3] K. Prakash, T. Nancharaih and V. Rao, "Additive Manufacturing Techniques in Manufacturing -An Overview", *Materials Today: Proceedings*, vol. 5, no. 2, pp. 3873-3882, 2018. Available: 10.1016/j.matpr.2017.11.642.

[4] A. Dass and A. Moridi, "State of the Art in Directed Energy Deposition: From Additive Manufacturing to Materials Design", *Coatings*, vol. 9, no. 7, p. 418, 2019. Available: 10.3390/coatings9070418.

[5] C. Seepersad, "Challenges and Opportunities in Design for Additive Manufacturing", *3D Printing and Additive Manufacturing*, vol. 1, no. 1, pp. 10-13, 2014. Available: 10.1089/3dp.2013.0006.

[6] C. Hull et al., "Rapid prototyping: current technology and future potential", *Rapid Prototyping Journal*, vol. 1, no. 1, pp. 11-19, 1995. Available: 10.1108/13552549510732026.

[7] M. Berzins, T. Childs and G. Ryder, "The Selective Laser Sintering of Polycarbonate", *CIRP Annals*, vol. 45, no. 1, pp. 187-190, 1996. Available: 10.1016/s0007-8506(07)63044-3.

[8] T. Ziegler, R. Jaeger and C. Koplin, "A design, mechanical rating, and load adaptation method for cellular components for additive manufacturing", *The International Journal of Advanced Manufacturing Technology*, vol. 90, no. 9-12, pp. 2875-2884, 2016. Available: 10.1007/s00170-016-9615-z.

[9] Y. Huang, M. Leu, J. Mazumder and A. Donmez, "Additive Manufacturing: Current State, Future Potential, Gaps and Needs, and Recommendations", *Journal of Manufacturing Science and Engineering*, vol. 137, no. 1, 2015. Available: 10.1115/1.4028725.

[10] X. Bai, H. Zhang and G. Wang, "Modeling of the moving induction heating used as secondary heat source in weld-based additive manufacturing", *The International Journal of Advanced Manufacturing Technology*, vol. 77, no. 1-4, pp. 717-727, 2014. Available: 10.1007/s00170-014-6475-2.

[11] S. Yang and Y. Zhao, "Additive manufacturing-enabled design theory and methodology: a critical review", *The International Journal of Advanced Manufacturing Technology*, vol. 80, no. 1-4, pp. 327-342, 2015. Available: 10.1007/s00170-015-6994-5.

[12] H. Lee, C. Lim, M. Low, N. Tham, V. Murukeshan and Y. Kim, "Lasers in additive manufacturing: A review", *International Journal of Precision Engineering and Manufacturing-Green Technology*, vol. 4, no. 3, pp. 307-322, 2017. Available: 10.1007/s40684-017-0037-7.

[13] A. Babaytsev, M. Prokofiev and L. Rabinskiy, "Mechanical properties and microstructure of stainless steel manufactured by selective laser sintering", *Nanoscience and Technology: An International Journal*, vol. 8, no. 4, pp. 359-366, 2017. Available: 10.1615/nanoscitechnolintj.v8.i4.60.

[14] D. Zindani and K. Kumar, "An insight into additive manufacturing of fiber reinforced polymer composite", *International Journal of Lightweight Materials and Manufacture*, vol. 2, no. 4, pp. 267-278, 2019. Available: 10.1016/j.ijlmm.2019.08.004.

[15] S. Ford and M. Despeisse, "Additive manufacturing and sustainability: an exploratory study of the advantages and challenges", *Journal of Cleaner Production*, vol. 137, pp. 1573-1587, 2016. Available: 10.1016/j.jclepro.2016.04.150.

[16] X. Zhang and Y. Liao, "A phase-field model for solid-state selective laser sintering of metallic materials", *Powder Technology*, vol. 339, pp. 677-685, 2018. Available: 10.1016/j.powtec.2018.08.025.

[17] S. Hosseini, H. Bayesteh and S. Mohammadi, "Thermo-mechanical XFEM crack propagation analysis of functionally graded materials", *Materials Science and Engineering: A*, vol. 561, pp. 285-302, 2013. Available: 10.1016/j.msea.2012.10.043.

[18] A. Bandyopadhyay and B. Heer, "Additive manufacturing of multi-material structures", *Materials Science and Engineering: R: Reports*, vol. 129, pp. 1-16, 2018. Available: 10.1016/j.mser.2018.04.001.

[19] A. Majeed et al., "A big data-driven framework for sustainable and smart additive manufacturing", *Robotics and Computer-Integrated Manufacturing*, vol. 67, p. 102026, 2021. Available: 10.1016/j.rcim.2020.102026.

[20] J. Plocher and A. Panesar, "Review on design and structural optimisation in additive manufacturing: Towards next-generation lightweight structures", *Materials & Design*, vol. 183, p. 108164, 2019. Available: 10.1016/j.matdes.2019.108164.

[21] R. Ganeriwala and T. Zohdi, "A coupled discrete element-finite difference model of selective laser sintering", *Granular Matter*, vol. 18, no. 2, 2016. Available: 10.1007/s10035-016-0626-0.

[22] T. Mayer, G. Brändle, A. Schönenberger and R. Eberlein, "Simulation and validation of residual deformations in additive manufacturing of metal parts", *Heliyon*, vol. 6, no. 5, p. e03987, 2020. Available: 10.1016/j.heliyon.2020.e03987.

[23] T. Anderson, *Fracture Mechanics - Fundamentals and Applications*, 4th ed. New York: CRC Press, 2017.

[24] K. Bathe, *Finite Element Procedures in Engineering Analysis*, 3rd ed. Prentice-Hall., 1984.

[25] D. Driver, "Discrete Element Multiphysical Models for Additive Manufacturing in conjunction with a Domain Specific Language for Computational Mechanics", Ph.D, UC Berkeley, 2015.

[26] F. Matthews, G. Davies, D. Hitchings and C. Soutis, *Finite Element Modelling of Composite Materials and Structures*, 2nd ed. Elsevier, 2000.

[27] J. Ibbett, B. Tafazzolimoghaddam, H. Hernandez Delgadillo and J. Curiel-Sosa, "What triggers a microcrack in printed engineering parts produced by selective laser sintering on the first place?", *Materials & Design*, vol. 88, pp. 588-597, 2015. Available: 10.1016/j.matdes.2015.09.026.

[28] Paolo Ferro, Filippo Berto and Luca Romanin, "Understanding powder bed fusion additive manufacturing phenomena via numerical simulation", *Frattura ed Integrità Strutturale*, vol. 14, no. 53, pp. 252-284, 2020. Available: 10.3221/igf-esis.53.21.

[29] J. Niu, H. Choo and W. Sun, "Finite element analysis and experimental study of plastic lattice structures manufactured by selective laser sintering", *Proceedings of the Institution of Mechanical Engineers, Part L: Journal of Materials: Design and Applications*, vol. 231, no. 1-2, pp. 171-178, 2016. Available: 10.1177/1464420716662296.

[30] B. Schoinochoritis, D. Chantzis and K. Salonitis, "Simulation of metallic powder bed additive manufacturing processes with the finite element method: A critical review", *Proceedings of the Institution of Mechanical Engineers, Part B: Journal of Engineering Manufacture*, vol. 231, no. 1, pp. 96-117, 2016. Available: 10.1177/0954405414567522.

[31] J. Navarro-Zafra, J. Curiel-Sosa and M. Serna Moreno, "Three-Dimensional Static and Dynamic Analysis of a Composite Cruciform Structure Subjected to Biaxial Loading: A Discontinuum Approach", *Applied Composite Materials*, vol. 23, no. 2, pp. 139-154, 2015. Available: 10.1007/s10443-015-9453-4.

[32] D. De Meo, N. Zhu and E. Oterkus, "Peridynamic Modeling of Granular Fracture in Polycrystalline Materials", *Journal of Engineering Materials and Technology*, vol. 138, no. 4, 2016. Available: 10.1115/1.4033634.

[33] M. Miga et al., "Modeling of Retraction and Resection for Intraoperative Updating of Images", *Neurosurgery*, vol. 49, no. 1, pp. 75-85, 2001. Available: 10.1227/00006123-200107000-00012.

107

[34]L. Vigneron, M. Duflot, P. Robe, S. Warfield and J. Verly, "2D XFEM-based modeling of retraction and successive resections for preoperative image update", *Computer Aided Surgery*, pp. 1-20, 2009. Available: 10.1080/10929080903052677.

[35]N. Mo�s, J. Dolbow and T. Belytschko, "A finite element method for crack growth without remeshing", *International Journal for Numerical Methods in Engineering*, vol. 46, no. 1, pp. 131-150, 1999. Available: 10.1002/(sici)1097-0207(19990910)46:1<131::aid-nme726>3.0.co;2-j.

[36]D. Stoia, E. Linul and L. Marsavina, "Influence of Manufacturing Parameters on Mechanical Properties of Porous Materials by Selective Laser Sintering", *Materials*, vol. 12, no. 6, p. 871, 2019. Available: 10.3390/ma12060871.

[37]J. Bai, B. Zhang, J. Song, G. Bi, P. Wang and J. Wei, "The effect of processing conditions on the mechanical properties of polyethylene produced by selective laser sintering", *Polymer Testing*, vol. 52, pp. 89-93, 2016. Available: 10.1016/j.polymertesting.2016.04.004.

[38]E. Lahtinen et al., "Preparation of Highly Porous Carbonous Electrodes by Selective Laser Sintering", *ACS Applied Energy Materials*, vol. 2, no. 2, pp. 1314-1318, 2019. Available: 10.1021/acsaem.8b01881.

[39]Z. Xu, Y. Wang, D. Wu, K. Ananth and J. Bai, "The process and performance comparison of polyamide 12 manufactured by multi jet fusion and selective laser sintering", *Journal of Manufacturing Processes*, vol. 47, pp. 419-426, 2019. Available: 10.1016/j.jmapro.2019.07.014.

[40]S. Greiner, K. Wudy, L. Lanzl and D. Drummer, "Selective laser sintering of polymer blends: Bulk properties and process behavior", *Polymer Testing*, vol. 64, pp. 136-144, 2017. Available: 10.1016/j.polymertesting.2017.09.039.

[41]M. Schmidt, D. Pohle and T. Rechtenwald, "Selective Laser Sintering of PEEK", *CIRP Annals*, vol. 56, no. 1, pp. 205-208, 2007. Available: 10.1016/j.cirp.2007.05.097.

[42]"Wohlers publishes 2018 AM report", *Metal Powder Report*, vol. 75, no. 4, p. 237, 2018. Available: 10.1016/j.mprp.2020.06.013.

[43] S. Kumar, "Selective laser sintering: A qualitative and objective approach", *JOM*, vol. 55, no. 10, pp. 43-47, 2003. Available: 10.1007/s11837-003-0175-y.

[44] J. Bai, J. Song and J. Wei, "Tribological and mechanical properties of MoS2 enhanced polyamide 12 for selective laser sintering", *Journal of Materials Processing Technology*, vol. 264, pp. 382-388, 2019. Available: 10.1016/j.jmatprotec.2018.09.026.

[45] S. Yuan, D. Strobbe, J. Kruth, P. Van Puyvelde and B. Van der Bruggen, "Production of polyamide-12 membranes for microfiltration through selective laser sintering", *Journal of Membrane Science*, vol. 525, pp. 157-162, 2017. Available: 10.1016/j.memsci.2016.10.041.

[46] E. Olakanmi, R. Cochrane and K. Dalgarno, "A review on selective laser sintering/melting (SLS/SLM) of aluminium alloy powders: Processing, microstructure, and properties", *Progress in Materials Science*, vol. 74, pp. 401-477, 2015. Available: 10.1016/j.pmatsci.2015.03.002.

[47] T. Laumer, T. Stichel, K. Nagulin and M. Schmidt, "Optical analysis of polymer powder materials for Selective Laser Sintering", *Polymer Testing*, vol. 56, pp. 207-213, 2016. Available: 10.1016/j.polymertesting.2016.10.010.

[48] S. Tiwari, S. Pande, S. Agrawal and S. Bobade, "Selection of selective laser sintering materials for different applications", *Rapid Prototyping Journal*, vol. 21, no. 6, pp. 630-648, 2015. Available: 10.1108/rpj-03-2013-0027.

[49] "DuraForm® PA Plastic. Technical report", 3D Systems Corporation, 2010.

[50] B. Van Hooreweder, D. Moens, R. Boonen, J. Kruth and P. Sas, "On the difference in material structure and fatigue properties of nylon specimens produced by injection molding and selective laser sintering", *Polymer Testing*, vol. 32, no. 5, pp. 972-981, 2013. Available: 10.1016/j.polymertesting.2013.04.014.

[51] H. Ly et al., "Prediction and Sensitivity Analysis of Bubble Dissolution Time in 3D Selective Laser Sintering Using Ensemble Decision Trees", *Materials*, vol. 12, no. 9, p. 1544, 2019. Available: 10.3390/ma12091544.

[52] M. Schmid, A. Amado and K. Wegener, "Materials perspective of polymers for additive manufacturing with selective laser sintering", *Journal of Materials Research*, vol. 29, no. 17, pp. 1824-1832, 2014. Available: 10.1557/jmr.2014.138.

[53] X. Wang, T. Laoui, J. Bonse, J. Kruth, B. Lauwers and L. Froyen, "Direct Selective Laser Sintering of Hard Metal Powders: Experimental Study and Simulation", *The International Journal of Advanced Manufacturing Technology*, vol. 19, no. 5, pp. 351-357, 2002. Available: 10.1007/s001700200024.

[54] F. Shen, S. Yuan, C. Chua and K. Zhou, "Development of process efficiency maps for selective laser sintering of polymeric composite powders: Modeling and experimental testing", *Journal of Materials Processing Technology*, vol. 254, pp. 52-59, 2018. Available: 10.1016/j.jmatprotec.2017.11.027.

[55] J. Kim and T. Creasy, "Selective laser sintering characteristics of nylon 6/clay-reinforced nanocomposite", *Polymer Testing*, vol. 23, no. 6, pp. 629-636, 2004. Available: 10.1016/j.polymertesting.2004.01.014.

[56] F. Sillani, R. Kleijnen, M. Vetterli, M. Schmid and K. Wegener, "Selective laser sintering and multi jet fusion: Process-induced modification of the raw materials and analyses of parts performance", *Additive Manufacturing*, vol. 27, pp. 32-41, 2019. Available: 10.1016/j.addma.2019.02.004.

[57] Z. Zhang, X. Yao and P. Ge, "Phase-field-model-based analysis of the effects of powder particle on porosities and densities in selective laser sintering additive manufacturing", *International Journal of Mechanical Sciences*, vol. 166, p. 105230, 2020. Available: 10.1016/j.ijmecsci.2019.105230.

[58] T. Stichel et al., "A Round Robin study for selective laser sintering of polymers: Back tracing of the pore morphology to the process parameters", *Journal of Materials Processing Technology*, vol. 252, pp. 537-545, 2018. Available: 10.1016/j.jmatprotec.2017.10.013.

[59] M. Ganci, W. Zhu, G. Buffa, L. Fratini, S. Bo and C. Yan, "A macroscale FEM-based approach for selective laser sintering of thermoplastics", *The International Journal of*

Advanced Manufacturing Technology, vol. 91, no. 9-12, pp. 3169-3180, 2017. Available: 10.1007/s00170-017-9998-5.

[60] T. Hettesheimer, S. Hirzel and H. Roß, "Energy savings through additive manufacturing: an analysis of selective laser sintering for automotive and aircraft components", *Energy Efficiency*, vol. 11, no. 5, pp. 1227-1245, 2018. Available: 10.1007/s12053-018-9620-1.

[61] J. TATAMI, D. HIRATSUKA, S. OKADA, K. KOMEYA and T. WAKIHARA, "Analysis of sintering behavior of silicon nitride based on master sintering curve theory of liquid phase sintering", *Journal of the Ceramic Society of Japan*, vol. 124, no. 4, pp. 375-380, 2016. Available: 10.2109/jcersj2.15291.

[62] O. Pokluda, C. Bellehumeur and J. Vlachopoulos, "Modification of Frenkel's model for sintering", *AIChE Journal*, vol. 43, no. 12, pp. 3253-3256, 1997. Available: 10.1002/aic.690431213.

[63] H. Zhao, "Research and development on the sintering techniques of molybdenum and molybdenum alloys", *Powder Metall Technol*, vol. 37, no. 5, p. 382, 2019. [Accessed 22 June 2021].

[64] J. Mackenzie and R. Shuttleworth, "A Phenomenological Theory of Sintering", *Proceedings of the Physical Society. Section B*, vol. 62, no. 12, pp. 833-852, 1949. Available: 10.1088/0370-1301/62/12/310.

[65] I. Greenquist, M. Tonks, L. Aagesen and Y. Zhang, "Development of a microstructural grand potential-based sintering model", *Computational Materials Science*, vol. 172, p. 109288, 2020. Available: 10.1016/j.commatsci.2019.109288.

[66] S. Lee and S. Kang, "Theoretical analysis of liquid-phase sintering: Pore filling theory", *Acta Materialia*, vol. 46, no. 9, pp. 3191-3202, 1998. Available: 10.1016/s1359-6454(97)00489-8.

[67] J. Kruth, P. Mercelis, J. Van Vaerenbergh, L. Froyen and M. Rombouts, "Binding mechanisms in selective laser sintering and selective laser melting", *Rapid Prototyping Journal*, vol. 11, no. 1, pp. 26-36, 2005. Available: 10.1108/13552540510573365.

[68] S. Barakh Ali et al., "Understanding the effects of formulation and process variables on the printlets quality manufactured by selective laser sintering 3D printing", *International Journal of Pharmaceutics*, vol. 570, p. 118651, 2019. Available: 10.1016/j.ijpharm.2019.118651.

[69] A. Gobal and B. Ravani, "Physical Modeling for Selective Laser Sintering Process", *Journal of Computing and Information Science in Engineering*, vol. 17, no. 2, 2017. Available: 10.1115/1.4034473.

[70] A. Espera, A. Valino, J. Palaganas, L. Souza, Q. Chen and R. Advincula, "3D Printing of a Robust Polyamide-12-Carbon Black Composite via Selective Laser Sintering: Thermal and Electrical Conductivity", *Macromolecular Materials and Engineering*, vol. 304, no. 4, p. 1800718, 2019. Available: 10.1002/mame.201800718.

[71] X. Yang, Y. Wei, S. Xi, Y. Huang, M. Kong and G. Li, "Preparation of spherical polymer powders for selective laser sintering from immiscible PA12/PEO blends with high viscosity ratios", *Polymer*, vol. 172, pp. 58-65, 2019. Available: 10.1016/j.polymer.2019.03.066.

[72] A. Jansson and L. Pejryd, "Characterisation of carbon fibre-reinforced polyamide manufactured by selective laser sintering", *Additive Manufacturing*, vol. 9, pp. 7-13, 2016. Available: 10.1016/j.addma.2015.12.003.

[73] M. Serna Moreno, J. Curiel-Sosa, J. Navarro-Zafra, J. Martínez Vicente and J. López Cela, "Crack propagation in a chopped glass-reinforced composite under biaxial testing by means of XFEM", *Composite Structures*, vol. 119, pp. 264-271, 2015. Available: 10.1016/j.compstruct.2014.08.030.

[74] C. Majewski, H. Zarringhalam and N. Hopkinson, "Effect of the degree of particle melt on mechanical properties in selective laser-sintered Nylon-12 parts", *Proceedings of the Institution of Mechanical Engineers, Part B: Journal of Engineering Manufacture*, vol. 222, no. 9, pp. 1055-1064, 2008. Available: 10.1243/09544054jem1122.

[75]M. Chapetti and C. Steimbreger, "A simple fracture mechanics estimation of the fatigue endurance of welded joints", *International Journal of Fatigue*, vol. 125, pp. 23-34, 2019. Available: 10.1016/j.ijfatigue.2019.03.021.

[76]A. Chen et al., "Enhancement mechanism of mechanical performance of highly porous mullite ceramics with bimodal pore structures prepared by selective laser sintering", *Journal of Alloys and Compounds*, vol. 776, pp. 486-494, 2019. Available: 10.1016/j.jallcom.2018.10.337.

[77]R. Pan, L. Yang, L. Zheng, L. Hao and Y. Li, "Microscopic morphology, thermodynamic and mechanical properties of thermoplastic polyurethane fabricated by selective laser sintering", *Materials Research Express*, vol. 7, no. 5, p. 055301, 2020. Available: 10.1088/2053-1591/ab8b87.

[78]C. Borzan, M. Moldovan and V. Bocanet, "Evaluation of Surface Modification of PA 2200 Parts Made by Selective Laser Sintering Process", *Revista de Chimie*, vol. 69, no. 4, pp. 886-889, 2018. Available: 10.37358/rc.18.4.6221.

[79]F. Chen, J. Wu, H. Wu, Y. Chen, C. Li and Y. Shi, "Microstructure and mechanical properties of 3Y-TZP dental ceramics fabricated by selective laser sintering combined with cold isostatic pressing", *International Journal of Lightweight Materials and Manufacture*, vol. 1, no. 4, pp. 239-245, 2018. Available: 10.1016/j.ijlmm.2018.09.002.

[80]Z. Chen, X. Zong, J. Shi and X. Zhang, "Online Monitoring Based on Temperature Field Features and Prediction Model for Selective Laser Sintering Process", *Applied Sciences*, vol. 8, no. 12, p. 2383, 2018. Available: 10.3390/app8122383.

[81]D. Stoia, L. Marsavina and E. Linul, "Mode I Fracture Toughness of Polyamide and Alumide Samples obtained by Selective Laser Sintering Additive Process", *Polymers*, vol. 12, no. 3, p. 640, 2020. Available: 10.3390/polym12030640.

[82]L. Dong, A. Makradi, S. Ahzi and Y. Remond, "Three-dimensional transient finite element analysis of the selective laser sintering process", *Journal of Materials Processing Technology*, vol. 209, no. 2, pp. 700-706, 2009. Available: 10.1016/j.jmatprotec.2008.02.040.

[83] K. Wudy, M. Hinze, F. Ranft, D. Drummer and W. Schwieger, "Selective laser sintering of zeolite filled polypropylene composites: Processing and properties of bulk adsorbents", *Journal of Materials Processing Technology*, vol. 246, pp. 136-143, 2017. Available: 10.1016/j.jmatprotec.2017.03.011.

[84] M. Alfreider, D. Kozic, O. Kolednik and D. Kiener, "In-situ elastic-plastic fracture mechanics on the microscale by means of continuous dynamical testing", *Materials & Design*, vol. 148, pp. 177-187, 2018. Available: 10.1016/j.matdes.2018.03.051.

[85] A. Ali, *Failure Analysis and Prevention*. [S.l.]: IntechOpen, 2017.

[86] S. Sheppard, *Failure prevention and reliability, 1989*. New York, N.Y. (345 East 47th St., New York 10017): American Society of Mechanical Engineers, 1989.

[87] A. Sanchez-Rivadeneira and C. Duarte, "A stable generalized/eXtended FEM with discontinuous interpolants for fracture mechanics", *Computer Methods in Applied Mechanics and Engineering*, vol. 345, pp. 876-918, 2019. Available: 10.1016/j.cma.2018.11.018.

[88] R. Ritchie and D. Liu, *Introduction to Fracture Mechanics*, 1st ed. Elsevier, 2020.

[89] P. Cornetti, V. Mantič and A. Carpinteri, "Finite Fracture Mechanics at elastic interfaces", *International Journal of Solids and Structures*, vol. 49, no. 7-8, pp. 1022-1032, 2012. Available: 10.1016/j.ijsolstr.2012.01.002.

[90] U. Zerbst et al., "Review on fracture and crack propagation in weldments – A fracture mechanics perspective", *Engineering Fracture Mechanics*, vol. 132, pp. 200-276, 2014. Available: 10.1016/j.engfracmech.2014.05.012.

[91] P. Cornetti, M. Muñoz-Reja, A. Sapora and A. Carpinteri, "Finite fracture mechanics and cohesive crack model: Weight functions vs. cohesive laws", *International Journal of Solids and Structures*, vol. 156-157, pp. 126-136, 2019. Available: 10.1016/j.ijsolstr.2018.08.003.

[92]J. Rice, "A Path Independent Integral and the Approximate Analysis of Strain Concentration by Notches and Cracks", *Journal of Applied Mechanics*, vol. 35, no. 2, pp. 379-386, 1968. Available: 10.1115/1.3601206.

[93]J. Nairn, "Direct comparison of anisotropic damage mechanics to fracture mechanics of explicit cracks", *Engineering Fracture Mechanics*, vol. 203, pp. 197-207, 2018. Available: 10.1016/j.engfracmech.2018.05.047.

[94]A. Yazid, N. Abdelkader and H. Abdelmadjid, "A state-of-the-art review of the X-FEM for computational fracture mechanics", *Applied Mathematical Modelling*, vol. 33, no. 12, pp. 4269-4282, 2009. Available: 10.1016/j.apm.2009.02.010.

[95]U. Zerbst, C. Klinger and R. Clegg, "Fracture mechanics as a tool in failure analysis — Prospects and limitations", *Engineering Failure Analysis*, vol. 55, pp. 376-410, 2015. Available: 10.1016/j.engfailanal.2015.07.001.

[96]N. O'dowd, "Applications of two parameter approaches in elastic-plastic fracture mechanics", *Engineering Fracture Mechanics*, vol. 52, no. 3, pp. 445-465, 1995. Available: 10.1016/0013-7944(95)00033-r.

[97]Y. Matvienko, "The effect of crack-tip constraint in some problems of fracture mechanics", *Engineering Failure Analysis*, vol. 110, p. 104413, 2020. Available: 10.1016/j.engfailanal.2020.104413.

[98]K. Agathos, S. Bordas and E. Chatzi, "Improving the conditioning of XFEM/GFEM for fracture mechanics problems through enrichment quasi-orthogonalization", *Computer Methods in Applied Mechanics and Engineering*, vol. 346, pp. 1051-1073, 2019. Available: 10.1016/j.cma.2018.08.007.

[99]M. Hashemi, M. Jamshidi and J. Aghdam, "Investigating fracture mechanics and flexural properties of unsaturated polyester polymer concrete (UP-PC)", *Construction and Building Materials*, vol. 163, pp. 767-775, 2018. Available: 10.1016/j.conbuildmat.2017.12.115.

[100] J. Chang and C. Hudson, *Methods and models for predicting fatigue crack growth under random loading*. Philadelphia, Pa.: American Society for Testing and Materials, 1981.

[101] N. Abid, J. Pro and F. Barthelat, "Fracture mechanics of nacre-like materials using discrete-element models: Effects of microstructure, interfaces and randomness", *Journal of the Mechanics and Physics of Solids*, vol. 124, pp. 350-365, 2019. Available: 10.1016/j.jmps.2018.10.012.

[102] A. Riccio, U. Caruso, A. Raimondo and A. Sellitto, "Robustness of XFEM Method for the Simulation of Cracks Propagation in Fracture Mechanics Problems", *American Journal of Engineering and Applied Sciences*, vol. 9, no. 3, pp. 599-610, 2016. Available: 10.3844/ajeassp.2016.599.610.

[103] P. Paris and F. Erdogan, "A Critical Analysis of Crack Propagation Laws", *Journal of Basic Engineering*, vol. 85, no. 4, pp. 528-533, 1963. Available: 10.1115/1.3656900.

[104] S. Dadbakhsh, L. Verbelen, O. Verkinderen, D. Strobbe, P. Van Puyvelde and J. Kruth, "Effect of PA12 powder reuse on coalescence behaviour and microstructure of SLS parts", *European Polymer Journal*, vol. 92, pp. 250-262, 2017. Available: 10.1016/j.eurpolymj.2017.05.014.

[105] P. Weißgraeber, J. Felger, D. Geipel and W. Becker, "Cracks at elliptical holes: Stress intensity factor and Finite Fracture Mechanics solution", *European Journal of Mechanics - A/Solids*, vol. 55, pp. 192-198, 2016. Available: 10.1016/j.euromechsol.2015.09.002.

[106] U. Zerbst, M. Madia and M. Vormwald, "Applying fracture mechanics to fatigue strength determination – Some basic considerations", *International Journal of Fatigue*, vol. 126, pp. 188-201, 2019. Available: 10.1016/j.ijfatigue.2019.05.009.

[107] A. Sapora, P. Cornetti, A. Campagnolo and G. Meneghetti, "Fatigue limit: Crack and notch sensitivity by Finite Fracture Mechanics", *Theoretical and Applied Fracture Mechanics*, vol. 105, p. 102407, 2020. Available: 10.1016/j.tafmec.2019.102407.

[108] T. Oliveira, W. Vélez, E. Santana, T. Araújo, F. Mendonça and A. Portela, "A local mesh free method for linear elasticity and fracture mechanics", *Engineering Analysis with Boundary Elements*, vol. 101, pp. 221-242, 2019. Available: 10.1016/j.enganabound.2019.01.007.

[109] S. Antolovich, A. Saxena and W. Gerberich, "Fracture mechanics – An interpretive technical history", *Mechanics Research Communications*, vol. 91, pp. 46-86, 2018. Available: 10.1016/j.mechrescom.2018.03.003.

[110] A. Cano, A. Salazar and J. Rodríguez, "Effect of temperature on the fracture behavior of polyamide 12 and glass-filled polyamide 12 processed by selective laser sintering", *Engineering Fracture Mechanics*, vol. 203, pp. 66-80, 2018. Available: 10.1016/j.engfracmech.2018.07.035.

[111] P. GOPE and A. THAKUR, "Experimental investigation of crack growth direction in multiple cracks", *Fatigue & Fracture of Engineering Materials & Structures*, vol. 34, no. 10, pp. 804-815, 2011. Available: 10.1111/j.1460-2695.2011.01574.x.

[112] F. Ellyin and H. El Kadi, "Predicting crack growth direction in unidirectional composite laminae", *Engineering Fracture Mechanics*, vol. 36, no. 1, pp. 27-37, 1990. Available: 10.1016/0013-7944(90)90093-v.

[113] F. Li, N. Macdonald, R. Guijt and M. Breadmore, "Increasing the functionalities of 3D printed microchemical devices by single material, multimaterial, and print-pause-print 3D printing", *Lab on a Chip*, vol. 19, no. 1, pp. 35-49, 2019. Available: 10.1039/c8lc00826d.

[114] R. Dimitri, P. Cornetti, V. Mantič, M. Trullo and L. De Lorenzis, "Mode-I debonding of a double cantilever beam: A comparison between cohesive crack modeling and Finite Fracture Mechanics", *International Journal of Solids and Structures*, vol. 124, pp. 57-72, 2017. Available: 10.1016/j.ijsolstr.2017.06.007.

[115] M. Pais, "Variable amplitude fatigue analysis using surrogate models and exact XFEM reanalysis", Ph.D Dissertation, University of Florida, Florida, USA, 2021.

[116] J. Jokinen and M. Kanerva, "Simulation of Delamination Growth at CFRP-Tungsten Aerospace Laminates Using VCCT and CZM Modelling Techniques", *Applied Composite Materials*, vol. 26, no. 3, pp. 709-721, 2018. Available: 10.1007/s10443-018-9746-5.

[117] Y. Jiang, T. Tay, L. Chen and X. Sun, "An edge-based smoothed XFEM for fracture in composite materials", *International Journal of Fracture*, vol. 179, no. 1-2, pp. 179-199, 2012. Available: 10.1007/s10704-012-9786-z.

[118] Y. Jiang, T. Tay, L. Chen and X. Sun, "An edge-based smoothed XFEM for fracture in composite materials", *International Journal of Fracture*, vol. 179, no. 1-2, pp. 179-199, 2012. Available: 10.1007/s10704-012-9786-z.

[119] Z. Zhuang and Zhuo Zhuang., *Extended Finite Element Method*. Academic Press, 2014.

[120] N. Abdullah, J. Curiel-Sosa, Z. Taylor, B. Tafazzolimoghaddam, J. Martinez Vicente and C. Zhang, "Transversal crack and delamination of laminates using XFEM", *Composite Structures*, vol. 173, pp. 78-85, 2017. Available: 10.1016/j.compstruct.2017.04.011.

[121] K. Rege and H. Lemu, "A review of fatigue crack propagation modelling techniques using FEM and XFEM", *IOP Conference Series: Materials Science and Engineering*, vol. 276, p. 012027, 2017. Available: 10.1088/1757-899x/276/1/012027.

[122] M. Sadd, *Elasticity: theory, applications, and numerics*, 3rd ed. Academic Press, 2009.

[123] T. Fries, "Overview and comparison of different variants of the XFEM", *PAMM*, vol. 14, no. 1, pp. 27-30, 2014. Available: 10.1002/pamm.201410008.

[124] H. Sun, H. Waisman and R. Betti, "A multiscale flaw detection algorithm based on XFEM", *International Journal for Numerical Methods in Engineering*, vol. 100, no. 7, pp. 477-503, 2014. Available: 10.1002/nme.4741.

[125] Y. Jiang, J. Dong, D. Nie and X. Zhang, "XFEM with partial Heaviside function enrichment for fracture analysis", *Engineering Fracture Mechanics*, vol. 241, p. 107375, 2021. Available: 10.1016/j.engfracmech.2020.107375.

[126]W. De Corte, P. Helincks, V. Boel, J. Klusak, S. Seitl and G. De Schutter, "Generalised fracture mechanics approach to the interfacial failure analysis of a bonded steel-concrete joint", *Frattura ed Integrità Strutturale*, vol. 11, no. 42, pp. 147-160, 2017. Available: 10.3221/igf-esis.42.16.

[127]A. Sapora, P. Cornetti, A. Campagnolo and G. Meneghetti, "Fatigue crack onset by Finite Fracture Mechanics", *Procedia Structural Integrity*, vol. 18, pp. 501-506, 2019. Available: 10.1016/j.prostr.2019.08.193.

[128]E. De Luycker, D. Benson, T. Belytschko, Y. Bazilevs and M. Hsu, "X-FEM in isogeometric analysis for linear fracture mechanics", *International Journal for Numerical Methods in Engineering*, vol. 87, no. 6, pp. 541-565, 2011. Available: 10.1002/nme.3121.

[129]H. Chen et al., "A two-set order parameters phase-field modeling of crack deflection/penetration in a heterogeneous microstructure", *Computer Methods in Applied Mechanics and Engineering*, vol. 347, pp. 1085-1104, 2019. Available: 10.1016/j.cma.2019.01.014.

[130]T. Menouillard and T. Belytschko, "Dynamic fracture with meshfree enriched XFEM", *Acta Mechanica*, vol. 213, no. 1-2, pp. 53-69, 2010. Available: 10.1007/s00707-009-0275-z.

[131]R. Duddu, S. Bordas, D. Chopp and B. Moran, "A combined extended finite element and level set method for biofilm growth", *International Journal for Numerical Methods in Engineering*, vol. 74, no. 5, pp. 848-870, 2008. Available: 10.1002/nme.2200.

[132]B. Prabel, A. Combescure, A. Gravouil and S. Marie, "Level set X-FEM non-matching meshes: application to dynamic crack propagation in elastic–plastic media", *International Journal for Numerical Methods in Engineering*, vol. 69, no. 8, pp. 1553-1569, 2007. Available: 10.1002/nme.1819.

[133]N. Sukumar and J. Prévost, "Modeling quasi-static crack growth with the extended finite element method Part I: Computer implementation", *International Journal of*

Solids and Structures, vol. 40, no. 26, pp. 7513-7537, 2003. Available: 10.1016/j.ijsolstr.2003.08.002.

[134]M. Malekan, A. Khosravi and L. St-Pierre, "An Abaqus plug-in to simulate fatigue crack growth", *Engineering with Computers*, 2021. Available: 10.1007/s00366-021-01321-x.

[135]S. Loehnert, "Stabilizing the XFEM for static and dynamic crack simulations", *PAMM*, vol. 15, no. 1, pp. 137-138, 2015. Available: 10.1002/pamm.201510059.

[136]C. Daux, N. Mo�s, J. Dolbow, N. Sukumar and T. Belytschko, "Arbitrary branched and intersecting cracks with the extended finite element method", *International Journal for Numerical Methods in Engineering*, vol. 48, no. 12, pp. 1741-1760, 2000. Available: 10.1002/1097-0207(20000830)48:12<1741::aid-nme956>3.0.co;2-l.

[137]D. Huynh and T. Belytschko, "The extended finite element method for fracture in composite materials", *International Journal for Numerical Methods in Engineering*, vol. 77, no. 2, pp. 214-239, 2009. Available: 10.1002/nme.2411.

[138]H. Pathak, A. Singh, I. Singh and S. Yadav, "A simple and efficient XFEM approach for 3-D cracks simulations", *International Journal of Fracture*, vol. 181, no. 2, pp. 189-208, 2013. Available: 10.1007/s10704-013-9835-2.

[139]S. Kumar, I. Singh and B. Mishra, "A homogenized XFEM approach to simulate fatigue crack growth problems", *Computers & Structures*, vol. 150, pp. 1-22, 2015. Available: 10.1016/j.compstruc.2014.12.008.

[140]R. Patil, B. Mishra and I. Singh, "A new multiscale XFEM for the elastic properties evaluation of heterogeneous materials", *International Journal of Mechanical Sciences*, vol. 122, pp. 277-287, 2017. Available: 10.1016/j.ijmecsci.2017.01.028.

[141]A. Dyson, Z. Tang and A. Tolooiyan, "Use of stochastic XFEM in the investigation of heterogeneity effects on the tensile strength of intermediate geotechnical materials", *Finite Elements in Analysis and Design*, vol. 145, pp. 1-9, 2018. Available: 10.1016/j.finel.2018.03.003.

[142] U. Ajoku, N. Hopkinson and M. Caine, "Experimental measurement and finite element modelling of the compressive properties of laser sintered Nylon-12", *Materials Science and Engineering: A*, vol. 428, no. 1-2, pp. 211-216, 2006. Available: 10.1016/j.msea.2006.05.019.

[143] A. Gusarov, T. Laoui, L. Froyen and V. Titov, "Contact thermal conductivity of a powder bed in selective laser sintering", *International Journal of Heat and Mass Transfer*, vol. 46, no. 6, pp. 1103-1109, 2003. Available: 10.1016/s0017-9310(02)00370-8.

[144] X. Wang, T. Laoui, J. Bonse, J. Kruth, B. Lauwers and L. Froyen, "Direct Selective Laser Sintering of Hard Metal Powders: Experimental Study and Simulation", *The International Journal of Advanced Manufacturing Technology*, vol. 19, no. 5, pp. 351-357, 2002. Available: 10.1007/s001700200024.

[145] S. Kolossov, E. Boillat, R. Glardon, P. Fischer and M. Locher, "3D FE simulation for temperature evolution in the selective laser sintering process", *International Journal of Machine Tools and Manufacture*, vol. 44, no. 2-3, pp. 117-123, 2004. Available: 10.1016/j.ijmachtools.2003.10.019.

[146] L. Dong, A. Makradi, S. Ahzi and Y. Remond, "Three-dimensional transient finite element analysis of the selective laser sintering process", *Journal of Materials Processing Technology*, vol. 209, no. 2, pp. 700-706, 2009. Available: 10.1016/j.jmatprotec.2008.02.040.

[147] M. Shiomi, A. Yoshidome, F. Abe and K. Osakada, "Finite element analysis of melting and solidifying processes in laser rapid prototyping of metallic powders", *International Journal of Machine Tools and Manufacture*, vol. 39, no. 2, pp. 237-252, 1999. Available: 10.1016/s0890-6955(98)00036-4.

[148] U. Ajoku, N. Saleh, N. Hopkinson, R. Hague and P. Erasenthiran, "Investigating mechanical anisotropy and end-of-vector effect in laser-sintered nylon parts", *Proceedings of the Institution of Mechanical Engineers, Part B: Journal of Engineering Manufacture*, vol. 220, no. 7, pp. 1077-1086, 2006. Available: 10.1243/09544054jem537.

[149] B. Partee, S. Hollister and S. Das, "Selective Laser Sintering Process Optimization for Layered Manufacturing of CAPA® 6501 Polycaprolactone Bone Tissue Engineering Scaffolds", *Journal of Manufacturing Science and Engineering*, vol. 128, no. 2, pp. 531-540, 2005. Available: 10.1115/1.2162589.

[150] B. Tafazzolimoghaddam, "Computational Mechanics of Fracture and Fatigue in Composite Laminates by Means of XFEM and CZM", Ph.D, the University of Sheffield, 2017.

[151] D. Hitt, B. Haworth and N. Hopkinson, "Fracture mechanics approach to compare laser sintered parts and injection mouldings of nylon-12", *Proceedings of the Institution of Mechanical Engineers, Part B: Journal of Engineering Manufacture*, vol. 225, no. 9, pp. 1663-1672, 2011. Available: 10.1177/0954405411402141.

[152] N. Hopkinson, C. Majewski and H. Zarringhalam, "Quantifying the degree of particle melt in Selective Laser Sintering ®", *CIRP Annals*, vol. 58, no. 1, pp. 197-200, 2009. Available: 10.1016/j.cirp.2009.03.001.

[153] C. Majewski, H. Zarringhalam and N. Hopkinson, "Effect of the degree of particle melt on mechanical properties in selective laser-sintered Nylon-12 parts", *Proceedings of the Institution of Mechanical Engineers, Part B: Journal of Engineering Manufacture*, vol. 222, no. 9, pp. 1055-1064, 2008. Available: 10.1243/09544054jem1122.

[154] H. Zarringhalam, N. Hopkinson, N. Kamperman and J. de Vlieger, "Effects of processing on microstructure and properties of SLS Nylon 12", *Materials Science and Engineering: A*, vol. 435-436, pp. 172-180, 2006. Available: 10.1016/j.msea.2006.07.084.

[155] J. Kruth, G. Levy, F. Klocke and T. Childs, "Consolidation phenomena in laser and powder-bed based layered manufacturing", *CIRP Annals*, vol. 56, no. 2, pp. 730-759, 2007. Available: 10.1016/j.cirp.2007.10.004.

[156] H. Zarringhalam, C. Majewski and N. Hopkinson, "Degree of particle melt in Nylon-12 selective laser-sintered parts", *Rapid Prototyping Journal*, vol. 15, no. 2, pp. 126-132, 2009. Available: 10.1108/13552540910943423.

[157] T. Brugo, R. Palazzetti, S. Ciric-Kostic, X. Yan, G. Minak and A. Zucchelli, "Fracture mechanics of laser sintered cracked polyamide for a new method to induce cracks by additive manufacturing", *Polymer Testing*, vol. 50, pp. 301-308, 2016. Available: 10.1016/j.polymertesting.2016.01.024.

[158] A. Salazar, A. Rico, J. Rodríguez, J. Segurado Escudero, R. Seltzer and F. Martin de la Escalera Cutillas, "Fatigue crack growth of SLS polyamide 12: Effect of reinforcement and temperature", *Composites Part B: Engineering*, vol. 59, pp. 285-292, 2014. Available: 10.1016/j.compositesb.2013.12.017.

[159] R. Seltzer, F. de la Escalera and J. Segurado, "Effect of water conditioning on the fracture behavior of PA12 composites processed by selective laser sintering", *Materials Science and Engineering: A*, vol. 528, no. 22-23, pp. 6927-6933, 2011. Available: 10.1016/j.msea.2011.05.045.

[160] M. Strobl and T. Seelig, "Restrictions in phase field modeling of brittle fracture", *PAMM*, vol. 18, no. 1, 2018. Available: 10.1002/pamm.201800157.

[161] K. Song, C. Dávila and C. Rose, "Guidelines and parameter selection for the simulation of progressive delamination", in *In Abaqus User's conference*, 2008, pp. 43-44.

[162] A. Ronca et al., "Selective Laser Sintering Fabricated Thermoplastic Polyurethane/Graphene Cellular Structures with Tailorable Properties and High Strain Sensitivity", *Applied Sciences*, vol. 9, no. 5, p. 864, 2019. Available: 10.3390/app9050864.

[163] B. Caulfield, P. McHugh and S. Lohfeld, "Dependence of mechanical properties of polyamide components on build parameters in the SLS process", *Journal of Materials Processing Technology*, vol. 182, no. 1-3, pp. 477-488, 2007. Available: 10.1016/j.jmatprotec.2006.09.007.

[164] J. Usher, T. Gornet and T. Starr, "Weibull growth modeling of laser-sintered nylon 12", *Rapid Prototyping Journal*, vol. 19, no. 4, pp. 300-306, 2013. Available: 10.1108/13552541311323308.

[165]A. Amado-Becker, J. Ramos-Grez, M. José Yañez, Y. Vargas and L. Gaete, "Elastic tensor stiffness coefficients for SLS Nylon 12 under different degrees of densification as measured by ultrasonic technique", *Rapid Prototyping Journal*, vol. 14, no. 5, pp. 260-270, 2008. Available: 10.1108/13552540810907929.

[166]N. Lammens, M. Kersemans, I. De Baere and W. Van Paepegem, "On the visco-elasto-plastic response of additively manufactured polyamide-12 (PA-12) through selective laser sintering", *Polymer Testing*, vol. 57, pp. 149-155, 2017. Available: 10.1016/j.polymertesting.2016.11.032.

[167]D. Drummer, D. Rietzel and F. Kühnlein, "Development of a characterization approach for the sintering behavior of new thermoplastics for selective laser sintering", *Physics Procedia*, vol. 5, pp. 533-542, 2010. Available: 10.1016/j.phpro.2010.08.081.

[168]H. Amel, H. Moztarzadeh, J. Rongong and N. Hopkinson, "Investigating the behavior of laser-sintered Nylon 12 parts subject to dynamic loading", *Journal of Materials Research*, vol. 29, no. 17, pp. 1852-1858, 2014. Available: 10.1557/jmr.2014.150.

[169]W. Dewulf, M. Pavan, T. Craeghs and J. Kruth, "Using X-ray computed tomography to improve the porosity level of polyamide-12 laser sintered parts", *CIRP Annals*, vol. 65, no. 1, pp. 205-208, 2016. Available: 10.1016/j.cirp.2016.04.056.

[170]M. Crespo, M. Gómez-del Río and J. Rodríguez, "Failure of SLS polyamide 12 notched samples at high loading rates", *Theoretical and Applied Fracture Mechanics*, vol. 92, pp. 233-239, 2017. Available: 10.1016/j.tafmec.2017.08.008.

[171]N. Zarmehri, M. Nazari and M. Rokhi, "XFEM analysis of a 2D cracked finite domain under thermal shock based on Green-Lindsay theory", *Engineering Fracture Mechanics*, vol. 191, pp. 286-299, 2018. Available: 10.1016/j.engfracmech.2017.12.039.

[172]D. Mora, M. Niffenegger, G. Qian, M. Jaros and B. Niceno, "Modelling of reactor pressure vessel subjected to pressurized thermal shock using 3D-XFEM", *Nuclear Engineering and Design*, vol. 353, p. 110237, 2019. Available: 10.1016/j.nucengdes.2019.110237.

[173] Y. Murakami and L. Keer, "Stress Intensity Factors Handbook, Vol. 3", *Journal of Applied Mechanics*, vol. 60, no. 4, pp. 1063-1063, 1993. Available: 10.1115/1.2900983.

[174] N. Prasad, M. Aliabadi and D. Rooke, "The dual boundary element method for transient thermoelastic crack problems", *International Journal of Solids and Structures*, vol. 33, no. 19, pp. 2695-2718, 1996. Available: 10.1016/0020-7683(95)00183-2.

[175] M. Uddin, D. Williams and A. Blencowe, "Recycling of Selective Laser Sintering Waste Nylon Powders into Fused Filament Fabrication Parts Reinforced with Mg Particles", *Polymers*, vol. 13, no. 13, p. 2046, 2021. Available: 10.3390/polym13132046.